Exploring Microscopic Thermal Transport Properties of Molecular Crystals with Simulations and Experiments

Thesis by
Andrew Beyer Robbins

In Partial Fulfillment of the Requirements for the
Degree of
Doctor of Philosophy

Caltech

CALIFORNIA INSTITUTE OF TECHNOLOGY
Pasadena, California

2019
Defended January 11, 2019

ACKNOWLEDGEMENTS

ABSTRACT

Polymers are widely used in applications due to their diverse and controllable properties in many physical domains. However, polymers have not historically been used in applications for which a high thermal conductivity is required as bulk polymers are typically thermal insulators. However, research in recent decades on a handful of highly oriented or semi-crystalline polymers has shown the potential for dramatically increased uniaxial thermal conductivity by factors exceeding 100. This dramatic increase in thermal conductivity is because heat is conducted by atomic vibrations along the covalently bonded polymer backbone rather than across chains by weak van der Waals bonds as in unoriented polymers. While it is known that polymers can be processed to yield these properties, much remains unknown about the microscopic transport properties of atomic vibrations in these materials and the true upper limits to thermal conductivity. In this thesis, we address these knowledge gaps by using a combination of simulations and experiments to investigate thermal conduction in semi-crystalline and crystalline polymers.

First, we present molecular dynamics simulations of a perfect polymer crystal, poly-norbornene. While polymer crystals studied typically exhibit substantially enhanced thermal conductivities above those of the amorphous form, polynorbornene exhibits a glass-like thermal conductivity of less than $1 \ \mathrm{Wm^{-1}K^{-1}}$ even as a perfect crystal. This unusual behavior occurs despite the polymer satisfying many of the conventional criteria for high thermal conductivity. Using our simulations, we show that the origin of this unusual behavior is excessively anharmonic bonds and a complex unit cell.

Second, we move to experimental studies of thermal transport in polymers. A key requirement to perform materials science is a method to routinely and easily characterize the property of interest in diverse samples. For polymers, this property is typically the in-plane thermal conductivity. This property turns out to be surprisingly difficult to measure using conventional thermal characterization methods. In this work, we adapt transient grating spectroscopy (TG), a well-known method in the chemistry community, to perform in-plane thermal conductivity measurements of polymer films. TG can resolve the in-plane thermal anisotropy of a sample without any physical contact and at tunable length scales, a substantial advance in capability over all prior characterization methods. We extend the application of TG to probe sub-μm length scales, and we successfully apply the technique to numerous poor

quality polymer samples as well as thin films.

Finally, we exploit the capability of TG to probe thermal conduction over sub-µm length scales to provide the first experimentally resolved microscopic transport properties of atomic vibrations in semi-crystalline polyethylene (PE). Despite the intense interest over decades in PE due to its high intrinsic thermal conductivity, no experimental measurement has yet been able to directly probe the heat-carrying phonons, leading to many questions about the relevant scattering mechanisms and absolute upper limits of thermal conductivity in real samples. Using TG, we present the first observation of quasi-ballistic thermal transport at sub-µm length scales, from which we obtain the phonon mean free path spectra of a semi-crystalline PE sample. Further, we pair these results with Small-Angle X-ray Scattering measurements to show that thermal phonons propagate ballistically within and across nanocrystalline domains, contrary to the conventional viewpoint. These results provide an unprecedented microscopic view of thermal transport in polymer crystals that was previously experimentally inaccessible.

PUBLISHED CONTENT AND CONTRIBUTIONS

1. Robbins, A. B., Drakopoulos, S. X., Ronca, S. & Minnich, A. J. Thermal Phonons with Micron-Scale Mean Free Paths in Semi-Crystalline Polyethylene. *(In Preparation).*
   Contributions: Andrew B. Robbins built the experimental setup, wrote all data acquisition code, performed all thermal measurements, wrote all data analysis code, performed all thermal data analysis, and wrote a majority of the manuscript.

2. Robbins, A. B. & Minnich, A. J. Crystalline polymers with exceptionally low thermal conductivity studied using molecular dynamics. *Applied Physics Letters* **107,** 201908 (Nov. 16, 2015).
   DOI: http://doi.org/10.1063/1.4936195
   Contributions: Andrew B. Robbins performed all calculations and simulations, wrote all analysis code, performed all analysis, and wrote the manuscript.

TABLE OF CONTENTS

LIST OF ILLUSTRATIONS

C h a p t e r   1

INTRODUCTION

Polymers are a diverse and fascinating class of materials that exhibit a wide range of properties across numerous physical domains. Many highly oriented polymers have garnered great interest for their extreme anisotropy, which can result in extraordinary properties along the direction of alignment. Of prime interest in this thesis is the exceptionally high thermal conductivity that is possible along oriented polymer chains.

1.1   Thermal Transport in Polymers

Unoriented polymers are generally considered to be heat insulators due to the poor heat transport across the weak van der Waals bonds between neighboring polymer chains. Nearly all such polymers have thermal conductivity values around $\kappa = 0.2$ Wm^{-1}K^{-1}[1]. Such low values for κ can be beneficial in certain applications. For example, various polymers have been studied extensively for use in thermoelectrics[2], in an attempt to take advantage of poor heat transport in electrically conductive polymers. On the other hand, achieving thermally conductive polymers while maintaining many of their other material properties would open up a wide range of new material applications. For example, heat spreaders in electronics packaging or light-emitting diodes could benefit from polymers' flexible mechanical properties, and light-weight heat exchangers could benefit from their corrosion resistance. As a result, expanding and understanding the range of possible material properties in polymers is an important topic of ongoing research in materials science.

While heat transport in polymers is typically limited by weak inter-chain bonds, oriented polymers are highly anisotropic, with one direction being characterized by strong covalent backbone bonds. As a result, transport along the polymer chains in an oriented structure can be greatly enhanced. Early studies on drawn amorphous polymers reported modest increases in thermal conductivity, κ, of $\sim 30\%$ for polymethylmethacrylate (PMMA)[3]. Over the next decade, several studies on oriented semi-crystalline polymers like polyethylene[4, 5] and polypropylene[6] showed that some polymers could exhibit thermal conductivities exceeding their initial value by 2-3 orders of magnitude. Choy et al. measured a maximum value of

$\kappa = 14.0$ Wm^{-1}K^{-1} in drawn polyethylene[7].

Following these early works, one of the overarching goals of ongoing research has been to synthesize polymers with the highest possible uniaxial thermal conductivity. For example, many studies have increased the draw ratio, or the ratio of a sample's initial to final length after stretching, in an effort to align and crystallize the polymer chains and thereby increase κ. Several studies have focused on polyethylene[8–10], with the highest draw ratio achieved reaching a factor of 350, which resulted in values of $\kappa > 40$ Wm^{-1}K^{-1}[11]. More recently, the highest experimental thermal conductivity for any polymer was reported by Shen et al. in polyethylene nanofibers with a value of $\kappa \sim 104$ Wm^{-1}K^{-1}[12]. While the 2 to 3 order of magnitude improvement over unoriented polyethylene is remarkable, it is important to increase the thermal conductivity of macroscopic samples as well. The highest values achieved in bulk thin films of polyethylene have been $\kappa \sim 65$ Wm^{-1}K^{-1}[13, 14], achieved by using high molecular weight polymers and optimized fabrication and processing techniques.

One of the reasons polyethylene has achieved such large values of κ is thanks to its semi-crystalline structure, even when unoriented[15]. While chain alignment provides the stronger bonds over which transport can occur, a crystalline structure limits the scattering that is inherent to disordered materials. Many other works have examined the thermal conductivity in a variety of other ordered materials, including semi-crystalline polymers like polyacetylene[16] or polymer fibers like Kevlar[17]. Additionally, several works have also shown that significant improvements to κ can be achieved in highly oriented amorphous polymers[18]. Singh et al. reported an improvement in highly oriented amorphous polythiophene by a factor of more than 20 times[19]. In a semi-crystalline polymer like polyethylene, these thermally conductive amorphous regions can contribute to the improved conductivity as well[14, 15, 20].

While crystallinity is certainly important for achieving high thermal conductivity, numerous works have quantitatively shown that both the crystalline fraction and crystal domain size are important factors for achieving high thermal conductivity[11, 13, 21, 22]. Especially at high draw ratios, crystallinity can increase, which is what enables the exceptionally high values of κ that have been reported.

Many of the experimental studies discussed so far have tried to relate differences in thermal transport to microscopic properties and mechanisms. For example, in highly oriented semi-crystalline polymers, phonons are the dominant heat carriers.

In general, thermal conductivity as caused by phonons is described according to the kinetic equation

$$\kappa_i = \frac{1}{V} \sum_\lambda C_\lambda v_{i,\lambda} \Lambda_{i,\lambda} \tag{1.1}$$

where κ_i is the thermal conductivity in direction i, V is the volume, λ refers to a specific phonon mode, C_λ is the phonon mode's heat capacity, $v_{i,\lambda}$ is the group velocity in direction i, and $\Lambda_{i,\lambda}$ is the component of the mean free path (MFP) in direction i. Knowledge of the parameters in Eqn. 1.1 fully determines the thermal conductivity, but also provides insight into which phonons contribute how much to heat conduction, and how far they travel between collisions. This type of information, however, is extremely difficult to access experimentally because experimental observables are typically averaged over the broad phonon spectrum. As a result, oriented polymers have been studied extensively with theory and simulation in an effort to understand the microscopic processes governing thermal transport.

Computational techniques can provide such information for a variety of atomic structures, including perfect polymer crystals. For example, ab-initio calculations have been used to study a perfect polyethylene crystal[23], fully predicting all of its phonon properties. A recent ab-initio study calculated the polyethylene crystal to have a maximum thermal conductivity of 164 $Wm^{-1}K^{-1}$[24], thus establishing a theoretical upper limit to what could possibly be achieved experimentally.

Additionally, simulations techniques such as molecular dynamics (MD) have been used extensively to study polymer crystals[17, 25–29]. One advantage of these simulations is their ability to analyze microscopic thermal processes and properties at a smaller computational cost than ab-initio calculations, though inaccuracies may arise due to the approximate interatomic potentials. For example, the spectral energy density can be obtained, from which phonon group velocity and information about phonon scattering rates can be determined [25]. Other studies have manipulated the underlying atomic interactions to observe what sorts of molecular interactions correlate with good heat transport[27]. Another beneficial aspect of these simulations is their ability to study and compare many different types of polymers simultaneously in an effort to evaluate the most promising material to study further[25, 26]. By studying idealized structures, the simulations can approximate the polymer's upper limit to κ, which is not easy to do experimentally. Furthermore, by studying the microscopic properties of many polymers together, one can characterize the features that are important for achieving a high thermal conductivity.

1.2 Experimental Methods

While the computational works discussed so far offer a valuable insight into the thermal mechanisms underlying a material's thermal conductivity, it is important to connect these to real world materials with experiments. While experiments are limited in the information they can probe about thermal transport, there have been many methods developed with varying capabilities that can be applied to polymers. We will highlight a select few here. First, there are a number of macroscopic methods capable of measuring macroscopic bulk samples. Most generally work by measuring the transient response of a sample to a heat input. For example, laser flash is one such technique used for oriented polymers that measures how fast a laser-heated area spreads its heat to nearby spots on the sample[13, 30, 31].

Of particular interest are methods that can probe thermal transport at the microscale, which can be applied to either nanostructured materials or used to probe the phonon properties in a material. One such technique used to measure polyethylene nanofibers used a complex setup involving an AFM cantilever connected to the nanofiber, with optical sensing to monitor cantilever deflection in response to temperature changes[12]. A thermal bridge technique has also been used where an isolated strip of the material being measured is suspended between two thermal sinks. Electrical heating and temperature sensing relate the material response to conductivity[32]. These and related techniques have had success in measuring nanoscale samples that are otherwise impossible to measure by conventional means, though their implementation is highly complex and there are numerous sources of error to account for[33–35]. Importantly, they are not applicable for macroscopic samples like films.

Another technique that is used widely for a variety of thermal measurements is time-domain thermoreflectance (TDTR). Briefly, this method works by focusing a short laser pulse to a narrow spot on a sample and observing the resulting temperature profile with a second laser pulse. One work applied this technique to study interfacial thermal conductance in PMMA films, including some partially oriented films known as polymer brushes[36]. However in these examples, the technique is used to measure the cross-plane transport of a material, or a combination of in-plane and cross-plane transport. Cross-plane refers to the direction normal to the surface, while in-plane refers to a direction parallel to the surface of a material.

A technique that has been known in the chemistry community for decades but has not been extensively used in the thermal transport community is Transient Grating (TG)[37–46], which will be the subject of Chapters 3 and 4 of this thesis. Briefly,

this method works by exciting a thermal grating in a sample with two pump laser pulses, and measuring the subsequent decay with a second probe laser. It has been used to study a variety of materials and properties, but we are primarily interested in its ability to study thermal transport. The technique has been applied to polymers like polyimide[47, 48] and PMMA[49] to measure group velocity and thermal diffusivity. Notably, it is an optical, non-destructive technique like TDTR, but it is naturally a fully in-plane measurement, making it especially suitable for measuring films.

Another important experimental capability is MFP spectroscopy, which involves a thermal measurement that can probe the phonon MFP spectrum of a material[50–53]. A variety of experiments are capable of this by changing the length scales of the thermal measurement[35, 51, 54–59]. As the measurement length scale is tuned, the apparent thermal conductivity varies, which can be related to the MFP spectrum[51–53]. Importantly, TG is well suited to MFP spectroscopy, which will be explained at length in Chapter 4.

1.3   Outline of Thesis

In this thesis, we aim to elucidate the microscopic transport processes of phonons in highly oriented polymers through the use of both simulations and experiments. Despite the extensive work over many decades discussed above, the microscopic perspective of thermal conduction required to synthesize polymers with exceptional thermal properties is still lacking. On the computational side, while there exist some criteria for evaluating the potential of a given polymer to possess high thermal conductivity, the desired predictive power is not yet available. Additionally, experimentally probing these microscopic transport processes in real polymer materials has historically been challenging. Filling this gap between computational predictions and experimental verification in real materials would represent a major advance in the physical understanding necessary for the materials science community.

In Chapter 2, we will use molecular dynamics (MD) simulations to study heat transport in crystalline polynorbornene. While guidelines presented in the literature might suggest a high thermal conductivity in this material, MD calculations show that the thermal conductivity is not only low, but barely better than an amorphous material. We explore numerous possible explanations for this unexpected behavior through simulations and various analysis techniques. We identify the origin as due to strong anharmonic interactions that prevent the formation of propagating atomic

waves, or phonons, leading to glass-like thermal conduction. This work identifies an important mechanism that affects the lower limit of thermal conductivity in polymer crystals.

In Chapter 3, we describe the Transient Grating (TG) experiment and discuss the adaptations we made to apply it to polymer films. In particular, we will discuss how to use this technique at sub-µm length scales and in materials with thermal conductivity as low as ~0.1 $\mathrm{Wm}^{-1}\mathrm{K}^{-1}$. This chapter expands on the methodology introduced in past literature and explores the many modifications and details required to successfully implement TG, especially for the work discussed in Chapter 4.

In Chapter 4, we will apply the TG technique to highly oriented polyethylene (PE) films. The primary objective of this chapter will be to discuss MFP spectroscopy, where TG measurements at length scales comparable to phonon MFPs are used to reconstruct the MFP spectrum in various PE samples with different microstructures. We will explain how this technique works as well as the details of the MFP reconstruction. Additionally, we explain the structural characterization used, which is important for interpreting results about thermal transport. Finally we will explore the implications of the MFP spectrum, including how it relates to thermal transport and the morphology of the highly oriented PE films.

Finally, Chapter 5 summarizes the key results of the thesis. Further, we will place the conclusions in the context of the greater field and discuss what directions are most promising for future study.

Chapter 2

CRYSTALLINE POLYMERS WITH EXCEPTIONALLY LOW THERMAL CONDUCTIVITY STUDIED USING MOLECULAR DYNAMICS

This chapter has been adapted, in part, from:

> Robbins, A. B. & Minnich, A. J. Crystalline polymers with exceptionally low thermal conductivity studied using molecular dynamics. *Applied Physics Letters* **107,** 201908 (Nov. 16, 2015).

Atomistic simulations remain an invaluable tool for studying heat transport in a diverse group of materials. While simulations have their limitations and are only as valid as the underlying physics they are built on; when well constructed, their use can offer numerous benefits. For example, it is relatively easy to compare different materials or vary conditions such as temperature or pressure. More importantly, simulation at the atomic scale allows for direct access to microscopic information that is difficult to access experimentally.

Of particular interest in this chapter is the use of molecular dynamics (MD) simulations on polymers. MD simulates the classical motion of atoms with a specified interatomic potential. Recent years have seen the frequent application of these simulations to a variety of polymers, particularly to assess their potential for exceptionally high thermal conductivity. In this chapter, we will apply MD simulations to a polymer called polynorbornene (PNb). We will begin by discussing how MD has been used to study heat transport in polymers in the past, and what insights were learned. Then we will describe MD and its implementation in greater details. Next, we will show that MD predicts PNb to have a very low thermal conductivity, despite what would be expected based on previous literature. Finally, we will demonstrate that heat transport in this material is fundamentally different from previously studied polymer crystals, behaving thermally as a glass.

2.1 Background

Numerous studies have used MD simulations to better understand the improved thermal conductivity of aligned polymers[17, 25–29]. Covering a variety of polymers,

these studies have tried to establish theoretical upper limits to thermal conductivity across different materials. Beyond that, many have sought to identify molecular features that enable better heat transport. First among these molecular characteristics is the polymer backbone bond strength[25]. Relatively strong bonds along the backbone chain can result in higher group velocity, which directly leads to higher thermal conductivity. For example, an all-carbon backbone like polyethylene would be expected to exhibit a higher thermal conductivity than a silicon-oxygen backbone like polydimethylsiloxane (PDMS). Second, numerous works have identified the importance of chain segment disorder [25, 27, 61]. Such disorder involves the random rotation of segments along a polymer chain. Essentially these chaotic deviations disrupt the ideal translational symmetry of the crystal, causing increased phonon scattering and thus decreasing the thermal conductivity.

We sought to use MD on a polymer that had not been studied in the thermal transport literature that could also be experimentally measured. While many polymers thus studied have no shortage of experimental analogs, there is a significant gap between sample quality in experiments and simulations. The MD simulations mentioned above all study perfect crystals or individual isolated chains. While these systems are useful to study for a number of reasons, it is very challenging or impossible to experimentally make a single polymer crystal of these materials, let alone a fully isolated single chain. If an experimental study of a thermally conductive polymer could be successfully replicated in simulation, the molecular-scale insights provided by simulations could greatly enhance understanding of experimental results.

In this chapter we study polynorbornene (PNb). The molecular makeup and crystal structure of PNb can be seen in Figure 2.1. The unit cell of PNb consists of five-membered singly-bonded carbon rings, connected to each other by carbon-carbon double bonds. We chose to study this polymer because PNb and its derivatives have been experimentally grown as a polymer brush[62] via a synthesis technique known as surface-initiated ring-opening metathesis polymerization (SI-ROMP)[36]. In this growth technique, polymer chains are uniformly grown from a substrate to some desired length. Thus each individual chain is attached at one end, and free at the other, thus "polymer brush". When densely grown, it has the ability to form a polymer crystal with a structure that matches MD simulations. In this chapter, due to the unexpectedly low thermal conductivity in PNb, we limit our scope to simulation studies only. However the atypical thermal behavior of this polymer crystal compared to all others thus studied make it particularly useful in better
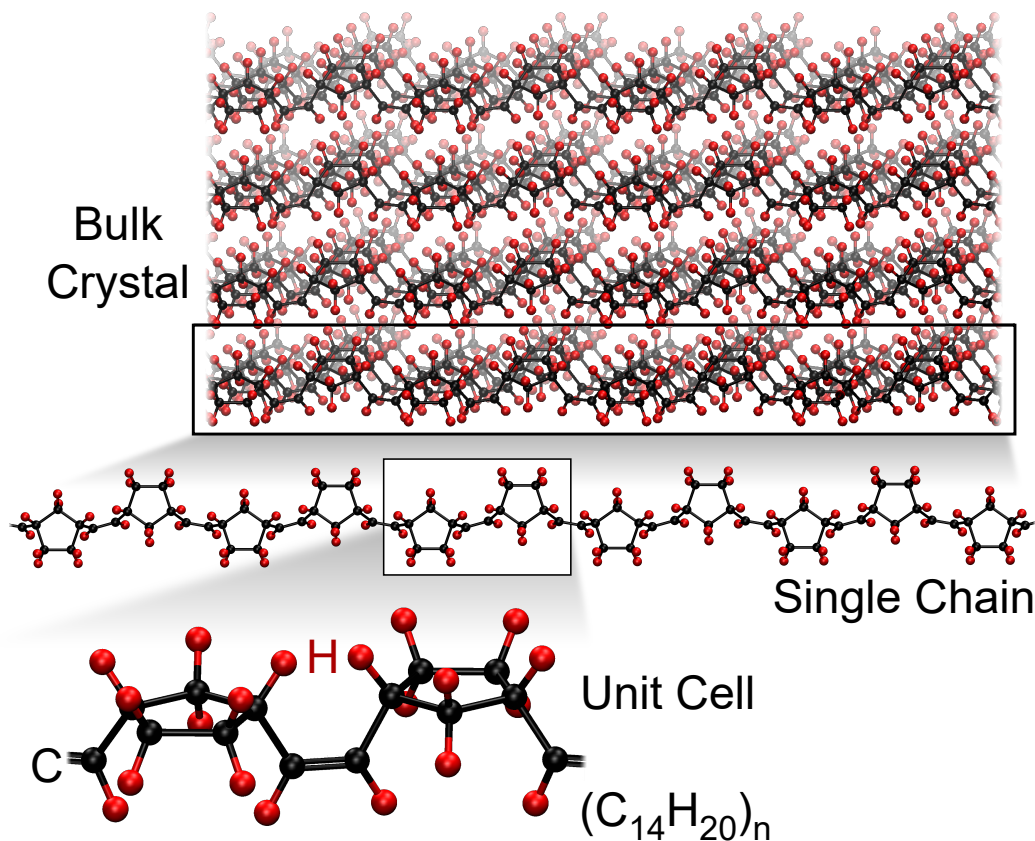
Figure 2.1: Illustration of a PNb crystal, a single polymer chain, and the PNb unit cell, composed of carbon (black) and hydrogen (red) atoms only.

understanding the molecular features that enable or limit high thermal conductivity.

2.2 Molecular Dynamics

All results presented in this chapter were obtained from molecular dynamics (MD) simulations performed with the Large-scale Atomic/Molecular Massively Parallel Simulator (LAMMPS), developed at Sandia National Labs[63]. This section describes the basic principles of MD and how it is implemented in this work. Further details and parameters, as well as validation of these simulations, is available in section 2.3.

MD simulations require as input a fully defined atomic structure, the atomic bonds that are present, a force field to govern atomic interactions, thermodynamic variables such as a temperature and pressure, and boundary conditions. The simulation is progressed in time by moving forward by some timestep dt, chosen fine enough to reduce numerical errors. At any timestep, the force on every atom is calculated.

Then, its position and velocity are updated according to the current force and the atom's previous position and velocity. In this chapter, all simulations were run with a timestep $dt = 1$ fs. The lowest relevant timescale of the system corresponds to the carbon-hydrogen stretching mode, with a period of just over 10 fs. Thus, 1 fs is small enough to capture this motion.

We studied both single chain PNb and bulk crystalline PNb, with the initial unit cell built from previous experimental characterization[64]. Periodic boundary conditions were used to simulate an effectively infinite material. The force field used to govern atomic interactions was the polymer consistent force field (PCFF)[65]. This relatively complex force field incorporates 2-, 3-, and 4-atom energy terms which incorporate bond lengths, bond angles, dihedral angles, and improper (out-of-plane) angles. Further, the force field also contains cross terms for all of these quantities, such as an energy term that accounts for the interaction of bond stretching with bond angle stretching. It also accounts for van der Waals interactions and Coulombic interactions. In total, there are 13 distinct types of energy terms that contribute to the calculated potential energy of the structure. This force field and these many terms make it far more applicable than its alternatives when it comes to thermal transport simulations. Other force fields that may be more accurate for other properties, like lattice constant, lack the detailed energy landscape that is essential for heat transport calculations.

To run a simulation, the specific structure being studied must be equilibrated to the desired temperature and pressure (or volume). Initial atom positions are estimated with that goal of approximating the equilibrated structure. For example, bond lengths and angles are chosen based on known equilibrium quantities for similar structures, and unit cell sizes are chosen based on literature values. As a result, the equilibration process needs to explore only a small portion of the energy landscape.

Equilibration is accomplished in three main steps. First, an energy minimizer is run to find a potential energy minimum, effectively at 0 K. This avoids an atom "flying away" if it is accidentally in a position where it has a large force on it. Second, the system is run in an NPT ensemble. In this stage of the simulation, the system is put into "contact" with a temperature reservoir and a pressure reservoir. Energy is added to individual atoms to ensure the overall kinetic energy reflects the desired temperature. Similarly, the volume is varied to ensure the desired pressure of the system is reached. Also, because the system begins at 0 K, with all atoms stationary, the temperature is slowly increased. As the system heats up, kinetic energy is

explicitly added, which then flows into potential energy. Thus the system is allowed to equilibrate at the desired temperature until the total energy stabilizes. Finally, in step 3 the entire system is run in an NVE ensemble, where the total energy and volume are fixed, which amounts to an adiabatic, rigid box. This step is required because the external thermostat may excite modes of heat transport, such as certain phonon modes, that are out of equilibrium. This is equivalent to a real system in contact at an interface with a thermal reservoir, where the thermal vibrations injected at the interface do not reflect the equilibrium distribution of the bulk material. By running the simulation for an extended period of time after removing the thermal reservoir, the system can reach a natural thermal equilibrium.

There have been two main techniques for calculating thermal conductivity in MD simulations. First are non-equilibrium techniques, which are straightforward in that they apply a temperature gradient and measure the resulting heat flux, or vice versa. From Fourier's Law, $J = -\kappa \nabla T$, the thermal conductivity can be determined. The second technique, which is used exclusively in this chapter, is an equilibrium technique which uses the Green-Kubo equation. Here, the system is left completely isolated running in an NVE ensemble. Thus the entire system is at a constant temperature. Just as there are natural temperature fluctuations in a material at a finite temperature, there are natural fluctuations in the heat flux. These fluctuations can be directly related to thermal conductivity by the following equation:

$$\kappa_z = \frac{V}{k_B T^2} \int_0^\infty \langle J_z(0) J_z(t) \rangle dt \tag{2.1}$$

This equation is derived from the fluctuation-dissipation theorem and states that the autocorrelation of the global heat flux in a system is proportional to the thermal conductivity. Note also that if thermal conductivity is anisotropic, this formalism can simultaneously identify the full tensor by isolating the different components of the heat flux. As we deal exclusively with fully oriented polymers in this chapter, we will only be interested in the thermal conductivity in the z direction, corresponding to the chain direction of PNb.

Lastly, in addition to studying PNb, we also study polyethylene (PE). Because this polymer has been studied extensively already, it allows us to verify our methods by reproducing others' work. Second, PE provides a direct comparison to PNb. We study both single chains and bulk crystalline PE, using identical techniques for both. As a result, we will focus on PNb, but will frequently quote or show PE data for comparison.

2.3 MD Validation

While the methodology for setting up MD simulations and calculating thermal conductivity is fully laid out in Section 2.2, there are numerous parameters and details that must be validated to ensure an accurate simulation. Like other simulation and calculation techniques, faulty assumptions can lead to erroneous results, even if the results appear "right". As a result the validation process is incredibly important.

Limitations of Molecular Dynamics Simulations

There are some sources of error that are simply intrinsic to the use of MD simulations. One potential source of error in any MD simulation is the force field used. In this work, the use of the PCFF is certainly not perfect, however it is the best available for studying heat transport in polymers and has many examples of reasonable findings in the literature. It is important though to acknowledge the error when considering precise numbers reported from MD. For example, calculations on PE from other works[25, 27] and this thesis put the upper limit on thermal conductivity lower than the value reported from ab-initio calculations[24] and experimental studies[12].

The other significant limitation of the simulations discussed here are their classical nature. Especially when studying light atoms, quantum effects can be important, even at room temperature. The heat capacity, for example, will be incorrect in classical MD simulations. However, the value from using MD comes more from its ability to compare materials and look at atomic-scale processes that are otherwise inaccessible. Thus, results presented in this work emphasize trends, comparisons, and molecular-scale mechanisms. Despite the limitations discussed here, many important questions can still be addressed using MD.

Timestep

Considering now the various choices of parameters in setting up our simulations, we begin with the timestep dt. If the simulation is run too coarsely such that a heat carrying vibrational mode is distorted by numerical artifacts, transport via this mode and any scattering processes this mode is part of will be affected. While the timestep of $dt = 1$ fs was chosen specifically to capture the fastest vibration known to the system (carbon-hydrogen stretching), we test this choice by running numerous identical simulations where dt is varied systematically. By calculating thermal conductivity in each of these simulations, we may compare and observe if the value is converged for our choice of dt. Figure 2.2 shows that at 1 fs and lower, there is no significant variation in the calculated thermal conductivity, which verifies
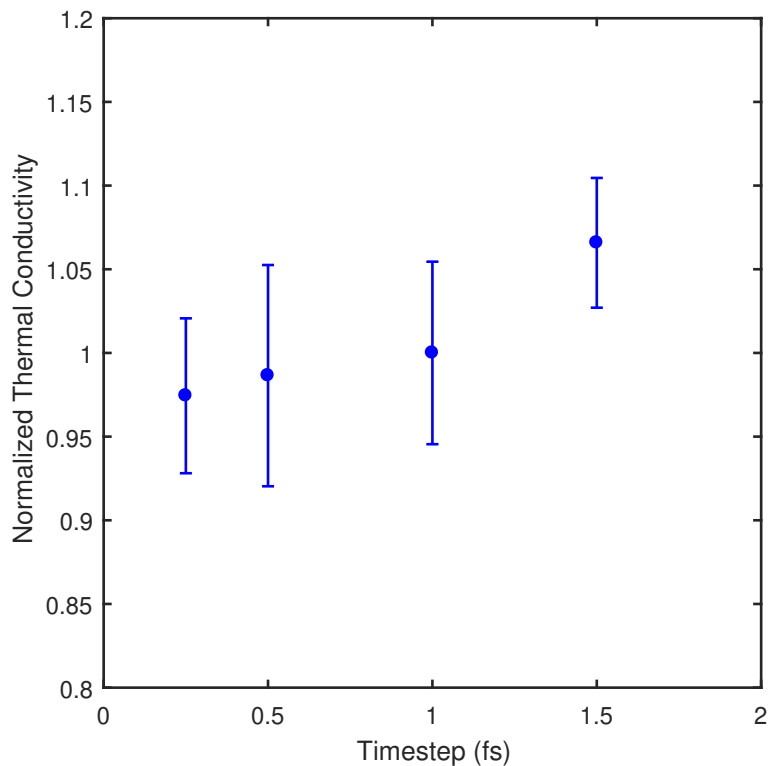
Figure 2.2: Calculated thermal conductivity of bulk PNb crystal as a function of simulation timestep. All simulations use a timestep of 1 fs. This plot shows that 1 fs is short enough to reach the converged thermal conductivity value.

that our choice of dt is acceptable to yield a converged thermal conductivity.

Equilibration

Next, we consider the equilibration process used in these simulations. The early equilibration steps are meant to inject enough energy into the system to achieve the desired temperature. The NPT equilibration step (step 2) is run long enough such that the pressure, temperature, and total energy of the system is stabilized. All of these quantities are calculated at every timestep and thus can be easily monitored for stability. The final equilibration step, where the system is run in an NVE ensemble to allow all thermal excitations to relax, can affect the final calculation. In general, any given vibrational mode in the system will have some corresponding decay time. Ideally, the final equilibration step would be run several times longer than the slowest vibrational decay time in the system. Again, it is easy to verify stability here by comparing multiple simulations where this time duration is varied. Following all these checks, there was no significant variation observed and the NPT steps were run for 50 ps and the NVE steps were run for 10 ps.
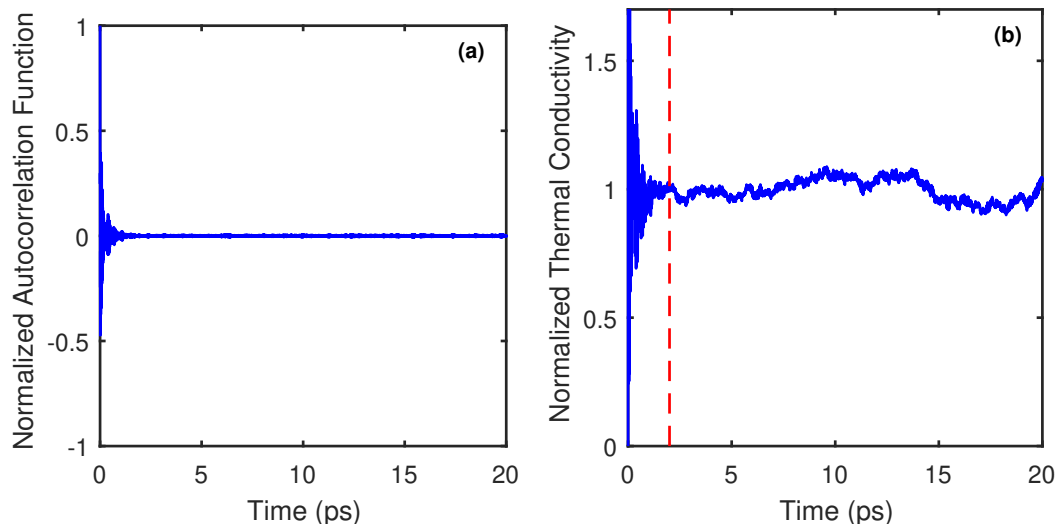
Figure 2.3: (a) Heat flux autocorrelation function in a bulk PNb crystal at 300 K. There is clearly a nonzero correlation of heat flux below 1 ps, though it decays sharply after that. (b) Evaluated Greek-Kubo equation yielding thermal conductivity as a function of the upper bound of integration. This is the integral of (a) multiplied by the appropriate constants. The value is mostly stabilized by 2 ps, which is the upper bound cutoff used in all simulations when evaluating the integral.

Green-Kubo Method

The most important parameters to verify are those associated with the Green-Kubo implementation. While Eqn. 2.1 appears straightforward, the autocorrelation integral involves some subtle considerations for a finite numerical simulation. First, the integrand of Eqn. 2.1 contains an ensemble averaged expectation value. To avoid running a prohibitively large number of simulations, the ensemble average is substituted with a time average. By running a simulation for a long enough duration, uncorrelated ensembles at different points in time are averaged to compute the autocorrelation integrand. Most simulations in this chapter used a duration of 3 ns.

The second consideration for the Green-Kubo calculation involves the integral in time up to $t = \infty$, which is not possible in a finite simulation. However the integrated quantity represents the autocorrelation of heat flux in time, which will eventually go to 0 (faster for lower values of κ). Thus we can truncate this integral after the correlation has fully disappeared. Figure 2.3(a) shows an example of the autocorrelation integrand of Eqn. 2.1 as a function of time. While transient features are apparent for times less than 1 ps, the function largely decays to 0 after this time. Figure 2.3(b) shows full Green-Kubo integration as a function of the upper integration bound. By approximately 2 ps, the thermal conductivity value is largely

stabilized, however minor deviations from 0 in the integrand can add up leading to uncertainty in the evaluated integral. A different choice of the upper bound in time to cut off the integral would lead to different values. To avoid any bias, an upper bound of 2 ps is always used when calculating the thermal conductivity for PNb.

Finally, because noise is an intrinsic part of these simulations, and there is clearly uncertainty based on the integral cutoff time and the time-averaged autocorrelation function, we average computed thermal conductivity values from 5 independent simulations. The error bars presented represent the standard deviation of these independent simulations.

Also relevant to validation of our techniques is the study of PE. We carried out all the same validations steps discussed above on PE. Our approach was further validated because our computed thermal conductivity values for PE are in agreement with prior reports[11, 12, 25–27]. Based on this agreement, we assume our approach is also valid for PNb.

2.4 Thermal Conductivity of Polynorbornene

We now present the first thermal conductivity results for PNb. To start, we look at κ as a function of chain length. While we are using periodic boundary conditions, a small simulation size will allow a given thermal vibration to wrap around and interact with itself, which would be unphysical. Thus we must use a chain length corresponding to a converged value of κ. As an aside, any deviations at lower length scales from the converged value do provide a qualitative measure of how far individual modes can travel before scattering. Figure 2.4 shows results for both single chain and bulk PNb at 300 K. What we can first notice is a lack of length dependence. There may be a slight dependence for the single chain, though it is not statistically significant. All subsequent simulations use a chain length of 50 nm, which corresponds to converged values.

The other feature we can consider from these initial results is the extremely low thermal conductivity values they yield. The bulk PNb crystal has a value of $\kappa = 0.72 \pm 0.05$ Wm^{-1}K^{-1}. For reference, the value in the perpendicular direction was 0.25 ± 0.03 Wm^{-1}K^{-1}, which provides an estimate of the lower limit set by the weak inter-chain interactions. Thus we see only a factor of 3 increase at most for a perfect oriented crystal. In contrast, we performed an identical simulation on polyethylene (PE), which yielded a value of 76.0 ± 7.2 Wm^{-1}K^{-1}, which agrees well with prior works[11, 12, 25–27].
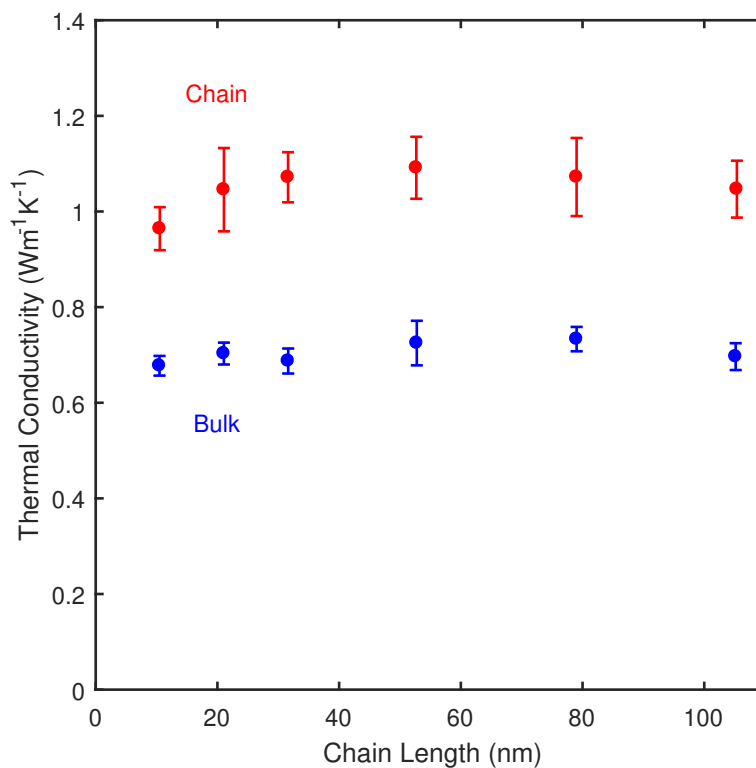
Figure 2.4: Thermal conductivity as a function of chain length for both a PNb bulk crystal and single chain. There is no significant length dependence, so a value of 50 nm is chosen for all subsequent simulations, which is certainly large enough to avoid any size effects.

Values for the single chain PNb are marginally higher than the bulk, which is typical because neighboring chains provide more opportunities for scattering of heat carriers. However it is clear that both PNb structures have intrinsically low thermal conductivity, unlike many of the other polymers that have been reported.

Temperature-Dependent Thermal Conductivity

We next consider the temperature dependence of PNb, shown in Figure 2.5(a). The thermal conductivity has only a weak dependence on temperature, increasing slightly over the range studied. This trend is actually characteristic of amorphous materials at these temperatures. Many other crystals, PE included, exhibit a decrease in thermal conductivity with temperature due to increased phonon-phonon scattering, as shown in Figure 2.5(b).

These initial results for PNb are unexpected and anomalous in the context of the other reported oriented polymer studies discussed earlier. The thermal conductivity
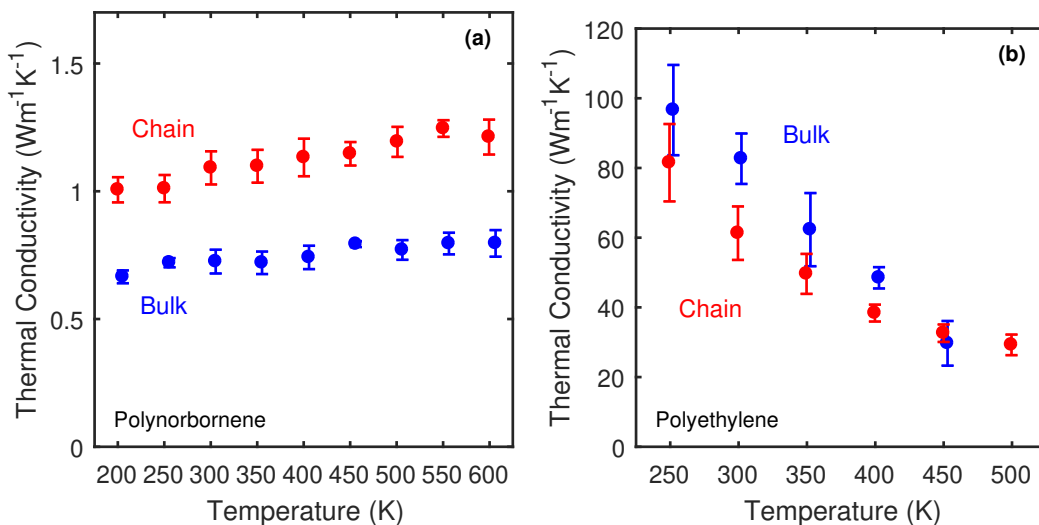
Figure 2.5: (a) Thermal conductivity as a function of temperature for both a PNb bulk crystal and single chain. There is a slight increase with temperature, which is characteristic of amorphous materials. (b) Thermal conductivity vs temperature for PE bulk crystal and single chain. Unlike PNb, PE thermal conductivity decreases with temperature, as is characteristic for crystals that are dominated by phonon-phonon scattering.

is not significantly enhanced with chain alignment, and the temperature dependence resembles an amorphous material. The remainder of this chapter will seek to explain these unexpected results and reveal why chain alignment and crystallinity do little to enhance κ in PNb.

2.5   Explaining Low Thermal Conductivity in Polynorbornene

To explain our unexpected calculations for PNb, we first consider our underlying assumptions. While we begin our simulation with a perfectly crystalline atomic structure, we have no evidence thus far that it remains crystalline. While unlikely, it is possible the structure transformed during the equilibration process while the volume was not rigid. To evaluate the crystallinity during the Green-Kubo implementation, we simply record the atom positions simultaneously. With the recorded atomic positions, we simulate taking an X-Ray Diffraction (XRD) pattern on the structure. This amounts to a spatial Fourier Transform. From these results, shown in Figure 2.6, we see that we have well-formed peaks, characteristic of a crystalline material.

We next consider other factors established in the literature that could explain a low thermal conductivity. As discussed in Section 2.1, one important factor is the composition of the polymer backbone. Strongly bonded, light atoms contribute to
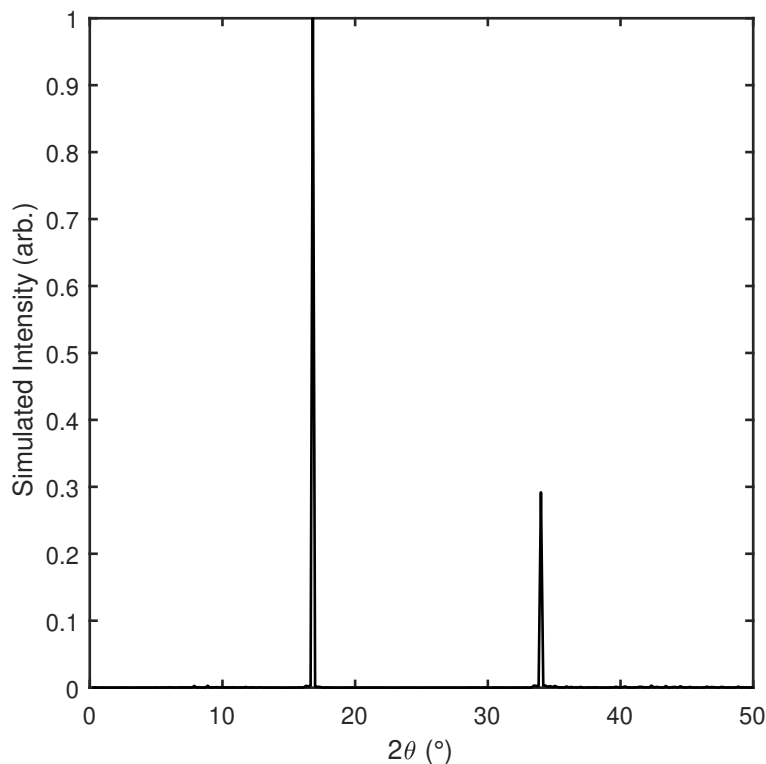
Figure 2.6: Simulated X-Ray Diffraction Pattern on bulk PNb crystal at 300 K in the z-direction. This pattern shows a fully crystalline structure.

a high group velocity. In our case, we have an all carbon backbone chain. There is even a rigid double bond as well. Thus this criterion is satisfied for PNb. A related factor is the presence of mass mismatch along the chain, which can disrupt vibrations. However again this does not apply to PNb. Thus these simple guidelines clearly do not hold for PNb.

An additional guideline that can be responsible for lowered thermal conductivity is segment chain disorder, which refers to segments of a polymer chain chaotically rotating out of their equilibrium positions. An example is shown for PE in Figure 2.7(a). The rotation occurs around a single bond, with the angle of rotation being known as the dihedral angle. In PNb, the 5-membered carbon ring and the double bond constrain much of the chain's ability to rotate its segments. However, there is one bond where such segment rotation may occur, highlighted in Figure 2.7(b). To affect thermal conductivity, rotation about this dihedral angle does not need to involve large angles, such as 180°. If the dihedral angle is soft enough, there may be a wide distribution about the equilibrium value such that thermal conductivity is affected. Rather than quantify what "wide enough" may refer to, we can
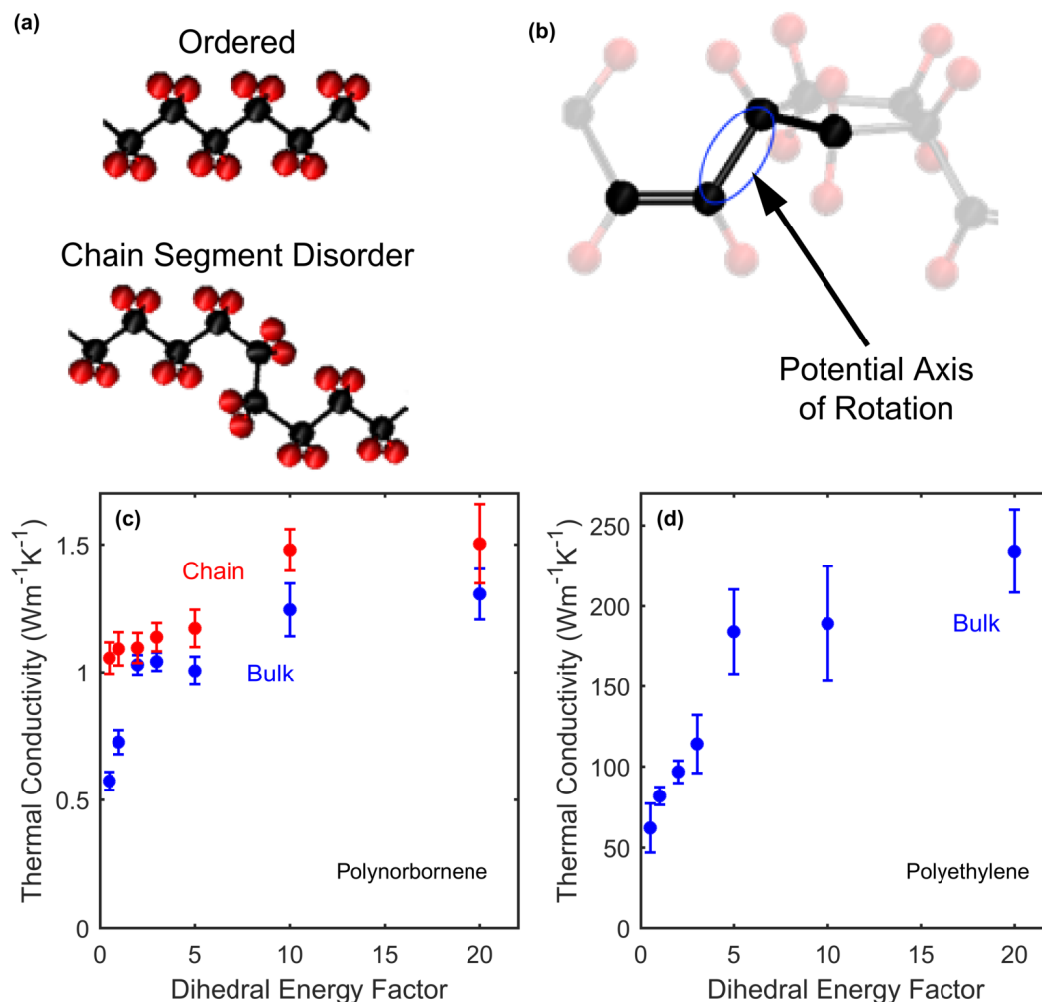
Figure 2.7: (a) Example of an ordered and a disordered polyethylene chain. In the disordered chain, a segment of the chain has rotated, thus disrupting the translational symmetry. (b) In this unit of polynorbornene, there is only one bond around which the chain can rotate freely, which is highlighted here. The angle of rotation around this bond is referred to as a dihedral angle. (c) Thermal conductivity calculations on polynorbornene bulk crystals and single chains as a function of dihedral energy factor. Larger factors correspond to an artificially stiffer energy surface corresponding to the dihedral energy in (b). (d) Same as (c), but for a polyethylene bulk crystal.

directly measure how important rotation about this angle is by artificially softening and stiffening it and observing the effect on thermal conductivity.

To observe the relationship between dihedral angle stiffness and thermal conductivity, we consider the force field. As previously mentioned, the force field used here has a dedicated term for dihedral angles. This term assigns an energy penalty

as a function of the amount of rotation around this dihedral. When implementing an MD simulation, these energy terms can be artificially increased or decreased in magnitude, changing the energy landscape. Zhang et al.[27] used this technique on PE, finding that despite its already large thermal conductivity value, chain segment disorder was a source of significant thermal resistance. We use a similar technique for PNb (and PE for reference) shown in Figure 2.7(c) and (d). In these plots, the x-axis represents the multiplicative factor of the dihedral energy term being studied. At the highest value, $\times 20$, this dihedral angle is exceptionally stiff, essentially fixing it to the equilibrium value. The plot for PNb shows that the bulk crystal's thermal conductivity increases marginally, approaching the single chain value, before leveling off just above 1 $Wm^{-1}K^{-1}$. The single chain value increases to 1.5 $Wm^{-1}K^{-1}$. For comparison, bulk crystalline PE sees an improvement of a factor of 3. While this factor is only a little larger than for PNb, it demonstrates that there is certainly no more segment rotation disorder in PNb than in PE. As a result it does not explain the low thermal conductivity.

At this point, PNb appears to defy all previously established guidelines on which polymers should have a high intrinsic thermal conductivity. As a result, we must employ other forms of analysis to reveal information about the underlying thermal transport in PNb.

2.6 Thermal Carriers in Polynorbornene

After establishing the low thermal conductivity in PNb, and ruling out explanations available in the literature, we next aim to consider what its phonon dispersion looks like. For a crystal, low thermal conductivity is generally a result of low group velocity or significant phonon scattering, both of which can be better understood with the phonon dispersion. We can approximate this by computing the spectral energy density.

Spectral Energy Density

The spectral energy density (SED) resembles a phonon dispersion with thermal broadening, equivalent to the dynamic structure factor measured in neutron scattering experiments. This technique has been used not only to determine a material's effective dispersion, but the lifetime of individual modes in a simulation.[25, 66–68]. The SED is computed in a very straightforward way as a spatial and temporal
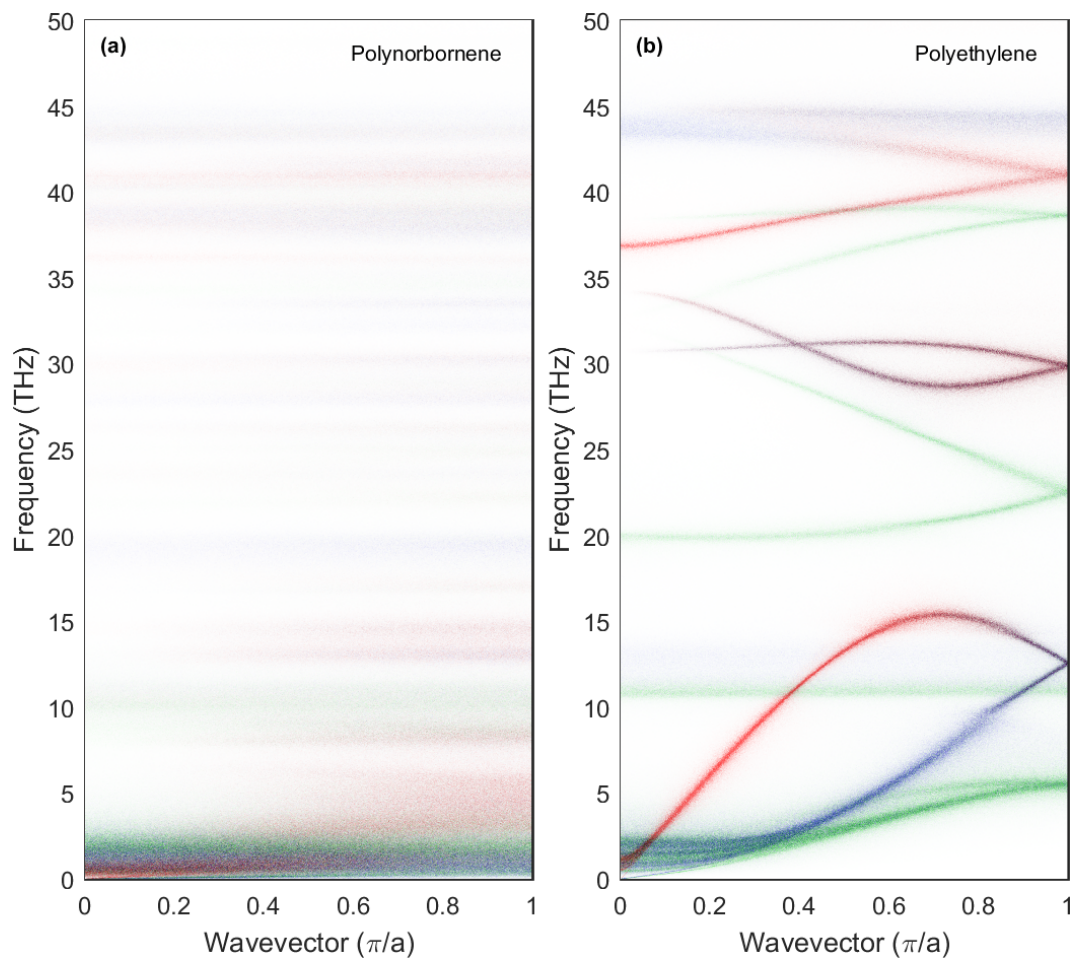
Figure 2.8: (a) Spectral energy density for bulk crystalline polynorbornene at 300 K. (b) Spectral energy density for bulk crystalline polyethylene at 300 K. To avoid washing out dimmer points due to the high brightness at low frequencies, intensities are plotted on a log scale. Further, intensities are normalized to the 99th percentile of the brightest such that the top 1% of intensities appears the same. Additionally, the color of any point is calculated according to the contributions from motion in the x (blue), y (green), and z (red) directions (See Eqn. 2.2). In general, red points represent longitudinal modes with blue/green representing transverse modes.

Fourier transform of atomic velocities over the course of a simulation:

$$\Phi_\alpha(\omega, k_z) = C \sum_{a=1}^{N_a} \left| \int \sum_{n=1}^{N_z} v_\alpha(z_n, t) e^{i(k_z z_n - \omega t)} dt \right|^2 \qquad (2.2)$$

In this equation, ω is frequency, k_z is wavevector, C is a constant, v_α corresponds to the velocity component along the specified axis where $\alpha = \{x, y, z\}$, n is the unit cell index up to N_z unit cells in the chain, and a indexes the backbone atoms within a unit cell up to N_a backbone atoms.

To calculate the SED, a simulation is run in an NVE ensemble for an extended period of time following all of the equilibrium steps. For crystalline PNb, 306 000 atoms were used with a chain length of over 1 μm, and simulations were run for 500 ps. Such a large simulation size and long duration are required to achieve fine enough resolution in k_z and ω.

Figure 2.8(a) shows the intensity in bulk crystalline PNb at 300 K plotted for $\Phi_x(\omega, k_z)$, $\Phi_y(\omega, k_z)$, and $\Phi_z(\omega, k_z)$ in blue, green, and red, respectively. As a reminder the polymer chains are along the z direction. While each directional component is typically combined to provide a single Φ, the anisotropic nature of polymer crystals makes it visually useful to separate out the components, thus highlighting which direction of atomic motion dominates certain modes.

In the case of PNb, the most important feature is the absence of any well-defined modes. There is a blurred background where we would have expected distinct phonon branches. For comparison, Figure 2.8(b) shows an identical calculation for a PE crystal, also at 300 K, where the phonon branches are obvious. The primary heat-carrying mode in PE, the red longitudinal acoustic branch, can be clearly seen. The calculated SED shown here is in great agreement with experimental measurements[69–71], which demonstrates that this technique and the force field used is capable of modelling complex thermal transport.

Zooming into the SED for PNb, Figure 2.9 shows that at low frequency, PNb does contain three well-defined acoustic branches, though only up to a frequency of about 0.25 THz. Beyond this cutoff, the modes seem to lose their wavevector dependence. Different regions seem to be dominated by different directions of motion, as evidence by the different colors, but these do not at all resemble phonon branches.
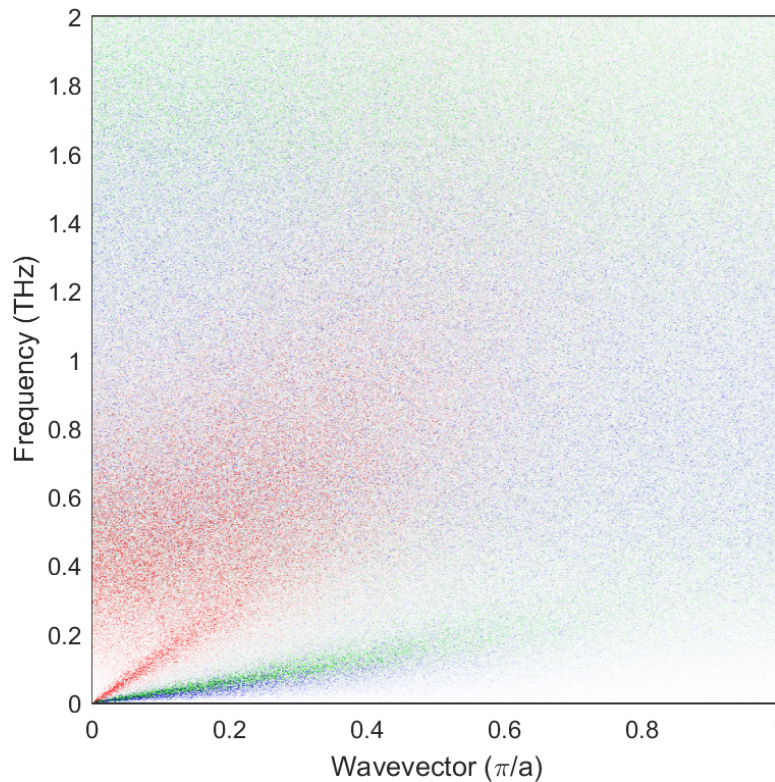
Figure 2.9: Zoomed in spectral energy density of Figure 2.8(a). The only difference is that the intensities are now plotted on a linear scale.

Ioffe-Regel Crossover

This odd transition from recognizable phonon modes to wavevector-independent, poorly-defined modes is known as the Ioffe-Regel crossover[72, 73]. This phenomenon, discovered first in electronic transport, marks the transition from propagating transport to non-propagating transport. Specifically, this crossover occurs when phonon mean free paths (MFPs), ℓ, become so low that they are comparable to the phonon wavelength, λ. When the thermal vibration scatters after traversing only a distance equal to its wavelength, that wavelength cannot be well-defined. This is a fundamental consequence of Fourier transforms and the relationship between spatial resolution and resolution in wavevector space. Note, for linear acoustic branches, this criteria is equivalent to the phonon mode lifetime being on the order of the phonon frequency. In this theory defined by Ioffe & Regel and Allen & Feldman[72, 73], the vibrational modes above the cutoff frequency, which are delocalized, non-propagating vibrations without a wavevector are known as diffusons.

In this theory, where phonons are no longer the only heat carrier, carriers are broken up into three categories: propagons, diffusons, and locons. Propagons are

effectively just phonons, and are only present at low frequencies. Diffusons are non-propagating, meaning they lack a spatial periodicity in their motion. Diffusons can still carry heat, though their effective lack of mobility makes this mode of transport relatively small diffusivity. Finally, there are locons, which tend to be isolated to very high frequency modes. These vibrations are characterized as extremely localized, with the spatial extent of an individual mode being limited to the inter-atomic spacing. For our discussion here, we are most interested in the divide between propagons and diffusons.

Historically, the Ioffe-Regel crossover and the associated discussion of diffusons has been restricted to disordered materials, such as amorphous solids. However, the phenomenon has been observed in perfectly crystalline materials with complex unit cells such as Mn_nSi_{2n-m} and YB_{68}[74, 75]. However this rare phenomenon has not been observed in a polymer before.

Additional evidence for this effect can be gained from the temperature dependence of thermal conductivity, shown previously in Figure 2.5(a). The slowly increasing trend with increasing temperature is characteristic of amorphous materials. Due to the Ioffe-Regel crossover, PNb would be expected to follow this trend rather than the decreasing trend caused by phonon-phonon scattering in crystals.

While the evidence thus far all points to the Ioffe-Regel crossover as the correct explanation, we can evaluate the stated Ioffe-Regel criteria quantitatively. To reiterate, the criterion we are considering is $\ell \sim \lambda$. To evaluate this, we calculate the phonon lifetimes and the MFPs using the SED.

Using frequency-domain normal mode analysis, we can extract a mode lifetime by fitting a Lorentzian profile to a single polarization of the SED[66–68]. To do this, we simply choose a wavevector k_z and take a slice in Φ as a function of ω. The full width at half max of the Lorentzian profile, $2\Gamma_{k_z,j}$, is related to the mode lifetime by $\tau^{-1} = 2\Gamma_{k_z,j}$.

To evaluate a single polarization of the SED, we take advantage of the fact that the longitudinal mode is only composed of motion in the z direction, as evidenced by the longitudinal mode in Figure 2.9 being only red. This allows us to say that $\Phi_{LA}(\omega, k_z) = \Phi_z(\omega, k_z)$ below 0.25 THz. All subsequent fittings and results correspond to the LA polarization in PNb.

Figure 2.10(a) shows an example of a Lorentzian being fit to $\Phi_{LA}(\omega, k_z)$ at $k_z = 0.02\frac{\pi}{a}$. From this fitting, a lifetime is calculated. By multiplying this with the
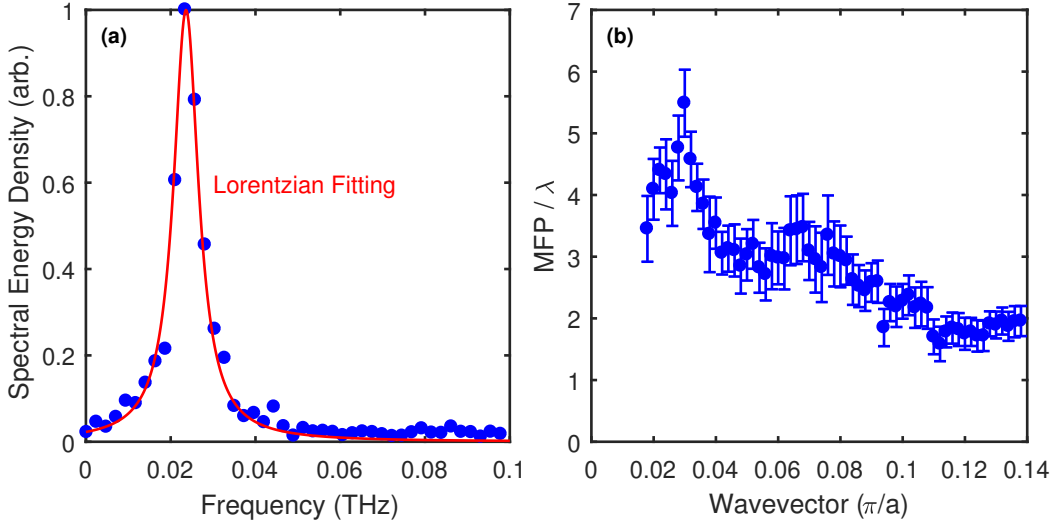
Figure 2.10: (a) Spectral energy density, $\Phi_{LA}(\omega, k_z)$ for the longitudinal acoustic polarization shown in Figure 2.9 at $k_z = 0.02\frac{\pi}{a}$. Each data point represents an average across nearby wavevectors to smooth out the data. The Lorentzian fitting is shown in red and is used to obtain the lifetime of the mode. (b) MFP, ℓ of a mode divided by wavelength, λ where $\lambda = \frac{2\pi}{k_z}$. As this quantity approaches unity, the Ioffe-Regel criteria is met. The error bars correspond to the 95% confidence interval of the Lorentzian fitting.

group velocity of the mode, we compute the MFP, ℓ. The phonon wavelength, λ is simply given by the inverse of the wavevector, k_z. By repeating this procedure at every wavevector along the LA mode until the mode becomes poorly defined, we can plot the ratio of $\frac{\ell}{\lambda}$ as a function of k_z, shown in Figure 2.10(b). This plot clearly demonstrates that the ratio decreases from almost 5 down past 2, before it is too difficult to fit any longer. This unequivocally confirms the Ioffe-Regel crossover condition is being met, resulting in a transition to non-propagating thermal carriers at higher frequencies.

These calculations show that the extremely low thermal conductivity in crystalline PNb is the result of an absence of propagating phonons in the material. Strong scattering results in the Ioffe-Regel phenomenon, a rare occurrence for a demonstrably perfect crystal. While we have fully characterized the heat carriers in PNb and how they limit thermal transport considerably, one may be left asking why PNb exhibits this effect in the first place. Why does it scatter so intensely? The rare examples of the Ioffe-Regel crossover in crystals imply that a large, complex unit cell is a prerequisite. However, quantifying this is difficult, because polymers with even more atoms per unit cell have been shown to have excellent thermal conductivity

with no Ioffe-Regel crossover[25]. We next attempt to quantify the anharmonicty in PNb to see if it is simply prone to higher scattering rates.

2.7 Anharmonicity in PNb

We evaluate the anharmonicity in PNb by considering the Gruneisen parameter. Sufficiently large values of the Gruneisen parameter can suggest significant anharmonicity, at least qualitatively. The parameter is defined as

$$\gamma = -\frac{\partial \ln \omega}{\partial \ln V} \tag{2.3}$$

where ω is the phonon mode frequency and V is the system volume. While γ is different for each mode, we can average over a polarization to get an idea for the anharmonicity of that mode. To study PNb, we consider the same LA mode discussed previously. The Lorentzian fitting already established $\omega(k_z)$ for the mode. To calculate γ, this procedure was repeated at 12 temperatures ranging from 260 K to 400 K. At each temperature, the PNb crystals were relaxed and the resulting volume recorded. The values of $\omega(k_z)$ were fit over the same wavevector range of the LA mode as well. Once this was done for all temperatures, data for $\ln[\omega(k_z, T)]$ vs $\ln[V(T)]$ was linearly fit for a particular k_z to obtain a value of γ at that wavevector. This was repeated at each wavevector.

It is important to note here that the fully correct procedure to make this calculation would not be to vary the temperature, but instead to vary the pressure. The reason for this stems from how anharmonicity causes scattering. In a simplified view, an atomic bond that is stretching from normal harmonic motion will experience a change in its harmonic force constant the more it is stretched, in proportion to the anharmonicity of the bond. Thus, by artificially stretching this bond and observing the change in vibrational frequency, anharmonicity can be quantified. However, accomplishing this via injection of heat can result in additional changes in frequency related to increased thermal motion. While the calculations could not be redone with this in mind due to limited computational resources, we compare results for PNb and PE to obtain a qualitative picture of their relative anharmonicity.

For PNb, we find that averaging over the entire LA mode that $\gamma = -2.8$. Identical calculations for PE's LA mode yield a value of $\gamma = 0.044$. The significantly larger magnitude for PNb implies significantly more anisotropy. Interestingly, the negative value results because phonon frequencies stiffen at higher temperature, rather than soften, which is generally the case.

Due to the likely presence of significant anisotropy in these polymers, we also consider the redefined Gruneisen parameter

$$\gamma_z = -\frac{\partial \ln \omega}{\partial \ln L_z^3} \tag{2.4}$$

where we have replaced the volume term with the dimension in the chain direction. This quantity is arguably more relevant to the modes of transport in the z direction for such an anisotropic material. The re-evaluated value for PNb and PE are -3.9 and -0.32, respectively. Note, PE's value has increased in magnitude, though it is still relatively low. More importantly, it has changed sign, which is a direct result of the negative coefficient of linear thermal expansion in the chain direction. These results suggest that PNb has intrinsically higher anharmonicity, which contributes directly to its increased scattering rates.

2.8 Summary

In summary, we have used MD simulations on PNb chains and crystals to show that it has an extremely low thermal conductivity. Beyond that, we have demonstrated that PNb behaves as a phonon glass, despite its perfectly crystalline structure, and that this is a consequence of the Ioffe-Regel crossover. This is demonstrated not only through its low thermal conductivity value near the amorphous limit, but in its temperature dependence and in its extremely short MFPs. This is likely the result of the high anharmonicity and the complex unit cell of PNb. These findings highlight a previously unconsidered thermal transport mechanism in polymers, demonstrating that some crystalline polymers do not possess intrinsically high uniaxial thermal conductivity. This property may be exploited in applications where increased thermal conductivity is undesirable.

C h a p t e r   3

TRANSIENT GRATING: MEASURING THERMAL TRANSPORT IN POLYMERS

Thermal transport experiments are pivotal for determining the real properties of actual materials, which may deviate from their theoretically predicted values due to differences in microstructure or the presence of defects. While the insights learned from simulations and calculations, as discussed in the previous chapter, are critical for a more fundamental understanding of microscopic heat transport, experiments are an invaluable feedback mechanism in developing synthesis and fabrication techniques, as well as evaluating the true properties of materials of interest.

Our underlying objective in this chapter is to develop a thermal measurement tool to be used on polymer films. However there are a number of requirements we have based on the material system and the specific properties we want to measure. In this chapter, we will begin by discussing the requirements and challenges for measuring polymer films. We will describe the Transient Grating (TG) experiment and how its capabilities compare and contrast with the other available thermal transport techniques in the literature. We will explain, in depth, how the method works, both at a practical level related to the optical setup, and at a fundamental level, including mathematical derivations. We will explain the standard thermal model applied in this and other works, as well as extend our modelling to the more complex thin film geometry. Next we will consider the important considerations necessary to apply this technique to polymer systems. We also include information on practical implementation of the technique. Finally, we present examples of this technique applied to different polymer systems to demonstrate its capabilities.

3.1   Background

Choosing a Thermal Transport Measurement

There exists a multitude of different thermal characterization methods for different types of samples. First, different materials and sample geometries impose different restrictions on the methods used. Second, some methods may yield only thermal conductivity along a particular axis, while others may have the capability to probe a wider range of thermal transport properties. Finally, some measurements are simply

easier or more practically implemented.

For polymer films, there are a number of potential challenges in measuring thermal transport that must be considered when choosing a method. First, we are interested in measuring not only polymer films, but oriented polymer films which are highly anisotropic both in- and cross-plane. As a result, the experimental method must be able to measure in-plane transport along a single dimension, allowing us to isolate transport either parallel or perpendicular to the aligned polymer chains.

Second, we are interested in using phonon mean free path (MFP) spectroscopy to obtain microscopic information about the heat carriers in the sample. MFP spectroscopy involves measuring thermal transport over a range of µm-scale length scales, which means our technique needs to have a tunable length scale on the order of µm's. MFP spectroscopy will be discussed in greater detail in Chapter 4.

Finally, due to the extreme anisotropy in some polymer chains, we need to be able to measure both very low and very high thermal conductivity values. Typically, methods measure the timescale of thermal decay and are best suited to measure a specific range of timescales. However our need to cover an unusually wide range of conductivity values, even on a single sample, means our technique must be compatible with a wide range of timescales.

Many of the experiments used to measure oriented polymers, discussed in Chapter 1, used macroscopic techniques like laser flash[10, 13, 20, 31], which impose heating on macroscopic length scales and observe transient temperature changes on the sample. However, the large length scales used make it unusable for MFP spectroscopy. Several nanoscale techniques have been used for MFP spectroscopy on a variety of non-polymer materials[35]. For example, the 3ω technique[76], which uses electrical contacts on a sample's surface to heat and monitor thermal transport, has been used to probe phonon MFPs[59]. Another technique, time-domain thermoreflectance (TDTR) is one of the most common modern thermal measurement methods[77]. This technique has been used for MFP spectroscopy on several materials as the adjustable heating frequency, similar to 3ω, changes the thermal penetration depth[51, 78–81]. However, these techniques are less applicable for selecting a single in-plane direction for measuring thermal transport. They are frequently used to measure cross-plane transport, or transport in all three spatial directions. Single in-plane measurements for TDTR have been used, though it is a much more complex configuration and analysis[82, 83].

Meeting all of the above requirements is the Transient Grating (TG) method. Explained in depth in the next section, TG is a non-linear optical technique capable of monitoring a variety of dynamics down to picosecond timescales and lower. The technique was largely developed in the 1980's[37]. TG was used to study a wide variety of physical processes[38], including exciton transport[39], dynamics of gas-phase molecules[40], molecular rotation rates in liquids[41], and of interest here, thermal diffusivity[42, 43]. The same principle has also been used for impulsive stimulated raman scattering in liquids[84]. Since then, the technique has been further improved through the use of heterodyne detection[44, 45, 84], femtosecond pulses[85], and continuously tunable gratings[46]. TG has also already been applied to macroscale thermal transport measurements in some polymer films[47, 48, 86, 87]. Further, it has been used in other materials for MFP spectroscopy[50, 54]. In this work, we build a TG setup that expands on these past developments to meet our above stated goals of measuring thermal transport in phonon MFPs in polymer films.

3.2 Transient Grating Mechanism

At its core, TG is an optical pump-probe experiment, meaning a pump laser pulse causes a thermal excitation in a sample, and a second probe laser measures the material's response. Here we will first consider the pump beam and how it creates the thermal grating on the sample.

The pump laser is a Coherent FlareNX laser with wavelength $\lambda = 515$ nm, ~1 ns pulse width, and a maximum pulse energy of ~300 μJ. The laser is split into two beams and focused towards the sample at angles $\pm\theta$. The pump beam incident on the sample is visualized in Figure 3.1. The electric field profiles of the respective pump laser beams can be written as:

$$E_{pump,\pm} = E_{0p} \exp(i\mathbf{k}_\pm \cdot \mathbf{r} - i\omega t) \tag{3.1}$$

$$\mathbf{k}_\pm = k_0(\sin(\pm\theta)\hat{x} + 0\hat{y} + \cos(\pm\theta)\hat{z}) \tag{3.2}$$

where E_{0p} is the magnitude of a laser's electric field before the sample, k_0 is the scalar wavevector of the pump laser given by $k_0 = \frac{2\pi}{\lambda}$, and ω is the frequency of the light. Note, we have simplified our treatment here by considering the lasers as plane waves. For the purposes of understanding TG and modelling thermal transport in most samples, this assumption is valid. Finite beam sizes are considered in Sections 3.6 and 3.7.
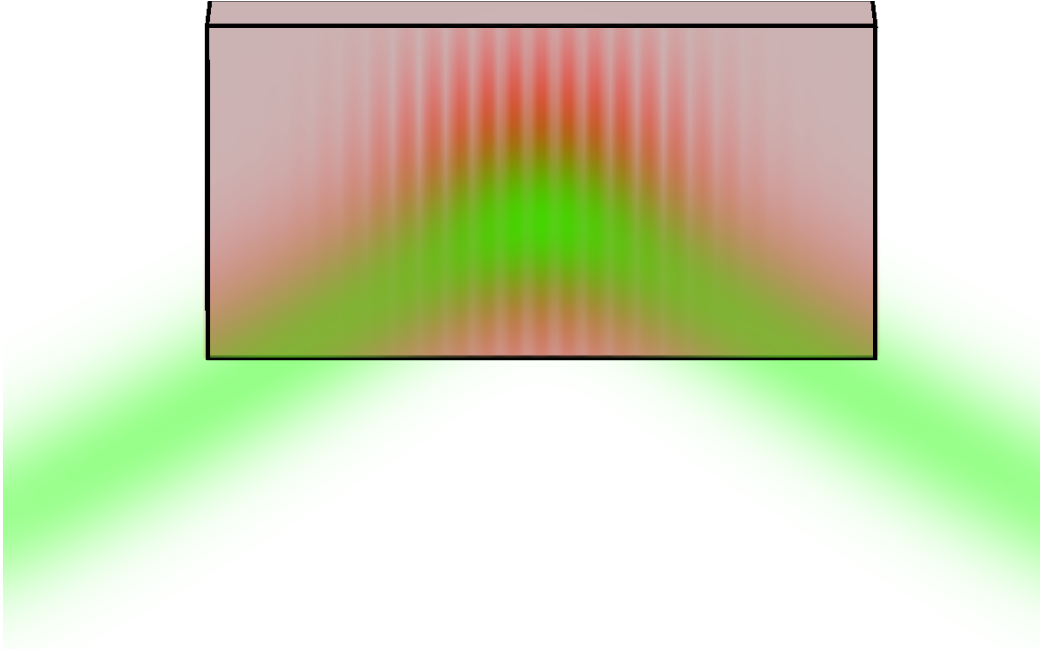
Figure 3.1: Schematic of the 2 pump laser beams overlapping on the sample in the TG experiment. The pair of pump lasers creates the thermal grating that can be seen on the sample.

At the sample, we compute the overall intensity of our two beams:

$$I_{pump} = |E_+ + E_-|^2 \tag{3.3}$$

$$I_{pump} = 2E_{0p}^2(1 + \cos(2k_0 \sin(\theta)x)) \tag{3.4}$$

The cos(...) term of this intensity profile is what creates the grating on the sample. From this, we may define a grating wavevector and a grating period:

$$q_x = 2k_0 \sin(\theta) = \frac{4\pi \sin(\theta)}{\lambda} \tag{3.5}$$

$$d = \frac{2\pi}{q_x} = \frac{\lambda}{2 \sin(\theta)} \tag{3.6}$$

As this intensity profile is absorbed by the sample, this intensity grating becomes a thermal grating.

$$\Delta T(x, y, z) \propto I_{pump}(x, y, z) \tag{3.7}$$

$$\Delta T(x, y, z) \propto 1 + \cos(q_x x) \tag{3.8}$$

3.3 Heterodyned Probe Detection

We next consider how the probe laser is used to measure the thermal grating and its subsequent decay. The probe laser is a Coherent Sapphire laser with wavelength

$\lambda = 532\,\text{nm}$ and is a CW (continuous) laser with a maximum power of $330\,\text{mW}$. Because it is continuous, it measures the sample before, during, and after the pump pulse, showing the formation and decay of the thermal grating in real time.

Like the pump laser, the probe laser is split into two beams, which are focused onto the sample such that all 4 beams (both pump and both probe) overlap at the same sample spot, as can be seen in Figure 3.1. The two probe beams are used in a heterodyne detection scheme, where one beam is used as the "signal" beam, containing the information about the thermal grating, while the second "reference" beam is used to amplify the signal.

Importantly, the probe beams are incident on the sample at the Bragg angle, $\pm\theta_B$, such that the signal beam diffracts off of the thermal grating[1]. More precisely, the thermal grating manifests as a grating in the complex index of refraction of the material, related by material constants like the thermo-optic coefficient. It is the optical grating that diffracts the electric field. This electric field profile of the diffracted portion of the signal beam can be written as:

$$E_{sig} = \eta(t)E_{0r}\exp(i\mathbf{k}\cdot\mathbf{r} - i\omega t) \tag{3.9}$$

$$\mathbf{k} = k_0(\sin(\theta_B)\hat{x} + 0\hat{y} + \cos(\theta_B)\hat{z}) \tag{3.10}$$

$$\eta(t) = \eta'(t) + i\eta''(t) \tag{3.11}$$

where E_{0r} is the magnitude of the probe's electric field before it is diffracted[2], and $\eta(t)$ is the diffraction efficiency. Because the index of refraction is complex, given by $n + ik$, the diffraction coefficient is also complex, given by $\eta'(t)$ and $\eta''(t)$:

$$\eta'(t) \propto \Delta k(t) \propto \Delta T(t)$$

$$\eta''(t) \propto \Delta n(t) \propto \Delta T(t)$$

Both quantities are proportional to the amplitude of the thermal grating referenced in Eqn. 3.8. Also, $\eta(t)$ is a function of time because it is this term specifically which will contain the time-dependent thermal decay we are detecting.

Ignoring the reference beam, we first consider the intensity of the diffracted signal beam:

$$I_{sig} = \left|E_{sig}\right|^2 \tag{3.12}$$

$$I_{sig} = \left(\eta'(t)^2 + \eta''(t)^2\right)E_{0r}^2 \tag{3.13}$$

---

[1] The reference beam will also diffract, but we are not interested in that process.

[2] Some of the laser energy will be lost to reflection and absorption by the sample, which are multiplicative factors that can be incorporated into E_{0r}

Because the diffraction intensity is so small, I_{sig} is difficult to measure. This is where the reference beam becomes important for the heterodyne detection scheme. We can define the reference probe beam simply as:[3]

$$E_{ref} = \sqrt{f} E_{0r} \exp(i\mathbf{k} \cdot \mathbf{r} - i\omega t + i\phi) \tag{3.14}$$

where f refers to a purposeful reduction in the reference probe beam's intensity using a neutral density filter and typically ranges from 0.01 to 1. This is used to avoid saturating the detector. Because the reference beam was already at an angle of θ_B, it is collinear with the diffracted signal beam. Note also the addition of the phase factor ϕ, which accounts for the arbitrary phase difference between the reference and diffracted signal beams due to their differing optical paths. We now write the combined intensity of the two beams as:

$$I_{het} = \left| E_{sig} + E_{ref} \right|^2 \tag{3.15}$$

$$I_{het} = E_{0r}^2 \left(\eta'(t)^2 + \eta''(t)^2 + f + 2\sqrt{f}(\eta'(t)\cos(\phi) + \eta''(t)\sin(\phi)) \right) \tag{3.16}$$

We can isolate 3 terms of interest in the computed intensity. First is the $\eta'(t)^2 + \eta''(t)^2$ term, which matches the intensity of the signal beam without the presence of the reference, given in Eqn. 3.13. As mentioned earlier, due to $\eta \ll 1$, this term is negligible. The second term, f, is notably constant in time. For our detector, this will present as a constant voltage offset, which can be subtracted electronically. The final terms, which are linear with $\eta'(t)$ and $\eta''(t)$ respectively, are the terms we are interested in. Importantly, we are now able to measure $I \propto 2\sqrt{f}\eta(t)$ rather than $I \propto \eta(t)^2$. This advantage can lead to orders of magnitude increase in the measured signal.

Another important feature of this term is the geometric dependence on ϕ. Typically, the thermal grating will lead to a larger change in either $\eta'(t)$ or $\eta''(t)$, depending on whether the real or imaginary part of the index of refraction is more temperature-dependent, though this is very material-dependent. Signals from $\eta'(t)$ or $\eta''(t)$ are known as amplitude and phase gratings, respectively. For polymers discussed in this thesis, $\eta'(t) \sim 0$, and thus we are only interested in measuring phase gratings given by $\eta''(t)\sin(\phi)$.

To measure the phase grating only, we take data at $\phi = \pm\frac{\pi}{2}$, corresponding to a "+"

---

[3]Again, this equation should have a $(1 - \eta(t))$ term, however $\eta \ll 1$, so it is ignored.

and "-" signal, and then subtract them:

$$I_{het}(\phi = \frac{\pi}{2}) = E_{0r}^2\left(\eta'(t)^2 + \eta''(t)^2 + f + 2\sqrt{f}\eta''(t)(1)\right) \quad (3.17)$$

$$I_{het}(\phi = -\frac{\pi}{2}) = E_{0r}^2\left(\eta'(t)^2 + \eta''(t)^2 + f + 2\sqrt{f}\eta''(t)(-1)\right) \quad (3.18)$$

$$I_{het}(\phi = \frac{\pi}{2}) - I_{het}(\phi = -\frac{\pi}{2}) = 4E_{0r}^2\sqrt{f}\eta''(t) \quad (3.19)$$

where the subtracted signal is now composed entirely of the amplified signal we are interested in. Not only is the heterodyne detection scheme important for amplifying the small diffracted signal, it allows us to extract phase information from the signal as well. This ability is critical because some samples may diffract due to different mechanisms that originate purely from amplitude or phase gratings. More commonly, there will be a phase-independent signal on top of the desired signal, which can result from a number of processes that are independent of thermal transport. However because of the subtraction process of the + and - signals, *all* phase-independent signals are subtracted out, leaving *only* the phase grating signal. Some examples where this is important will be discussed in Section 3.8. Note that there may be sources of other (non-thermal) phase grating signals in certain samples that are not eliminated.

3.4 The Optical Setup: Designing for Polymers and Low Grating Periods

Given the basic working principle of TG discussed in the previous section, we now discuss the TG optical setup implemented in the Minnich Lab at Caltech. Figure 3.2 shows a schematic of the TG experiment, as well as a picture of the setup from our lab.

Transient Grating Telescope

We focus first on the section highlighted in red in Figure 3.2(b), which is shown schematically in Figure 3.2(a), which we will refer to as the TG telescope. This section describes the most important set of optics in the experiment as it splits the pump and probe into two beams each and focuses them at the correct angle onto the sample. Considering first the pump laser, it passes through a phase mask, which is a clear optic with a grating pattern written onto the surface in the form of periodic indentations into the glass. The spatial periodicity of this grating pattern has period d_{PM}, which diffracts the beam into two first order beams. The thickness of the surface indentations is chosen to maximize the first order diffraction efficiency of 532 nm light. The first order diffracted beams are emitted at angles $\pm\theta_1$, according

(a)

(b)
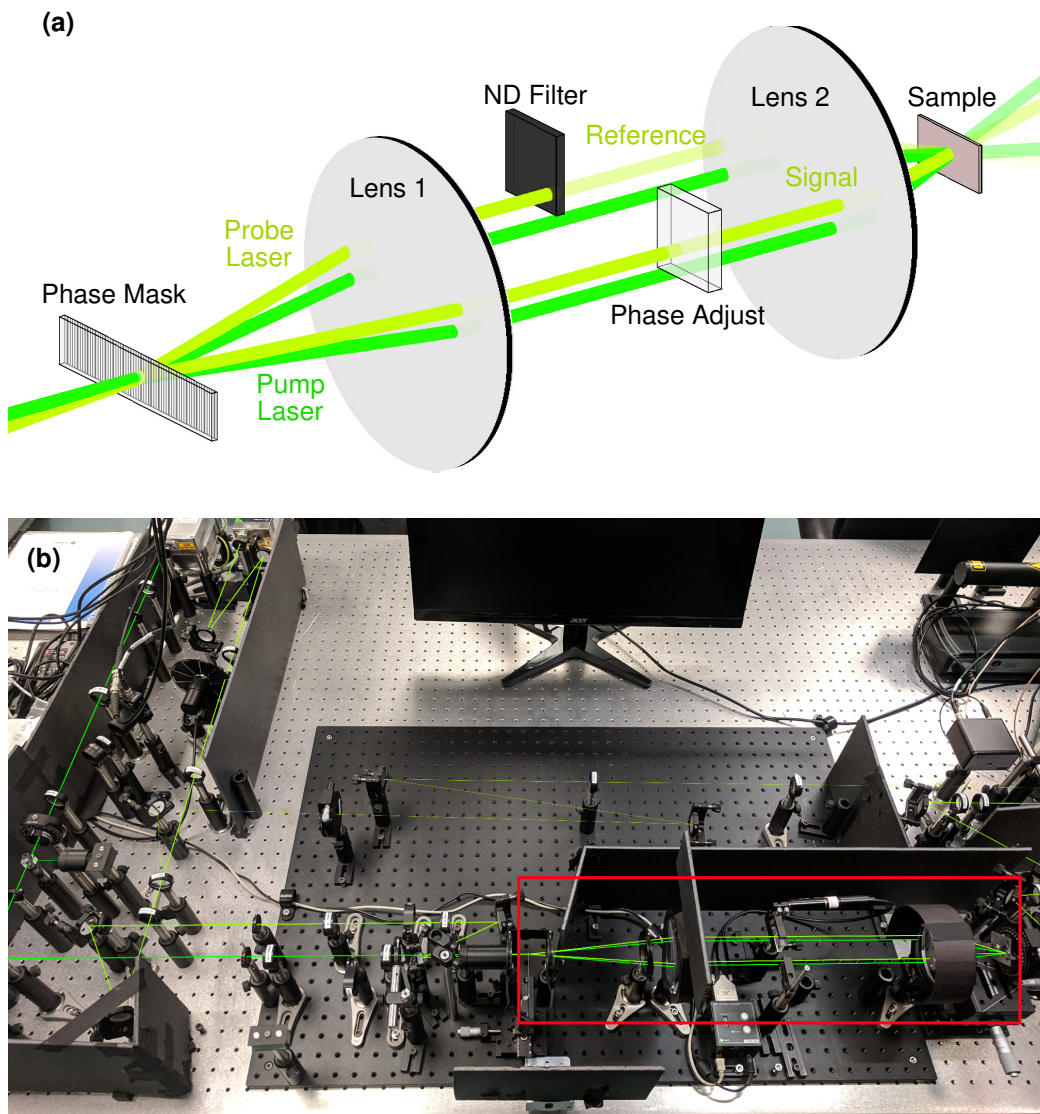
Figure 3.2: (a) Diagram of the Transient Grating (TG) optical setup. A separate pump and probe beam are each split into 2 beams at the phase mask, focused by 2 lenses, and all 4 beams are incident on the sample. (b) Picture of the TG setup as built in the Minnich Lab at Caltech. The section outlined in red corresponds to the schematic in (a).

to Bragg's Law:

$$d_{PM} \sin(\theta_1) = n\lambda \tag{3.20}$$

where we are only interested in $n = 1$. In this thesis, we use phase mask periods ranging from $d_{PM} = 2.2\,\mu m$ to $60\,\mu m$. Following along in Figure 3.2(a), the two pump beams are focused by Lens 1, which has a focal length of $f_1 = 200\,mm$, such that they are parallel. At Lens 2, with focal length $f_2 = 100\,mm$, the two beams are refocused to the lens's focal point, coincident with the sample. The phase mask is spaced a distance of f_1 from Lens 1, Lens 1 and Lens 2 are a distance of $f_1 + f_2$ apart, and the sample is a distance of f_2 from Lens 2. This configuration is known as a Keplerian telescope, which effectively ensures a magnified (or reduced) image of the phase mask on the sample. For arbitrary f_1 and f_2, the angle of the pump beams after Lens 2 can be calculated based on the geometry of the lenses:

$$\Delta x = f_1 \tan(\theta_1) = f_2 \tan(\theta_2) \tag{3.21}$$

$$\theta_2 = \arctan\left(\frac{f_1}{f_2} \tan(\theta_1)\right) \tag{3.22}$$

where Δx refers to the distance each pump beam is from the central optical axis after Lens 1. Combining our expressions relating the phase mask period (Eqn. 3.20), pump angles(Eqn. 3.22), and the grating period (Eqn. 3.6), we relate the phase mask period to the sample's grating period:

$$d = \frac{\sqrt{f_2^2 d_{PM}^2 + \lambda^2 \left(f_1^2 - f_2^2\right)}}{2f_1} \tag{3.23}$$

where we see that they have a nontrivial relationship. However, in the limit of either $f_1 = f_2$ or $\lambda^2 \ll d_{PM}^2$, which corresponds to $\theta_1 \ll 1$, the expression simplifies to:

$$d = \frac{f_2}{2f_1} d_{PM} \tag{3.24}$$

In fact in most literature on TG, and for most of the grating periods used in this work, this simplification is perfectly valid. However due to the lowest grating periods used in our work, which begin to approach the diffraction limit, the full expression is required. Using Eqn. 3.23, we find the range of theoretically accessible grating periods for our setup to be from $d = 593\,nm$ to $15\,\mu m$.

While computing the grating period is straightforward based on the lenses' focal lengths, any given lens is limited in the angle of light it can accept and focus

based on its numerical aperture (NA), which is based on the radius of the lens in addition to the focal length. Due to the large angles > 20° caused by the low, sub-µm grating periods used, lenses with NAs exceeding 0.4 were required. As a result, both lenses have a diameter of 100 mm, with the larger lens being 36 mm thick. Further, to avoid spherical aberrations, aspherical lenses were used (Thorlabs AL100100-A and AL100200-A). Lastly, such large lenses were required such that the working distance following Lens 2 left enough room for a cryostat to be used in temperature-dependent measurements. These large, unconventional lenses are necessary to enable the low grating periods used in this thesis.

Having covered the phase mask, Lens 1, and Lens 2; the only remaining optics in the highlighted red section of Figure 3.2(a) are the neutral density (ND) filter and the phase adjust, each of which are only used on the probe beams. First, the ND filter is used to modulate the reference probe beam and is the source of the term f in Eqn. 3.14. Again, this optic is used because the photodetector that is measuring the signal has an upper limit to its input power, before saturation or damage occurs. The ND filter is frequently exchanged based on how much power the sample transmits. More transparent samples may need a strong ND filter. The ND filter we used primarily (if we used on at all) was a 50 mm square reflective ND1.5 filter from Edmund Optics. Note that a reflective ND filter is used to avoid heating of the optic, which could cause unstable amplitude or phase of the reference beam. We also ensured the ND filter was rated for a sufficiently high damage threshold relative to the probe laser fluence, though this is generally not a concern if a reflective ND filter is used. Finally, we specifically used a square-shaped optic so that it could be placed in front of the reference probe beam without obscuring any of the other 3 beam paths.

The phase adjust is simply an optical flat (glass slide) that the signal beam passes through. Its sole purpose is to change the phase of the signal beam. By slightly changing the angle of this optic, the length of glass the light travels through will slightly change. As a result, the effective optical path, and thus the phase of the light, will change too. The relative phase between the signal beam and reference beam is given by ϕ, as used in Eqn. 3.14. The angle of this optic is controlled by a motor with fine control over its angle. It is this optic specifically that is critical to implementing the heterodyne detection scheme discussed in Section 3.3. We used a 6 mm thick square optical flat from OptoSigma rated to < 5 arcseconds parallelism, though we later concluded the parallelism specification is unimportant. As a result

even a basic glass slide is sufficient. Further discussion on controlling the phase is given in Section 3.8.

Lens Design to Control Beam Size

Looking again to Figure 3.2, there are many optics before the TG telescope section, most of which are lenses used to control the size of the pump and probe lasers. The size of both laser beams is very important for controlling the energy density, or fluence, at the sample. If the beams are too small and concentrated for a specific sample, it can lead to overheating or burning. Furthermore, large values of the amplitude of the thermal grating ($\Delta T > \sim 10\,\text{K}$) can lead to nonlinear values of material properties like thermal conductivity over the large temperature range. On the other hand, large beam sizes will have low energy density, resulting in a weaker signal. Large beam sizes may also be too large for very small samples.

Our TG setup was designed to have pump and probe beam diameters at the sample of $\sim 500\,\mu\text{m}$, $\sim 1\,\text{mm}$, and $\sim 2\,\text{mm}$. To design the lens optics with this goal in mind, we used the equations for Gaussian beam optics, which govern how a laser beam with an ideal Gaussian spatial profile propagates through space. To solve these equations, we have written a program in MATLAB to propagate a Gaussian beam with known starting beam size through a series of lenses. By varying the lenses used, their focal length, and their position, we developed the optical setup shown in Figure 3.3(a) and (b) for the pump and probe lasers, respectively. The true beam size was measured using a Thorlabs CCD Camera Beam Profiler. Excellent agreement was found between the theoretically calculated beam sizes and those measured for the same lens configuration.

As mentioned, the optics were designed to support 3 alternative beam sizes. This was accomplished using a set of 3 lenses on flip mounts immediately before the phase mask for both the pump and probe. By flipping specific lenses up or down, the desired beam size would be projected onto the sample.

One important consideration in designing the optics for the FlareNX pump laser is its extremely large power density. At $\sim 300\,\mu\text{J}$, delivered in $\sim 1\,\text{ns}$, a small beam size will lead to large power densities capable of burning many optical components, including mirrors. As a result, a pair of lenses are positioned immediately after the pump laser to expand the beam to a 4 mm diameter. This is large enough to remain collimated over long distances and to avoid burning any optics.
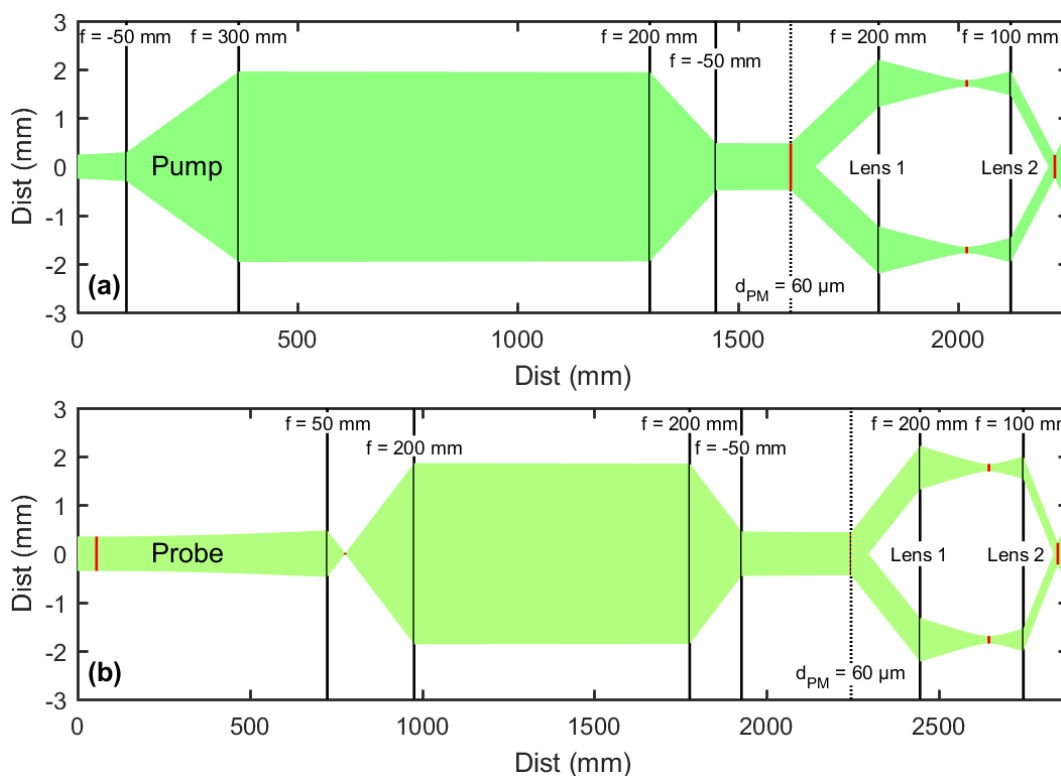
Figure 3.3: (a) Schematic of the pump laser passing through optics before reaching the sample. All solid black vertical lines correspond to lenses, labelled with their focal length. The dotted line shows the phase mask, which splits the pump into two beams, which are refocused after Lens 1 and Lens 2 to the sample. The red lines correspond to the waist of the Gaussian laser beams. (b) Same as (a), but for the probe laser.

Energy Modulation: Avoiding Sample Overheating

Another critical component of the TG design involves controlling the laser power. Especially when dealing with low thermal conductivity samples, such as most polymers, heat dissipation can occur very slowly. Even if a single laser pulse only heats the exposed sample volume by an average of 1 K above its starting temperature, or T_0, the entirety of that energy needs to dissipate before the next pulse arrives, which is only 5 ms in our setup. Otherwise the energy from multiple pulses will add up excessively. Ideally, the excited spot on the sample will reach equilibrium at some temperature moderately above T_0. As previously mentioned, the energy per pulse of the pump laser is ∼300 μJ, which is high enough to easily burn most samples, unless they absorb very little laser light or dissipate heat very effectively.

To avoid overheating by the pump laser, we use 2 optics, placed after the first pair of lenses (as can be seen in Figure 3.2). The first is a half-wave plate on a rotating

mount. The second is a polarizing beamsplitter cube. Because the light leaving the pump laser is vertically polarized, we can use a half-wave plate to change the polarization. At 0°, light passing through the half-wave plate remains vertically polarized, however at 45°, the exiting light is horizontally polarized. After this, the beamsplitter cube keeps only the light that is still vertically polarized, meaning the angle of the half-wave plate can directly control the total pump energy after the beamsplitter. The equation relating the angle and the pump energy is:

$$E = E_0 \cos^2(2\theta) \tag{3.25}$$

where P_0 is the maximum pump energy.

Overheating can also be caused by the probe laser. Because it is continuous, energy can build up over time in the sample. The probe laser's power can be easily adjusted with its controller, ranging from 30 mW to 330 mW. However, higher powers provide better signal to noise when collecting data, so it is optimal to use the highest power possible. Even 30 mW is too high for many samples. To enable high power without overheating, the probe laser is mechanically chopped soon after exiting the probe laser source. The mechanical chopper is a wheel with a narrow opening spinning at a corresponding frequency to the pump laser repetition rate and is synced with the pump laser. Because we are only interested in the signal immediately before, during, and after the pump pulse hits the sample, which usually amounts to 100 μs at most (and is typically far less), we can block the probe laser from hitting the sample the remainder of the time. The mechanical chopper completely blocks the laser in our setup for nearly 97% of the time, drastically limiting the energy delivered to the sample. These energy reduction measures are critical for measuring polymers and other low thermal conductivity materials.

Signal Detection

The last important set of optical components is dedicated to measuring the signal leaving the sample. This is accomplished using one of two photodetectors. The first detector is a Newport 1601FS-AC Photoreceiver, capable of measuring fast signals approaching ~1 ns. The second detector, a Thorlabs PDB460A DC-200 MHz Balanced Photodetector, is used for measuring slower signals, which occur at high grating periods or low thermal conductivity samples. Because it is capable of measuring DC signals, there is no distortion of long signals, which can occur with faster AC detectors. However, this results in the signal's DC term remaining, which can hurt resolution when measured by an oscilloscope. This is solved because it is

a balanced detector, which accepts a second beam into another photoreceiver and subtracts the two. We direct a small portion of the probe laser (after it is mechanically chopped) to the detector. It is also sent through a polarizer on a rotating mount, which can be used to modulate the power and thus match the DC term from the signal beam. The signal actually going to the oscilloscope thus has an average DC term near 0.

Another necessary component of the detection scheme is a bandpass filter. This is a filter that allows only a very narrow range of wavelengths through. This is necessary because the pump *power* is so great compared to the probe's power, any small portion of the light that scatters into the detector can greatly overwhelm the detector. The filter blocks this scattered light. Furthermore, because many of the polymer samples included in Chapter 4 scatter light very intensely, a second filter was also used to fully block the scattered pump laser light from entering the detector.

3.5 Sample Preparation: Sample Optical Properties

With the optical setup fully laid out, the next important consideration is the sample being measured. As discussed in Sections 3.2 and 3.3, the pump laser must excite a thermal grating, and the probe laser must diffract off of it. This requires the sample to absorb the pump laser and transmit the probe laser. Because the wavelengths of each laser are so close, the sample cannot be entirely opaque or transparent. Luckily though, in our experience the transmission can range very widely from ~2% to ~98% and still provide measurable signal. Signal-to-noise can always be improved though with longer signal averaging, which can push these bounds even further. We generally average $<1 \times 10^5$ samples, though for some samples with low optical transmission, we have gone as high as $\sim 1 \times 10^7$. Very thick samples ($>100\,\mu$m), even if almost entirely transparent, can also give some signal due to their large optical depth.

The other optical requirement in any given sample is that its index of refraction is temperature sensitive. For the real part of the index of refraction, this is referred to as the thermo-optic coefficient. In many polymers, this number is on the order of -1×10^{-4}/K and can be related to the material's thermal expansion coefficient[88]. While generally not an issue, some materials of interest may have exceptionally low (or high) coefficients, which can affect the maximum possible signal obtainable with TG.

While many materials previously measured with TG, such as Si, require no special

treatment, transparent materials, as most polymers are, require a dye of some sort to facilitate absorption. However there are several requirements on the dye being introduced. First, it must be present in trace enough quantities that it does not otherwise influence the material properties being measured. This is generally not a problem as most dyes have high enough absorption rates to only be required in small concentrations. Second, the dye must be compatible with the fabrication process. For example, a dye molecule soluble in polar solvents may be difficult to incorporate in a solution-processed polymer dissolved in a non-polar solvent. Third, the dye must be stable. Thermal degradation or photo-catalyzed degradation will lead to unstable TG measurements as a function of time. Finally, the dye must thermalize absorbed light efficiently, turning these photons into heat energy on a timescale that is fast compared to the thermal decay timescale.

As part of the development of our TG setup at Caltech, we tested numerous dyes, including polar and non-polar molecules, as well as different nanoparticles (NPs). Finding appropriate dyes that meet all stated requirements is nontrivial. For example, some dyes exhibit fluorescence or phosphorescence, where they re-radiate absorbed light at a fixed rate, sometimes over μs timescales. Not only does this reduce thermalization, but this makes the absorption coefficient of the light time-dependent after the pump pulses arrive, which adds an amplitude grating signal. For measuring phase grating signals, this contribution can be removed with heterodyning.

Another related issue with some dye materials is the presence of anomalous, fast decay processes. The optical excitation and subsequent thermal relaxation can be extremely complicated, and thus many dyes need to be tested for this. For example, we used Au NPs ($< 10 \, \text{nm}$) from Sigma-Aldrich and found non-thermal signals resulting from the pump excitation. While many of these signals can be subtracted out through careful implementation of heterodyning (example provided in Section 3.8), significantly large signals, or those that show up along side the thermal signal pose a challenge in data analysis. Any occurrences of this in data presented in this thesis will be discussed when the data is shown.

3.6 Thermal Modelling

After acquiring a signal, the data must be fit to an appropriate thermal model with a number of parameters, including one related to thermal conductivity. For this we simply use Fourier's Law:

$$J = -\kappa \nabla T \tag{3.26}$$

where J is the heat flux. Because the thermal grating is excited in a single direction, the resulting heat transfer is typically 1-dimensional, leaving us with:

$$J = -\kappa \frac{\partial T}{\partial x} \tag{3.27}$$

This may be combined with the continuity equation to yield a time-dependent equation:

$$\rho C \frac{\partial T}{\partial t} = -\nabla J \tag{3.28}$$

$$\frac{\partial T}{\partial t} = \frac{\kappa}{\rho C} \frac{\partial^2 T}{\partial x^2} = \alpha \frac{\partial^2 T}{\partial x^2} \tag{3.29}$$

where C is the heat capacity and ρ is the density, and α is the thermal diffusivity. Note, we have made a number of basic assumptions here, including that heat is not generated or lost, though this is valid as long as we make the initial thermal profile an initial condition. Many of the other assumptions will be discussed at the end of this section.

This simple partial differential equation is generally solved in introductory differential equations sources, but for completion we briefly show the solution here using a spatial Fourier transform:

$$\mathcal{F}\left[\frac{\partial T(t, x)}{\partial t}\right] = \mathcal{F}\left[\alpha \frac{\partial^2 T(t, x)}{\partial x^2}\right] \tag{3.30}$$

$$\frac{d\overline{T}(t, k_x)}{dt} = -\alpha k_x^2 \overline{T}(t, k_x) \tag{3.31}$$

$$\int_{\overline{T}(t=0)}^{\overline{T}(t,k_x)} \frac{d\overline{T}(t, k_x)}{\overline{T}(t, k_x)} = \int_0^t -\alpha k_x^2 dt \tag{3.32}$$

$$\ln\left(\frac{\overline{T}(t, k_x)}{\overline{T}(0, k_x)}\right) = -\alpha k_x^2 t \tag{3.33}$$

$$\overline{T}(t, k_x) = \overline{T}(0, k_x) e^{-\alpha k_x^2 t} \tag{3.34}$$

We then evaluate the initial condition by taking the Fourier transform of Eqn. 3.8. We can then plug the Fourier transformed expression into Eqn. 3.34 and take an inverse Fourier transform.

$$\overline{T}(0, k_x) = \Delta T 2\pi \left(\delta(k_x) + \frac{1}{2}(\delta(k_x - q_x) + \delta(k_x + q_x))\right) \tag{3.35}$$

$$\overline{T}(t, k_x) = \Delta T 2\pi \left(\delta(k_x) + \frac{1}{2}(\delta(k_x - q_x) + \delta(k_x + q_x))\right) e^{-\alpha k_x^2 t} \tag{3.36}$$

$$\mathcal{F}^{-1}\left(\overline{T}(t, k_x)\right) = T(t, x) = \Delta T \left(1 + e^{-\alpha q_x^2 t} \cos(q_x x)\right) \tag{3.37}$$

where ΔT gives the initial amplitude of the thermal grating. Because the probe selectively measures the amplitude of the grating, it is clear that the signal decay corresponds to the decaying exponential:

$$I(t) \propto e^{-\alpha q_x^2 t} = e^{-\frac{t}{\tau}} \tag{3.38}$$

where $\tau = \frac{1}{\alpha q_x^2}$. This simple equation embodies one of the great advantages of TG. The data analysis is usually much more straightforward than other techniques such as TDTR.

Another important feature to highlight about this solution is the dependence of τ on the grating wavevector, q_x. As a result of this relationship, data may be taken repeatedly at different grating periods, which will cover a wide range of timescales, changing as q_x^2. This can give further confidence of the true value of α. Figure 3.4 shows both an example of a TG signal taken for a PDMS film, as well as the decay rate as a function grating wavevector. The slope of this latter plot gives the thermal diffusivity, α, which was found to be in excellent agreement with literature values.

While Eqn. 3.37 is valid for most all of the data discussed in this thesis, as well as most of the published literature on TG[4], there are a number of assumptions that are important to consider to avoid oversimplifying in special cases. One such assumption calls back to Section 3.2, where we ignored the finite beam size when describing the thermal grating excited into the sample. To make this assumption, we must satisfy $d \ll \sigma_{x/y}$. Essentially, this just means that the grating period must be small compared to the beam size such that the gradients involved are dominated by the grating. Similarly, the thermal decay associated with the diffusion of the heated spot must be slow compared to the decay of the grating. In this work, a minimum beam size of $500\,\mu m$ ($\sigma_x = 125\,\mu m$) is used, with the largest grating period being $15.7\,\mu m$, which is small enough, relatively. A more formal derivation incorporating finite beam size is included in the next section.

Another more important assumption we have made is that of purely 1-dimension heat transfer. This assumption is primarily broken when dealing with thin films. Previously, we assumed a free-standing film, such that the film boundaries were adiabatic. However, the case of a thin film is sometimes unavoidable due to fabrication constraints. This is true especially for many polymer films. To deal with this case,

---

[4]Specifically, this refers to TG run in the transmission geometry.
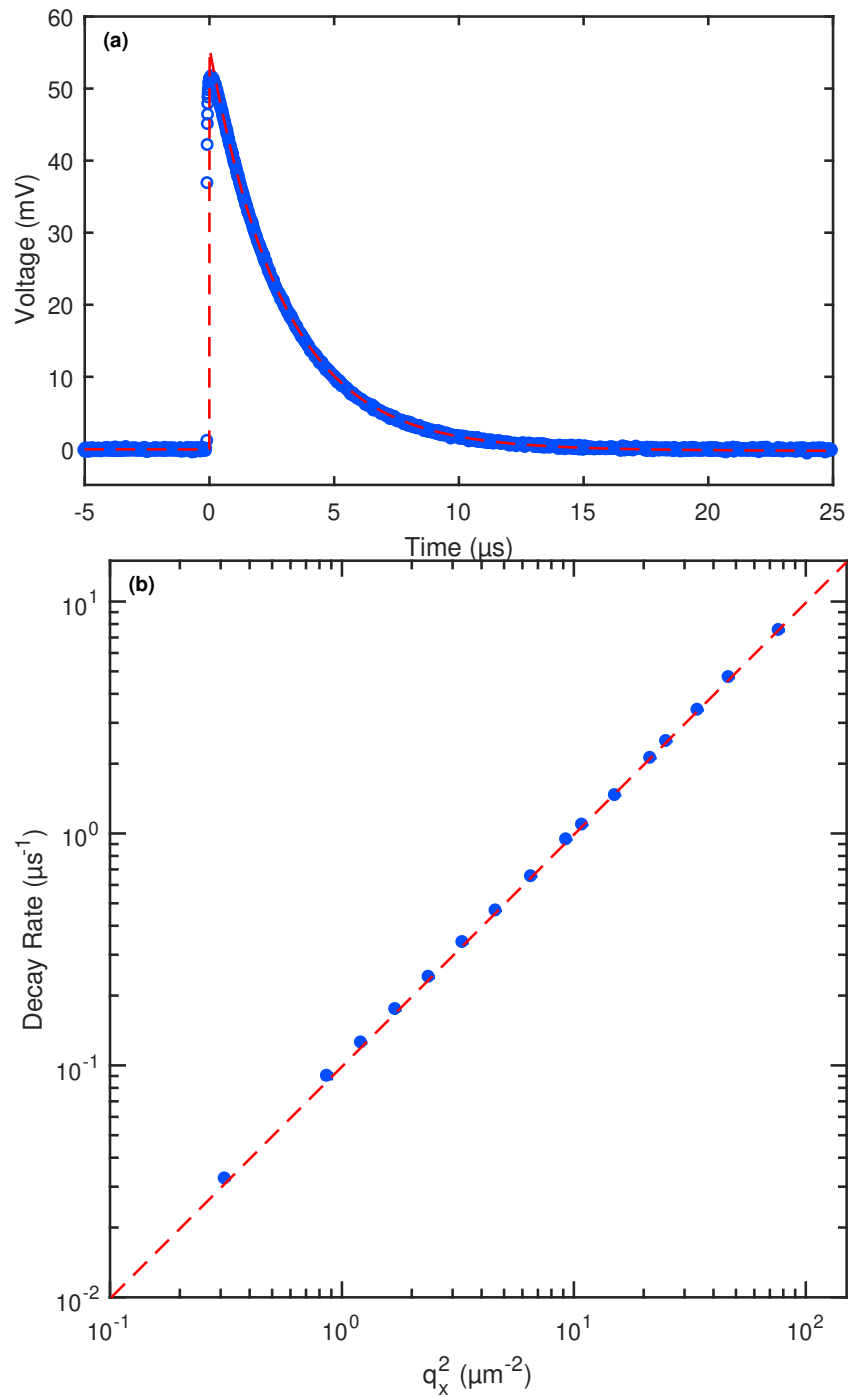
Figure 3.4: (a) Example TG signal for a PDMS signal using a grating period of 3.24 μm. A simple exponential fitting is shown in red. (b) Exponential decay rate as a function of grating wavevector for the same PDMS film as in (a). The slope of this line gives the thermal diffusivity, which is 0.1 mm/s

we use the next section to go through a full derivation solving the time-dependent temperature in the thin film geometry.

3.7 Thin Film Solution

While TG is most easily applied to free-standing films or membranes, there are a variety of interesting materials that are fabricated as thin films on substrates. Many polymers for example are fabricated via solution-processing onto substrates. Furthermore, if there is a very thin film to be studied, there may be no way to study its thermal transport properties without supporting it with a substrate. Regardless, this type of sample results in the possibility of heat leakage from the film into the substrate. Considering the limit of a very thin film and a very conductive substrate, it is clear how this sort of heat leakage could decrease the thermal decay time that is observed compared to the case without a substrate. As a result, we derive the full thermal solution for this sample geometry with the TG experiment.

First, we define the system geometry and boundary conditions governing the physical problem. We have two layers. Layer 1 is a thin film with thickness, L, and layer 2 is a semi-infinite substrate. The film and substrate are infinite in the x and y directions. We assume the film absorbs light according to an absorption coefficient, δ, while the substrate is either fully transparent or has a much smaller relative absorption compared to the film such that it can be ignored, as is the case with substrates such as glass or sapphire. We also make no assumptions about the anisotropy of the film or substrate, so material properties like thermal conductivity can be anisotropic. As for the boundary conditions, we assume the top interface of layer 1 is adiabatic. The heat flux at the interface between layers 1 and 2 is computed based on the interface conductance, G. Finally, in layer 2, the temperature when far from the interface is given by $T(z \rightarrow \infty) = T_0$.

Differential Equation for Thermal Transport

We begin with Fourier's law and the continuity equation as we did in the previous section. However we now leave the full thermal conductivity tensor and work in all three spatial dimensions. Additionally, we retain the heat generation term in the

continuity equation.

$$\rho C \frac{\partial T}{\partial t} = -\nabla J + Q \tag{3.39}$$

$$\rho C \frac{\partial T}{\partial t} = -\nabla \left[-\kappa_x \frac{\partial T}{\partial x} - \kappa_y \frac{\partial T}{\partial y} - \kappa_z \frac{\partial T}{\partial z} \right] + Q \tag{3.40}$$

$$\frac{\partial T}{\partial t} = \alpha_x \frac{\partial^2 T}{\partial x^2} + \alpha_y \frac{\partial^2 T}{\partial y^2} + \alpha_z \frac{\partial^2 T}{\partial z^2} + \frac{Q}{\rho C} \tag{3.41}$$

where κ_i is the thermal conductivity in the direction $i = (x, y, z)$, α_i is the thermal diffusivity component in the i-direction, ρ is the density, C is the heat capacity by mass, and Q is the volumetric heat generation term[5]. This partial differential equation (PDE) must be solved separately for each layer.

Before we begin to solve the PDE, we Fourier transform (FT) it in time as well as the x and y directions.

$$i\omega \overline{T} = \alpha_x \left(-k_x^2 \right) \overline{T} + \alpha_y \left(-k_y^2 \right) \overline{T} + \alpha_z \frac{\partial^2 \overline{T}}{\partial z^2} + \frac{\overline{Q}}{\rho C} \tag{3.42}$$

$$\frac{i\omega + \alpha_x k_x^2 + \alpha_y k_y^2}{\alpha_z} \overline{T} = \frac{\partial^2 \overline{T}}{\partial z^2} + \frac{\overline{Q}}{\kappa_z} \tag{3.43}$$

$$u^2 \overline{T} = \frac{\partial^2 \overline{T}}{\partial z^2} + \frac{\overline{Q}}{\kappa_z} \tag{3.44}$$

Here we have grouped terms of $\overline{T}$ to yield an inhomogeneous ordinary differential equation (ODE). We then defined a variable u to contain the temporal and spatial frequency terms. We have also applied the definition that $\kappa_z = \rho C \alpha_z$. Note also that we omit the functional dependencies for T, Q, and their FT pairs for readability, but they are all dependent on x, y, z, and t or the appropriate FT pair variable. At times we may denote specific variable dependencies when relevant, but the others are implicit.

General Solutions

We may now consider solutions for this ODE. The solutions to the homogeneous ODE are well known to be exponentials. For the inhomogeneous solution, we use our knowledge of the functional form of $\overline{Q}$ in terms of z:

$$Q(x, y, z, t) = Q_0(x, y, t) e^{-\frac{z}{\delta}} \tag{3.45}$$

Because heat is generated by the absorption of the pump laser, we know the absorption's dependence on z must follow an exponential decay. The functional form for the other variables is not yet necessary.

---

[5]Q has units of W/m^3.

We can now write the form of the general solution to Eqn. 3.44:

$$\overline{T}(z) = Ae^{uz} + Be^{-uz} + De^{-\frac{z}{\delta}} \tag{3.46}$$

where A, B, and D are functions that may depend on any variable except z and will be solved for using the boundary conditions.

With the general solution established, we now consider that we will need to solve for the unknown constants separately for both layers:

$$\overline{T}_1(z) = A_1 e^{u_1 z} + B_1 e^{-u_1 z} + De^{-\frac{z}{\delta}} \tag{3.47}$$

$$\overline{T}_2(z) = A_2 e^{u_2 z} + B_2 e^{-u_2 z} \tag{3.48}$$

Here we have explicitly written the solution to each layer, denoting their unique variables by subscript. Also note that because there is no heat generation in layer 2 (or it is small enough to ignore), we do not need the inhomogeneous term and only need to solve for A_2 and B_2.

Inhomogeneous Solution

Before we solve for the homogeneous portion of the ODE (corresponding to A_i and B_i), we solve for D. To do this, we plug in Eqn. 3.47 and Eqn. 3.45 into our inhomogeneous ODE, Eqn. 3.44.

$$u_1^2 \left(A_1 e^{u_1 z} + B_1 e^{-u_1 z} + De^{-\frac{z}{\delta}} \right) = \left(A_1 u_1^2 e^{u_1 z} + B_1 u_1^2 e^{-u_1 z} + \frac{D}{\delta^2} e^{-\frac{z}{\delta}} \right) + \frac{\overline{Q}_0 e^{-\frac{z}{\delta}}}{\kappa_{1,z}}$$

$$\tag{3.49}$$

$$Du_1^2 e^{-\frac{z}{\delta}} = \frac{D}{\delta^2} e^{-\frac{z}{\delta}} + \frac{\overline{Q}_0 e^{-\frac{z}{\delta}}}{\kappa_{1,z}} \tag{3.50}$$

$$D = \frac{\overline{Q}_0 \delta^2}{\left(u_1^2 \delta^2 - 1 \right) \kappa_{1,z}} \tag{3.51}$$

where the homogeneous solution has been cancelled out, leaving only terms linear in $e^{-\frac{z}{\delta}}$, which can be cancelled out. We then solved for D.

Boundary Conditions

Next, we need to solve for A_i and B_i in each layer. These four unknowns require four equations. Two of these equations come from the boundary conditions we

previously described. The first is the adiabatic condition at the top of layer 1.

$$J_{1,z}(0) = -\kappa_{1,z} \left.\frac{\partial \overline{T}_1(z)}{\partial z}\right|_{z=0} = 0 \tag{3.52}$$

$$-\kappa_{1,z}\left(A_1 u_1 - B_1 u_1 - \frac{D}{\delta}\right) = 0 \tag{3.53}$$

$$A_1 u_1 - B_1 u_1 - \frac{D}{\delta} = 0 \tag{3.54}$$

The second boundary condition is for the temperature of layer 2 to reach the ambient surrounding temperature, T_0, as $z \to \infty$. But because there is no difference in our choice of T_0, we use 0 as our baseline temperature. Because all the equations are linear in temperature, a simple offset for any finite T_0 can be added to the final solution.

$$\left.\overline{T}_2(z)\right|_{z\to\infty} = 0 \tag{3.55}$$

$$A_2 e^{u_2 \infty} + B_2 e^{-u_2 \infty} = 0 \tag{3.56}$$

To evaluate this equation, we recall the definition of u_i which can be taken from Eqn. 3.43. From here, we see the real part of u_i^2 is always positive. By consistently selecting the positive real branch cut of the square root (when obtaining u_i), we can say that $Re[u_i] \geq 0$.

$$A_2(\infty) + B_2(0) = 0 \tag{3.57}$$

$$A_2 = 0 \tag{3.58}$$

Eqn. 3.57 will tend to ∞ unless $A_2 = 0$, which gives us our second boundary condition equation.

The final two equations we need to solve for our remaining constants comes from the interface between the two layers. First, the heat flux must be continuous at the interface:

$$J_{1,z}(L) = J_{2,z}(0) \tag{3.59}$$

$$-\kappa_{1,z} \left.\frac{\partial \overline{T}_1(z)}{\partial z}\right|_{z=L} = -\kappa_{2,z} \left.\frac{\partial \overline{T}_2(z)}{\partial z}\right|_{z=0} \tag{3.60}$$

$$-\kappa_{1,z}\left(A_1 u_1 e^{u_1 L} - B_1 u_1 e^{-u_1 L} - \frac{D}{\delta}e^{-\frac{L}{\delta}}\right) = -\kappa_{2,z}(-B_2 u_2) \tag{3.61}$$

where we have already plugged in for $A_2 = 0$.

Second, the heat flux is proportional to the temperature difference and the interface conductance, G.

$$J_{2,z}(0) = G\left(\overline{T}_1(L) - \overline{T}_2(0)\right) \tag{3.62}$$

$$\kappa_{2,z}B_2u_2 = G\left(A_1e^{u_1L} + B_1e^{-u_1L} + De^{-\frac{L}{\delta}} - B_2\right) \tag{3.63}$$

Combining Eqns 3.54, 3.61, and 3.63, we can solve the system of equations for A_1, B_1, and B_2, and then plug the values into the full expressions for $\overline{T}_1$ and $\overline{T}_2$. The system of equations was solved and simplified using Mathematica, giving these final solutions:

$$
\begin{aligned}
\overline{T}_1(z) = &\left(\frac{\overline{Q}_0\delta}{\left(u_1^2\delta^2 - 1\right)\kappa_{1,z}}\right)\Bigg[u_1e^{-\frac{L}{\delta}}\left(G\kappa_{1,z} + u_2\kappa_{2,z}(\kappa_{1,z} - G\delta)\right)\cosh(u_1z) \\
&+ u_1\delta e^{-\frac{z}{\delta}}\left(Gu_2\kappa_{2,z}\cosh(Lu_1) + u_1\kappa_{1,z}(G + u_2\kappa_{2,z})\sinh(Lu_1)\right) \\
&- u_1\kappa_{1,z}(G + u_2\kappa_{2,z})\cosh(u_1(L - z)) - Gu_2\kappa_{2,z}\sinh(u_1(L - z))\Bigg] \\
&\Bigg/ \left(u_1\left(Gu_2\kappa_{2,z}\cosh(Lu_1) + u_1\kappa_{1,z}(G + u_2\kappa_{2,z})\sinh(Lu_1)\right)\right)
\end{aligned}
\tag{3.64}
$$

$$
\begin{aligned}
\overline{T}_2(z) = &\left(\frac{\overline{Q}_0\delta}{\left(u_1^2\delta^2 - 1\right)\kappa_{1,z}}\right) \\
&\times\left(G\kappa_{1,z}e^{-u_2z}\left(e^{-\frac{L}{\delta}}\cosh(Lu_1) + u_1\delta e^{-\frac{L}{\delta}}\sinh(Lu_1) - 1\right)\right) \\
&\Bigg/ \left(Gu_2\kappa_{2,z}\cosh(Lu_1) + u_1\kappa_{1,z}(G + u_2\kappa_{2,z})\sinh(Lu_1)\right)
\end{aligned}
\tag{3.65}
$$

where we have also plugged in for the coefficient D from Eqn. 3.51. While the expressions for $\overline{T}_i$ are complicated, one important feature we can note is that both solutions are linear in the heat generation term $\overline{Q}_0$, which will be important.

Time-Domain Temperature Profile

While we have completed the derivation of the temperature profile in the Fourier domain (in x, y, and t), what we really need is a solution in the time domain. While the FT in time was extremely useful for solving the original PDE, one look at our solution shows that an analytical inverse Fourier transform (IFT) appears impossible to find. However, not only is a numerical IFT easier to compute, but it is the correct way to apply the IFT. To find out why, we consider the heat generation term, $\overline{Q}_0$, from Eqn. 3.64.

$\overline{Q}_0$ contains all the information about the time and spatial profile (x and y) of the pump laser, which can be written as:

$$\overline{Q}_0(k_x, k_y, \omega) = \overline{R}(k_x, k_y)\overline{F}(\omega) \tag{3.66}$$

where $\overline{R}$ corresponds to the FT of the beam's spatial profile, and $\overline{F}$ corresponds to the FT of the temporal profile. For now, we consider the temporal profile of the pump pulse. The pump laser can be considered a periodic series of short Gaussian pulses with a fixed repetition rate:

$$F = \sum_{n}^{\infty} G_t(t - nt_r) \tag{3.67}$$

$$\tag{3.68}$$

where $G_t(t)$ corresponds to a Gaussian profile with standard deviation σ_t and t_r is the pulse repetition period. To FT this to get $\overline{F}$, we first rewrite F:

$$F = G_t(t) \circledast \sum_{n=-\infty}^{\infty} \delta(t - nt_r) \tag{3.69}$$

where we have expressed F as the convolution of a Gaussian profile with a series of δ functions (a Dirac comb). Taking the FT of a convolution of two terms is equivalent to multiplying the FT of each individual term:

$$\overline{F} = \mathcal{F}\left[g(t) \right] \times \mathcal{F}\left[\sum_{n=-\infty}^{\infty} \delta(t - nt_r) \right] \tag{3.70}$$

$$\overline{F} = \overline{G}_\omega(\omega)(2\pi) \sum_{n=-\infty}^{\infty} \delta(\omega - n\omega_r) \tag{3.71}$$

where we again have a Gaussian profile (with standard deviation $\frac{1}{\sigma_t}$), multiplied by a Dirac comb in frequency space repeating every $\omega_r = \frac{2\pi}{t_r}$, which is the repetition rate in radians.

We now rewrite $\overline{T}_1$ (Eqn. 3.64), plugging in Eqns. 3.66 and 3.71:

$$\overline{T}_1(\omega, k_x, k_y, z) = \left((2\pi) \sum_{n=-\infty}^{\infty} \delta(\omega - n\omega_r) \right) \overline{G}_\omega(\omega) \overline{H}(\omega, k_x, k_y, z) \tag{3.72}$$

where $\overline{H}$ contains the entirety of the solution except for the terms from $\overline{F}$, related to the pump pulse time (or frequency) profile. Note we have given the explicit functional dependencies here again for clarity, but we will resume showing only variable dependencies as they are relevant.

We next carry out an explicit IFT of $\overline{T}_1$:[6]

$$\mathcal{F}^{-1}\left(\overline{T}_1(\omega)\right) = \frac{1}{2\pi} \int_{-\infty}^{\infty} \left((2\pi) \sum_{n=-\infty}^{\infty} \delta(\omega - n\omega_r)\right) \overline{G}_\omega(\omega)\overline{H}(\omega)e^{i\omega t}\,d\omega \tag{3.73}$$

$$T_1(t) = \sum_{n=-\infty}^{\infty} \left(\int_{-\infty}^{\infty} \delta(\omega - n\omega_r)\overline{G}_\omega(\omega)\overline{H}(\omega)e^{i\omega t}\,d\omega\right) \tag{3.74}$$

$$T_1(t) = \sum_{n=-\infty}^{\infty} \left(\overline{G}_\omega(n\omega_r)\overline{H}(n\omega_r)e^{in\omega_r t}\right) \tag{3.75}$$

Here we can see that T_1 can be computed by what is essentially a discrete IFT. However unlike discrete FTs which are used to numerically approximate what would ideally be an analytical expression, we find that a discrete IFT gives the exact solution, though we still need to carry out an infinite sum. However, making special note of $\overline{G}(\omega)$, we recall that it is a Gaussian function, meaning it decays rapidly to 0 after evaluating at a value of ω that is large compared to the standard deviation.

Spatial-Domain Temperature Profile

While we derived the exact IFT in the time/frequency domain, we have not yet discussed the IFT in the x and y directions. It was clear that we needed to IFT in time because our signal is measured in the time-domain, meaning the model used to fit it must also be in the time-domain. However it is not so clear for the spatial variables. We can understand this by considering the probe detection mechanism again, from Section 3.3.

During heterodyne detection, what is specifically being measured is the diffraction efficiency off of the thermal grating. This efficiency is proportional to the magnitude of the thermal grating, which has wavevector q_x. Because diffraction is mathematically equivalent to a spatial FT, we may evaluate the amplitude of the thermal grating simply by evaluating $\overline{T}_1(k_x)$ at $k_x = \pm q_x$. Similarly, the diffraction is only in the x direction, meaning we also only need to evaluate in the y direction at $k_y = 0$.

We thus need to define $\overline{R}$, which is the last term required to fully define $\overline{T}_1$. We first write down the expression for, R, or the real-space profile:

$$R(x, y) = G_{xy}(x, y)(1 + \cos(q_x x)) \tag{3.76}$$

where $G_{xy}(x, y)$ represents the beam shape of the pump pulses defined as Gaussian profiles with standard deviations of σ_x and σ_y. Note, this spatial profile is only valid

---

[6]Note: this is only an IFT in time, meaning T_1 is still a function of k_x and k_y.

where the pump beams are overlapping, around $z = 0$. This assumption is only invalid if pump beam angles are extremely large, and even still only if the beam size is comparable to the film thickness. In our case, the minimum pump beam sizes are $\sim 500 \, \mu m$, with sample thicknesses on the order of μm's, and beam angles always less than $\sim 25°$, meaning our expression for R is accurate.

We next consider the FT, $\overline{R}$. Because R is the product of 2 terms, the FT is the convolution of the individual terms:

$$\overline{R}(k_x, k_y) = \overline{G}_{k_x, k_y}(k_x, k_y) \circledast \left(2\pi\delta(k_x) + \pi\delta(k_x - q_x) + \pi\delta(k_x + q_x) \right) \qquad (3.77)$$

$$\overline{R}(k_x, k_y) = 2\pi\overline{G}_{k_x, k_y}(k_x, k_y) + \pi\overline{G}_{k_x, k_y}(k_x - q_x, k_y) + \pi\overline{G}_{k_x, k_y}(k_x + q_x, k_y) \quad (3.78)$$

where we have evaluated the convolution to find that $\overline{R}$ is given by 3 Gaussian profiles centered at $k_x = 0, \pm q_x$. As mentioned earlier, when evaluating the diffraction efficiency, we will only select from the second 2 terms, which correspond to the cosine term (representing the thermal grating).

One other important note worth mentioning is that the absolute measured diffraction intensity is also a function of the spatial profile of both the pump and probe, as well as the local intensity of the grating as it varies across the beam area. However, in general, the calculation incorporating these terms will simply come out to be a constant, meaning the time-dependence of the thermal grating is not affected. As we will be fitting the measured signal to a multiplicative factor of our thermal model, any constant terms are unimportant.

Model Evaluation

For completeness, we print the full temperature solution for the thin film, combining Eqns. 3.64, 3.75, and 3.78:

$$
\begin{aligned}
T_1(t, k_x, k_y, z) = \sum_{n=-\infty}^{\infty} \Bigg[& \overline{G}_\omega(n\omega_r) e^{in\omega_r t} \\
\times \Bigg(& 2\pi \overline{G}_{k_x, k_y}(k_x, k_y) + \pi \overline{G}_{k_x, k_y}(k_x - q_x, k_y) + \pi \overline{G}_{k_x, k_y}(k_x + q_x, k_y) \Bigg) \\
\times \Bigg(& \frac{\delta}{\left(u_1^2 \delta^2 - 1\right)\kappa_{1,z}} \Bigg[u_1 e^{-\frac{L}{\delta}} \Big(G\kappa_{1,z} + u_2 \kappa_{2,z}(\kappa_{1,z} - G\delta) \Big) \cosh(u_1 z) \\
& + u_1 \delta e^{-\frac{z}{\delta}} \Big(G u_2 \kappa_{2,z} \cosh(Lu_1) + u_1 \kappa_{1,z}(G + u_2 \kappa_{2,z}) \sinh(Lu_1) \Big) \\
& - u_1 \kappa_{1,z}(G + u_2 \kappa_{2,z}) \cosh(u_1(L - z)) - G u_2 \kappa_{2,z} \sinh(u_1(L - z)) \Bigg] \\
& \Big/ \Big(u_1 \Big(G u_2 \kappa_{2,z} \cosh(Lu_1) + u_1 \kappa_{1,z}(G + u_2 \kappa_{2,z}) \sinh(Lu_1) \Big) \Big) \Bigg) \Bigg]
\end{aligned}
\tag{3.79}
$$

Plugging in $k_x = q_x$ and $k_y = 0$ yields the time-dependent temperature profile, up to a linear constant, for a grating period with wavevector q_x. For evaluating z, the expression may be integrated from its final form, which is not difficult given the exponential dependencies on z, though yields an even messier final expression and so is omitted here.

We next briefly discuss a few important aspects of practically evaluating this equation for the purpose of fitting a real signal. The bulk of the expression may be evaluated analytically, however a summation over values of ω must occur, as previously mentioned. While the interval $\Delta\omega = \omega_r$ is established by the pump repetition rate, this value can typically be artificially enlarged to reduce the number of terms that need to be added together. For example, if a particular thermal signal decays to near 0 within 1 μs, yet the pump repetition rate is 1 ms, there is no benefit to computing 1000 times more points in time than are necessary. As a result, for the purposes of computing the thermal grating decay, the repetition period/rate can be shortened from the true value to minimize computational cost, while calculating the decay signal for long enough to allow the signal to decay fully.

Similarly, we established that the sum only needs to be carried out until $\overline{G}(\omega)$ has gone to 0. Corresponding to the FT of the pump time profile, the shorter the pulse, the higher the frequencies will need to be incorporated. However, if the thermal decay being studied is relatively slow, and thus not requiring high frequency components,

an artificially longer pump pulse width can be used in the calculations to shorten the number of frequencies that need to be calculated. This will have no meaningful effect on the final profile. In summary, we have established that numerically, the $\Delta\omega$ and the ω_{upper} can be adjusted to minimize summation terms without having a significant change on the final evaluation.

Another important shortcut we can take results from T_1 being real. When T_1 is real, it holds that $Re[\overline{T}_1]$ is an even function and $Im[\overline{T}_1]$ is an odd function. As a result, the summation over values of ω need only be computed for $\omega > 0$. This can also be understood by realizing that the imaginary contributions must cancel because the final result must be real. Second, ω only appears squared (in the equations of Gaussian functions) or within the term u. For convenience, the definition of u_i is reprinted here:

$$u_i = \sqrt{\frac{i\omega + \alpha_{i,x}k_x^2 + \alpha_{i,y}k_y^2}{\alpha_{i,z}}}$$

In this term, ω always appears as $i\omega$, making it imaginary. As a result, the summation of values for $\omega < 0$ must be equal to the complex conjugate of the summation of values for $\omega > 0$. Thus, their real parts must be identical and their imaginary parts negative. This shortcut reduces computation time by a factor of 2.

The last consideration we discuss concerns $\omega = 0$. This value corresponds to the DC offset term of the final solution. As a result, this term is irrelevant for evaluating the thermal decay. However it still contains useful information about steady heating, as will be discussed next.

Evaluating Steady Temperature Rise

It is frequently important to estimate the amount of steady temperature rise that may occur on a sample to avoid burning the sample. It is clearly beneficial to increase the pump and probe powers to maximize the detected signal. However, too much power will destroy the sample or lead to distorted results, especially if it has relatively low thermal conductivity and is more susceptible to overheating (like many polymers). The $\overline{T}(\omega = 0)$ actually contains all the information about the total temperature rise on the sample.

When evaluating the $\omega = 0$ term, we now need to conduct the IFT in x and y because we are now interested in the maximum temperature on the sample, which will correspond to $x = y = 0$. As a result, we need the solution in terms of x and y, not k_x and k_y. This also makes sense because the steady temperature arises based on

the beam sizes. For the same total energy, a much larger beam size will have much smaller absolute temperature increases. The IFT can be computed numerically in k_x and k_y. Note with $\omega = 0$, the entire expression is real. Furthermore, because k_x and k_y only ever appear in the expression squared, only one quadrant needs to be evaluated.

This procedure can be very useful at iterating experimental settings to maximize the signal magnitude while remaining at optimal operating conditions on the sample.

Examples of Thin Film Measurements

To illustrate the utility of this thin film solution, we consider a thin PMMA film deposited on a (transparent) sapphire substrate. We fabricated this film by dissolving PMMA (with a molecular weight of ~120 000) in ethyl acetate and mixing it with a dye, Malachite Green, dissolved in ethanol. The solution was then deposited on to a clean sapphire substrate and placed in a drying plate surrounded by a 50/50 mixture of ethyl acetate/ethanol to slow the solvent evaporation. Further, the sample was covered with a funnel to further slow the drying process. The sample was given a day to dry, resulting in an optically smooth film. The sample was estimated to be 3 μm thick based on the volume and concentration of PMMA solution deposited, though this is subject to significant uncertainty.

The sample was measured with TG at a large grating period of 15.7 μm. At this large grating period, which is notably larger than the approximate thickness of the film, significant heat leakage can be expected into the substrate. Furthermore, the sapphire substrate that was purposely selected for this experiment has relatively high thermal conductivity ($23 \, \mathrm{Wm^{-1}K^{-1}}$), which allows it to pull heat away from the film very efficiently, which has a thermal conductivity 2 full orders of magnitude smaller. In reality, to minimize the importance of heat leakage from the film, a substrate like glass and a small grating period would be selected.

Figure 3.5 shows the TG signal for the PMMA thin film along with two thermal models. The simple exponential model (in black) uses the decay time calculated from the known thermal conductivity of PMMA, $\kappa = 0.21 \, \mathrm{Wm^{-1}K^{-1}}$, and is not a fitting parameter. Clearly, the decay is accelerated significantly due to the substrate, resulting in poor agreement. The full thin film thermal model (shown in red), corresponding to the solution derived above, again uses the known thermal conductivity (and diffusivity) of PMMA. Furthermore, all the known material constants for PMMA and sapphire are directly plugged in, rather than fitting them. An estimated
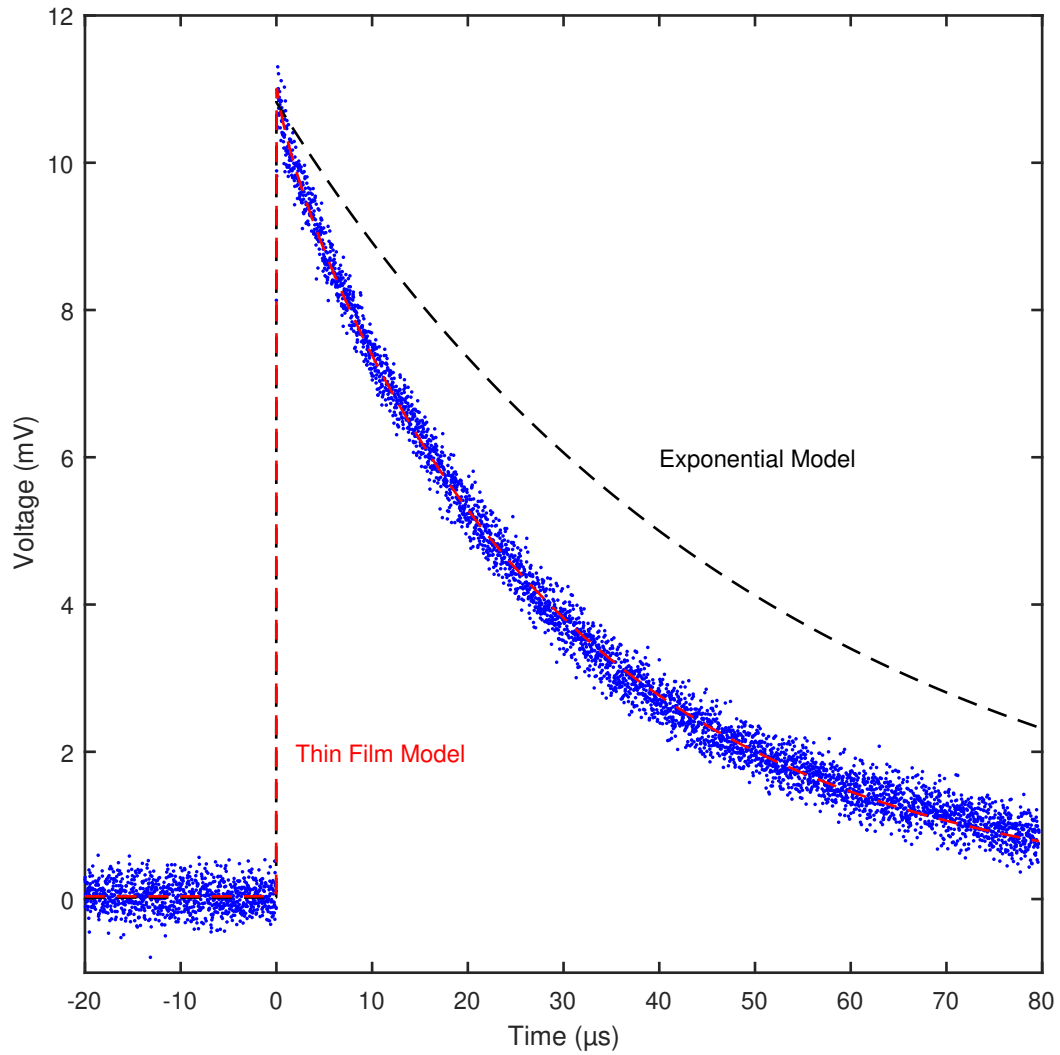
Figure 3.5: TG data for a thin film of PMMA on sapphire, along with the exponential fitting and the full thin film solution, using the known material properties of the film and substrate. The full solution is clearly necessary to account for heat leakage into the substrate during the thermal decay.

thermal conductance of $50\,\text{MW}/(\text{m}^2\,\text{K})$ is used in the model[7]. However the final fit does not appear sensitive to this value. The thickness is allowed to vary to optimize the fit and is found to be $4.7\,\mu\text{m}$, which is on the same order as the estimated value from fabrication. Of course, when applying this technique in the future, the film thickness can be measured by a variety of techniques to avoid using it as a fitting parameter. Finally, the absorption coefficient is estimated based on the thickness and measured light transmission through the film.

As can be seen from Figure 3.5, the full thin film solution very closely matches the measured data. When applying this fitting technique in the future to unknown materials, one must be aware of the many unknown parameters and how their sensitivity affects the fitting. While separate measurements on quantities like thickness and absorption coefficient can reduce the number of unknowns, the thermal diffusivity of the film and the interface conductance will both be unknown. Anisotropic materials will have an extra unknown corresponding to the cross plane diffusivity as well. However, one way to overcome having multiple unknowns is to repeat the TG measurement over a wide range of grating periods, stretching over almost 2 orders of magnitude, as is possible in our setup. This will dramatically vary the sensitivity of different parameters like thickness and interface conductance, which become less important at low grating periods. This group of measurements will allow for increased sensitivity to in-plane thermal transport.

3.8   Transient Grating Acquisition and Analysis

Having explained the optical and thermal processes behind TG, we now describe various practical techniques related to collecting and analyzing data, as well as optimizing for maximal signal.

Grating Size Calibration

Because the thermal conductivity is related to the thermal decay time by the grating period, it is important to have accurate values for the grating periods in each experiment. This can be accomplished by calibrating to a standard reference material or by direct imaging. Previous works have used water (with food dye) as a standard reference[89]. TG can also excite acoustic waves in a material due to rapid thermal expansion, allowing the user to measure the speed of sound. This is well known for water and thus makes a good reference.

---

[7]A moderately low value was chosen due to the interface being defined primarily by van der Waals interactions rather than covalent bonds.

For this thesis, all grating periods were calibrated via direct imaging. This was performed with a thin film of a doped organic molecule, spiro-OMeTAD, received from the Chabinyc group at UCSB. Due to the film's very high absorption, high pump energies were enough to leave a permanent burn mark on the material. This can occur with many materials, assuming the pump energy used is large enough. Each grating period used in this thesis was burned into a unique spot on this material, and then imaged in an optical microscope. Examples of a burned in pattern at two grating periods are shown in Figure 3.6.

To precisely quantify the burned-in grating period, a 2-dimensional Fourier Transform was taken of the image, yielding a pattern like the one shown in Figure 3.7. The center of the Fourier Transform is blocked out to avoid washing out the signal from the burned-in grating. The first order peak, corresponding to the grating wavevector, is fit to a 2-dimensional Gaussian profile to very precisely fit where the peak is. The location of this peak is used to calculate the true grating period.

The experimentally measured grating periods were in good agreement with computed values for most grating periods, however very low grating periods were lower than computed, and very high grating periods were slightly larger than computed. The former may result from aberrations near the edge of the lenses, and both may result from imprecise placement of the lenses. Regardless, the experimentally verified values are applied to all calculations and results presented in this thesis.

Phase Calibration

As described at length in Section 3.3, heterodyne detection is extremely important for amplifying and isolating the thermal signal. This is useful especially when other signals are present that can be subtracted out with this method. One challenge in practically implementing this method involves both knowing what the relative phase of the probe signal and reference beams is, as well as controlling this.

First, to control the relative phase, ϕ, we change the angle of the optical flat which acts as our phase adjust optic. To precisely control this angle, and allow us to repeatably measure and return to a particular position of the optic, we mount the glass on a mount that starts near vertical, but that can pivot at the base to be bent at an angle. Then, a motorized actuator is attached at the top where it can adjustably displace the top of the mount to control the angle of the glass. The exact displacement is measured to sub-μm resolution and can be read and controlled by a computer.

To determine the relative phase, ϕ, we first use a reference material. In our case,
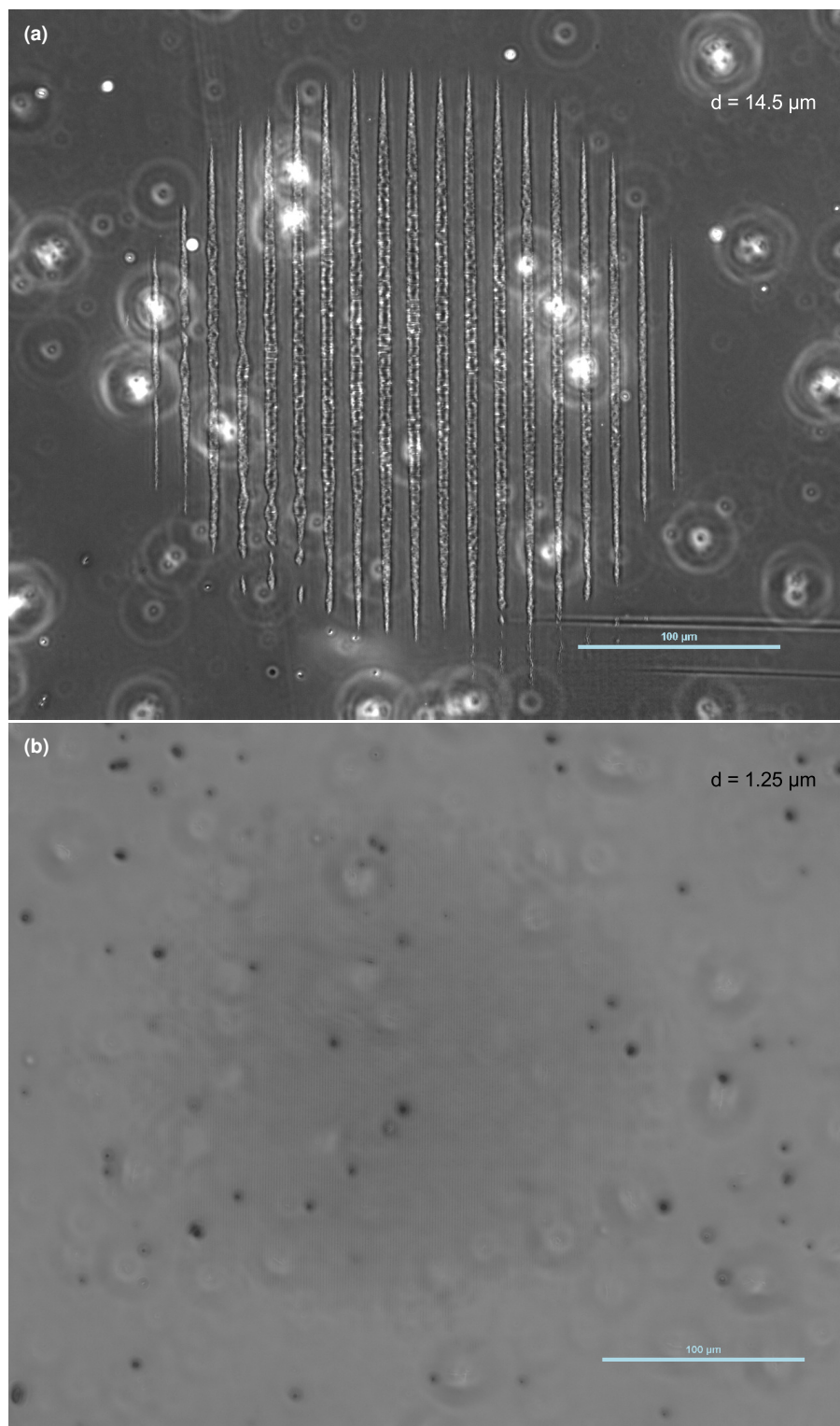
Figure 3.6: (a) Optical microscope image of a 14.5 µm grating pattern burned into a thin molecular film of spiro-OMeTAD. (b) Same as (a), but for a 1.25 µm grating. Due to the small grating size, if the pattern is not visible, zoom in (if viewing online).
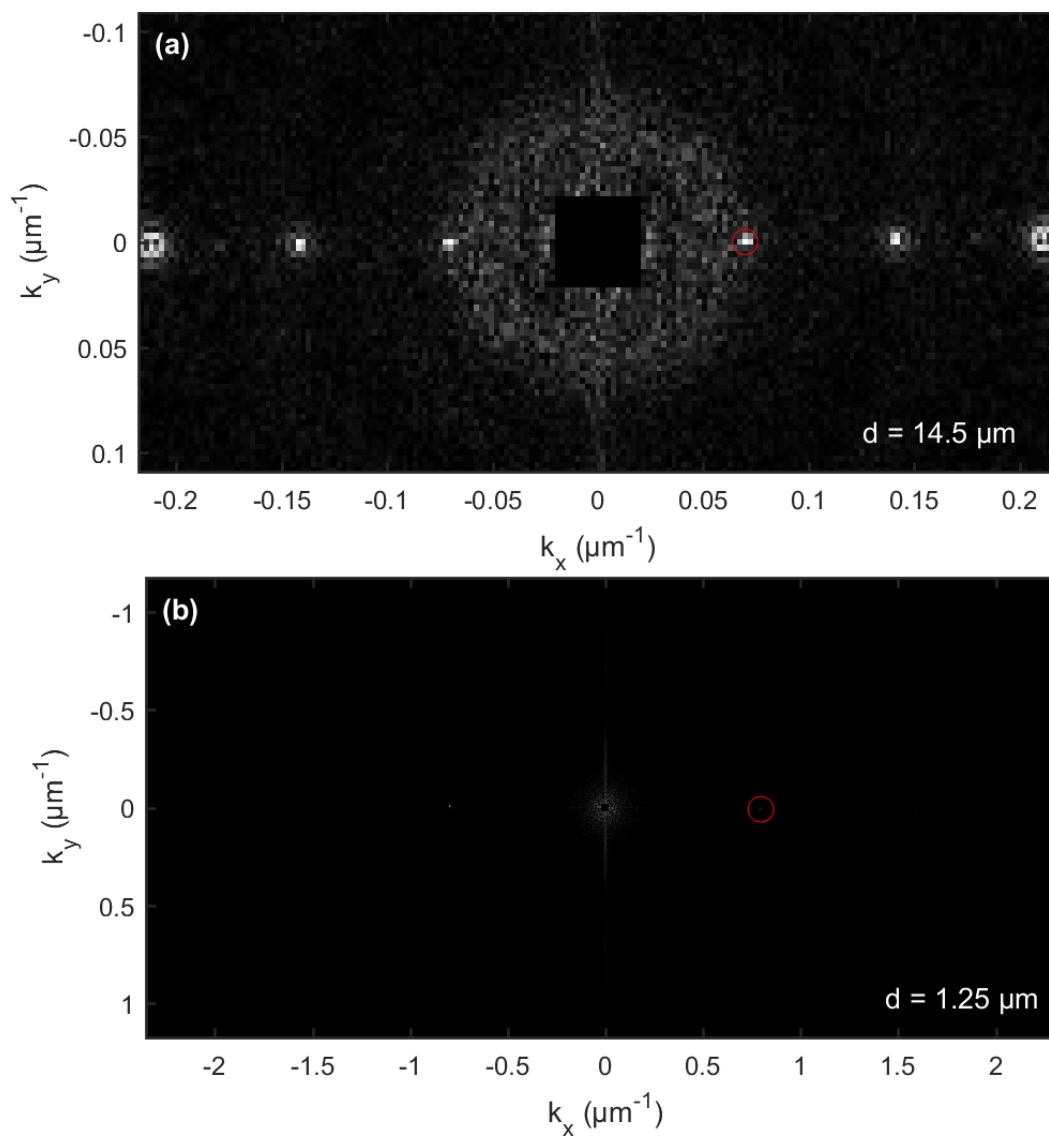
Figure 3.7: (a) 2-dimensional Fourier transform of optical microscope image of a 14.5 μm grating pattern burned into a thin molecular film (Figure 3.6(a)). The red circle identifies the peak where the grating wavevector has maximum intensity. The center wavevector is blocked out to avoid washing out the intensity in the remainder of the image. (b) Same as (a), but for a 1.25 μm grating image (Figure 3.6(b)).

we use a thick polydimethylsiloxane (PDMS) film, doped with a molecule called Malachite Green. This material only has a phase grating signal present as a result of the thermal grating. Recalling Eqn. 3.16, the amplitude of a phase grating signal is proportional to $\sin(\phi)$. Thus, we may systematically vary the displacement of the phase adjust motor and observe the magnitude of the thermal grating signal we measure. By relating this magnitude to the motor position, we have an exact function for ϕ as a function of the motor position.

To model the relationship between motor position and ϕ, we first relate the motor position displacement to the angle of the phase adjust optic.

$$\theta(p) = \arctan\left(\frac{p - p_0}{\ell}\right) \tag{3.80}$$

where p is the displacement of the motor, p_0 is the motor position where $\theta = 0$, and ℓ is the distance between the phase adjust mount's pivot point and where the motor is attached. Here we assume that the optic is fixed at its based and rotates according to the horizontal extension of the motor at the top. We then relate θ to the change in the optical path of the transmitting beam, and thus the change in relative phase.

$$\Delta\phi(\theta) = \frac{t}{\lambda}\left(1 - n - \cos(\theta) + \sqrt{n^2 - \sin^2(\theta)}\right) \tag{3.81}$$

where λ is the wavelength of the probe laser, t is the thickness of the glass, and n is the index of refraction of the glass. This expression can be derived using geometry and Snell's law.

An example of signal magnitude as a function of motor position is shown in Figure 3.8 along with the fitting of the above model to the data. In this example, one can see that the phase adjust optic is vertical around position $p_0 = 1.2$. Note, the gradual reduction in signal magnitude with position results from the fact that some beam displacement occurs up and down (perpendicular to the optical axis) at higher angles, which can reduce some optical alignment with the pump at the sample. Thus when fitting, the absolute magnitude of the signal is allowed to vary gradually. From the fitting, we can see that this model yields an excellent match to the data.

By repeating this procedure for any sample, the exact relative phase can be found. Then the exact motor positions can be used to achieve the right values of ϕ such that we can measure a phase (or amplitude) grating as part of the heterodyne detection scheme. An example of where careful heterodyne detection is important is shown in Figure 3.9(a). In this example, Au NPs that dope a polyethylene film cause a sharp, non-thermal signal at short timescales. The subtraction at the appropriate phases when heterodyning yields a much cleaner signal, as shown in Figure 3.9(b).
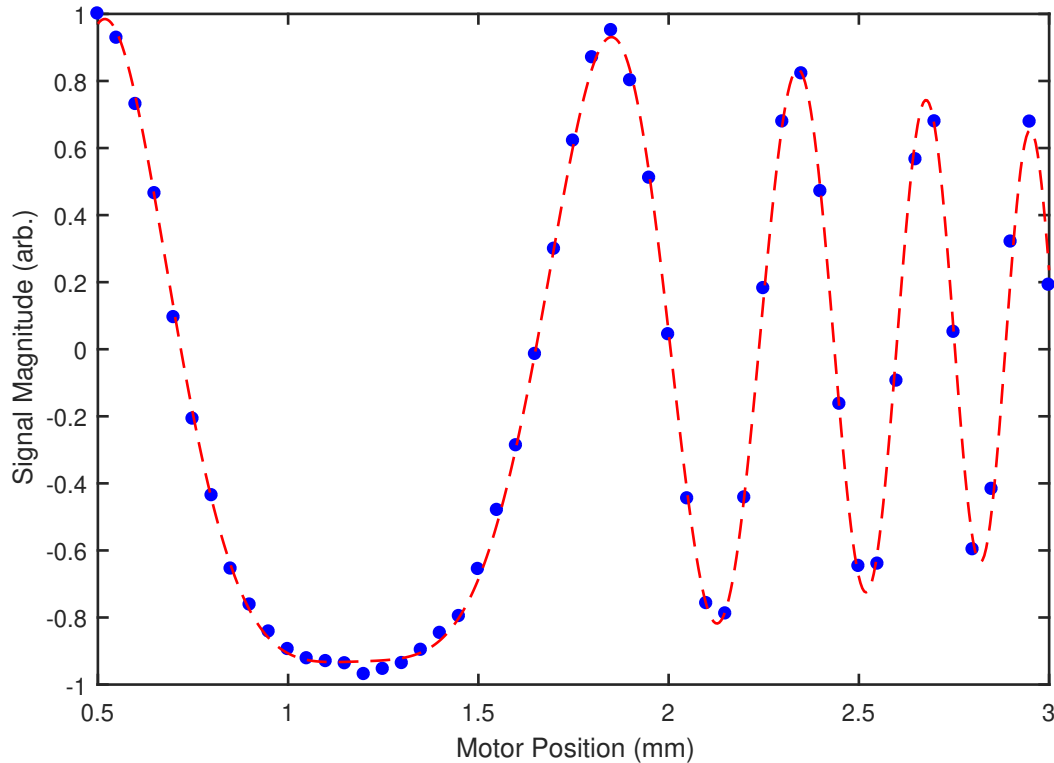
Figure 3.8: Signal magnitude vs phase adjust motor position for a thin film of PDMS. A fitting is shown in red corresponding to Equations 3.80 and 3.81. The good fitting shows the accuracy of the model, allowing the heterodyne phase to be known precisely as a function of motor position.

Detector Response

In Section 3.6, we derived the function $T(q_x, t)$, giving the amplitude of the thermal grating (with wavevector q_x) as a function of time in response to an instantaneous pump pulse. Ideally, we would directly measure this thermal amplitude as a voltage signal given by $f_0(t) \propto T(q_x, t)$. However, due to limitations in the photodetector, the actual signal measured is $f(t) \neq f_0(t)$. The reason for this disagreement is that all photodetectors are imperfect in how they translate an incoming optical signal into an outgoing electrical signal. For one, they always add additional noise to the signal. But more importantly, these detectors are limited by their frequency response function, which limits the frequencies they can measure.

If we first consider the balanced detector, it is rated nominally to measure from DC to 200 MHz. As a result, if the thermal decay profile is composed of frequencies higher than 200 MHz, these components will be largely filtered out, leading to a
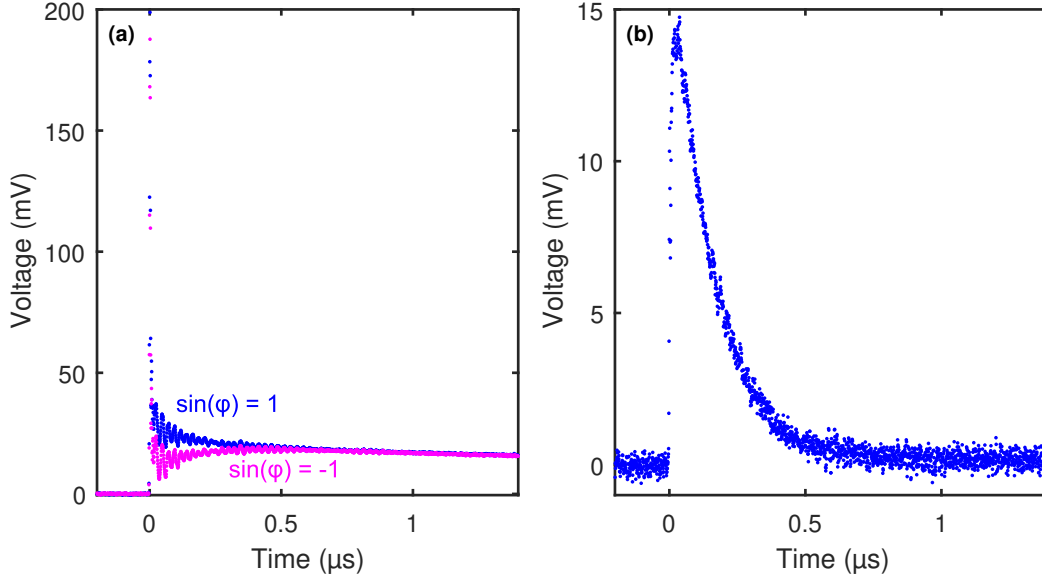
Figure 3.9: (a) Raw TG data for a highly oriented polyethylene film doped with Au nanoparticles, which have a significant non-thermal signal following the pump pulse. Both phases corresponding to the + and - signal are shown. (b) The subtracted signal for the data shown in (a). The unwanted signal is subtracted out, leaving only the thermal signal.

distorted signal. The actual signal measured by a detector is given by:

$$F_0(\omega) = \mathcal{F}[f_0(t)] \tag{3.82}$$

$$F(\omega) = H_{det}(\omega) \cdot F_0(\omega) \tag{3.83}$$

$$f(t) = \mathcal{F}^{-1}[F(\omega)] \tag{3.84}$$

where $\mathcal{F}$ denotes a Fourier transform. By using two detectors, we are able to use the balanced detector for signals with no significant signal components above 200 MHz, and we are able to to use the AC detector for faster signals. However, this latter detector has a nominal upper frequency cutoff of 1 GHz, which is limiting for signals on the order of ~1 ns.

Another limiting factor in measuring the expected thermal decay signal, $T(q_x, t)$ has to do with the assumption that the thermal grating was made instantaneously. Or equivalently stated, this assumes the pump pulse has a time profile given by a delta function, $\delta(t)$. However the pump pulse profile is more accurately described as a Gaussian profile in time, $g(t)$, with a pulse width[8] of 1.2 ns, in the case of our FlareNX laser.

---

[8]Full-Width Half-Max

Because solutions to Fourier's law are linear, the solution derived for a δ function, $T(q_x, t)$, can be convoluted with $g(t)$ to yield the new solution. This is equivalent to multiplying the Fourier transforms of these two functions. This relationship parallels the effect of the detector frequency response. Thus, we can write the full expression for the measured signal in terms of the detector response function and the pump pulse temporal profile, modifying Eqn. 3.83 above:

$$F(\omega) = H_{det}(\omega) \cdot G(\omega) \cdot F_0(\omega) \tag{3.85}$$

where $G(\omega)$ is the Fourier transform of the pump pulse temporal profile. With this expression, we can see that while there are two physically distinct sources of filtering the true thermal signal, they have equivalent mathematical interactions with the signal.

While we can use these equations to calculate the range of thermal signals that can be measured without experiencing significant distortion, we instead incorporate the above equation into our fitting process. Referencing Eqn. 3.85, our thermal model gives $F_0(\omega)$. By obtaining $H_{filt} = H_{det}(\omega) \cdot G(\omega)$, we can compute $F'(\omega)$ as a function of our fitting parameters and then compare to the measured data $F(\omega)$ during the fitting procedure.

To determine $H_{filt}(\omega)$, we simply measure the pump pulse directly with the detector. The measured signal will be $h_{filt}(t)$, which can be Fourier transformed to yield $H_{filt}(\omega)$. We incorporate this into our fitting procedure, which allows us to compensate for the fact that our pump pulse is not a δ function as well as for the detector's frequency response.

Accounting for the detector response and pulse width are irrelevant for a vast majority of the signals we measure, however highly conductive polymers being measured at low grating periods are otherwise impossible to accurately analyze with our available electronics without accounting for these effects. It should also be noted that additional error and decreased sensitivity naturally result from this procedure, but only in proportion to the fraction of high frequency components. The reduction in systematic error from this filtering effect easily outweighs this added error. Though to be conservative, we still restrict our measurements to signals where this filtering effect has not become too significant. Specifically, we do not measure thermal decay signals with decay timescales below ~2 ns.

Acquisition and Analysis Software

To efficiently and accurately collect and analyze TG data, we have developed software with graphical user interfaces (GUIs) using MATLAB. As an example, Figure 3.10 shows the GUI for collecting TG data. The interface contains sections for describing the current optical settings, as well as the sample being measured. It also interfaces with the oscilloscope as well as the phase adjust motor. This allows the previously mentioned phase calibration to occur automatically, thus increasing accuracy and speed of the process. It can automatically collect data for an arbitrarily long time, changing the phase adjust as necessary throughout, all regardless of the limits of the oscilloscope (which in our case could not collect data for longer than approximately a minute at a time). For many polymer samples measured for this thesis, which had terrible signal to noise ratios due to poor sample quality, this software-enabled extended acquisition was important for practically collecting enough data. Finally, the collected data would be saved with all the necessary optical and experimental information. While the experimental data acquisition could
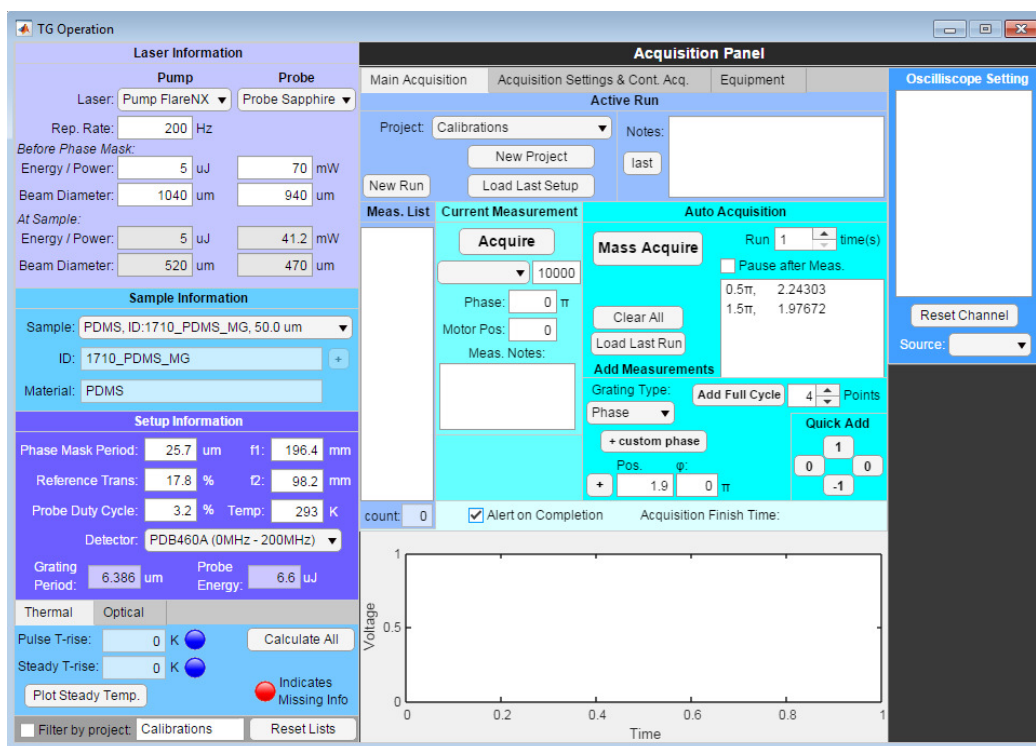
Figure 3.10: Image of the TG acquisition software graphical user interface. This is used to do phase calibration, record all experimental settings, and collect data by interfacing with the oscilloscope.

have been done with a much more limited software system, such as LabVIEW, the developed software was found to facilitate much more accurate and consistent data acquisition with a much greater throughput.

Similarly, an analogous GUI was made for data analysis, as shown in Figure 3.11. This interface allows sorting and filtering of all data sets. For any selected data, it displays all information pertaining to the acquisition. Most importantly, it contains an interface for analyzing the data and understanding the results. Finally, it is able to group related data sets for analysis, which is important for understanding thermal conductivity dependence on parameters such as grating period or temperature. Additionally, the software is especially useful for immediately fitting data being collected in real time from the TG Acquisition software, providing quick feedback as necessary. The most useful reason for having this more complex software tool for
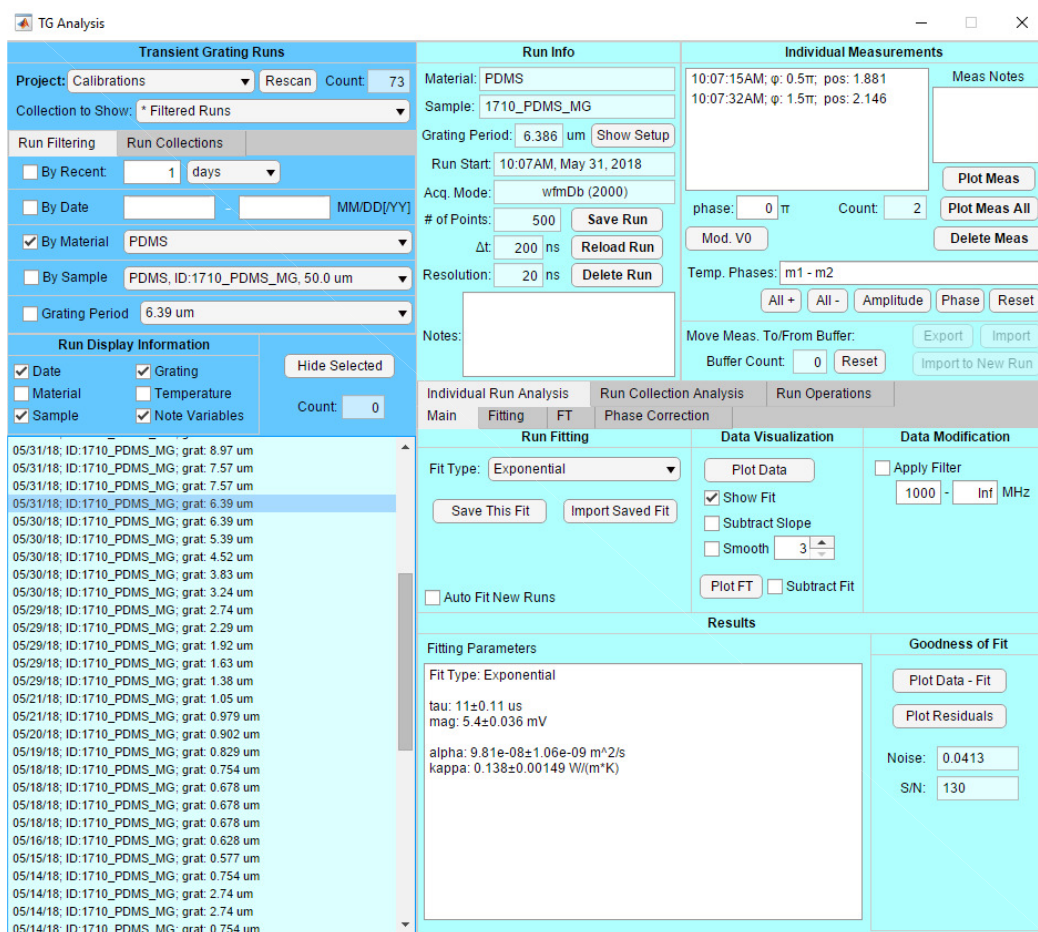
Figure 3.11: Image of the TG analysis software graphical user interface. This is used for accessing, sorting through, and automatically analyzing TG data.

data analysis is that it allows easy organization and access to all data previously collected. Having taken well over 1000 different data sets with the TG apparatus, this organized and searchable analysis software makes that possible without decreased change of error.

3.9 TG Example: Thermal Conductivity vs. Strain in PDMS

To demonstrate some of the advantages of the TG technique, we show an example here where thermal conductivity is measured in polydimethylsiloxane (PDMS) while it is being strained. Because the technique is an optical, non-contact method, any sample conditions that do not obstruct the optical path are compatible with the measurement. Because PDMS is nearly transparent, it is doped with trace amounts of Malachite Green dye to absorb a portion of the laser light.

The goal of this experiment was to observe the thermal conductivity as a function of strain. Taking advantage of the 1-dimensional, in-plane measurement, we repeated
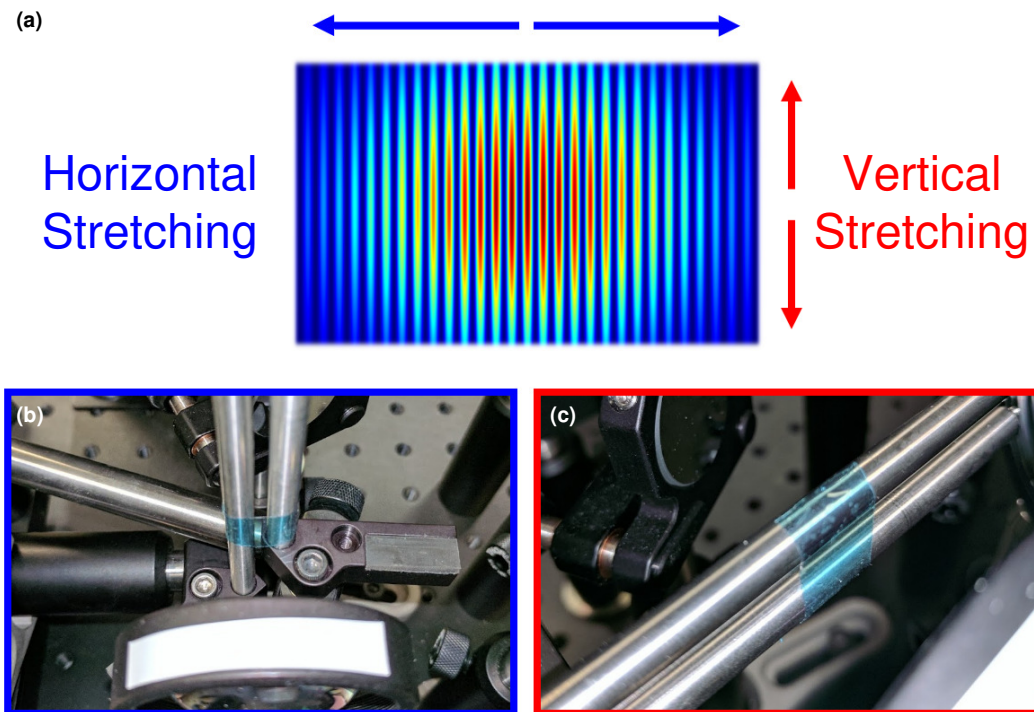
Figure 3.12: Apparatus for controlling strain shown for a free PDMS film while measuring with TG. (a) Schematic showing which direction is being stretched, overlapped with a schematic for the thermal grating, which is always horizontal. (b) Image showing the horizontal straining apparatus. (c) Image showing the vertical straining apparatus. Note: The pictured TG setup is from an earlier iteration than the one pictured earlier in this chapter.

the experiment while measuring parallel and perpendicular to the strain direction. Because the thermal measurement occurs horizontally (in the x-direction), the apparatus was set up for both horizontal and vertical strain, as shown in Figure 3.12.

PDMS films were strained until approximately ~200%, where fracture occurred. Thermal conductivity as a function of strain is shown both parallel and perpendicular to strain in Figure 3.13. Here we can see that κ experiences a notable increase parallel to the strain direction, up to ~17%. Perpendicular to the strain direction, there is no significant change in κ. The observed trends demonstrate that the increased polymer chain alignment results in better thermal transport, due to increased transport along polymer backbones. A particular advantage of using TG is that κ can be measured near-continuously while straining. We simply stopped at discrete points to average more data and increase signal-to-noise.
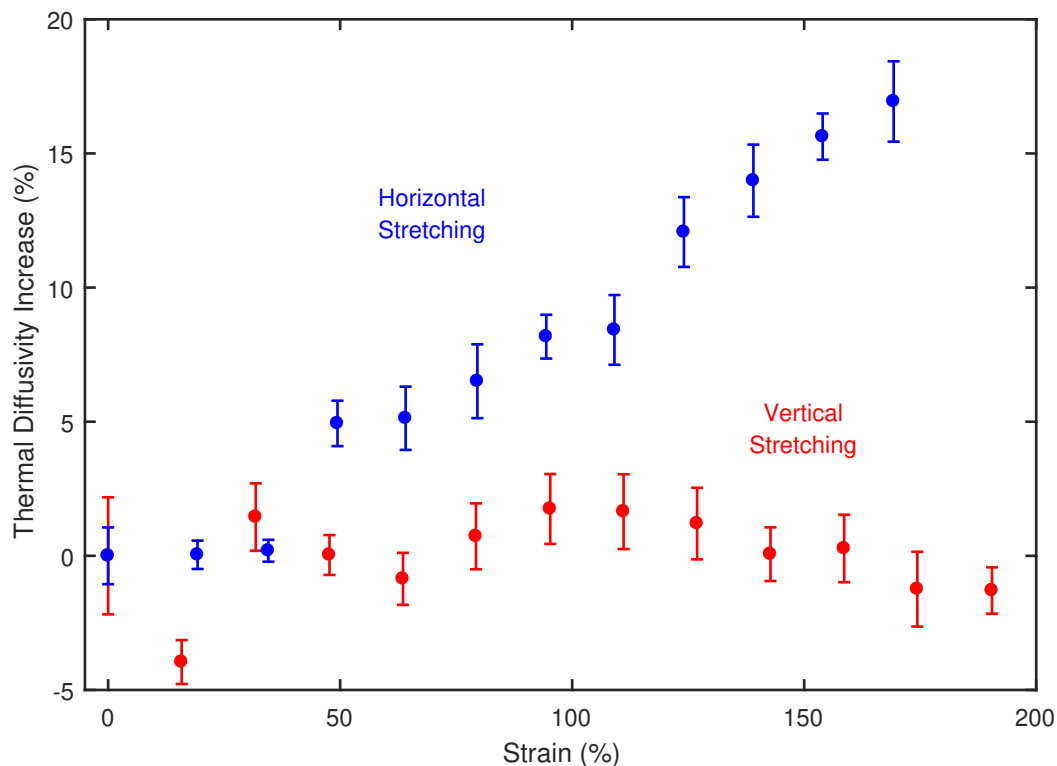
Figure 3.13: Thermal diffusivity as a function of strain, both parallel (horizontal) and perpendicular (vertical) to the measuring direction of TG. There is a clear increase in heat transport when stretching parallel, while the perpendicular direction has no significant change with strain. Two different strips of the same film were used for each set of points, until the film snapped close to 200% strain.

3.10 Summary

In summary, we have demonstrated how TG is especially suited for in-plane thermal conductivity measurements in polymer films. We have described how TG works, including the underlying working principles and the mathematical description. Further, we have described the important optical components that make the experiment work, including specific design choices that were developed with the express purpose of measuring polymers. We have also discussed the implemented strategies for efficient and accurate data acquisition and analysis.

Additionally, we have focused on the analysis and interpretation of TG data, especially relating to the thermal models applied to the measured signals. Not only have we discussed the familiar exponential model typically used with TG, but we derived a new model appropriate for thin films, enabling the accurate interpretation of a new type of sample geometry. Finally we have discussed additional considerations of easily forgotten features of the experiment, such as grating period calibration and detector response, which can critically impact the accurate interpretation of a measured signal.

We have also provided examples of our implementation of TG, including a demonstration of the importance of the thin film model. Lastly we presented an example of how TG can be applied to measuring anisotropic properties like strain-dependent thermal transport in a PDMS film.

In conclusion, TG can be used to probe polymer thermal transport especially well as compared to other techniques. In the next chapter, this method will be applied to an especially interesting material system, highly oriented polyethylene. In particular, the tunable grating period including very small length scales will become critical for probing thermal transport properties at the microscale.

Chapter 4

THERMAL PHONONS WITH MICRON-SCALE MEAN FREE PATHS IN SEMI-CRYSTALLINE POLYETHYLENE

This chapter has been adapted, in part, from:

> Robbins, A. B., Drakopoulos, S. X., Ronca, S. & Minnich, A. J. Thermal Phonons with Micron-Scale Mean Free Paths in Semi-Crystalline Polyethylene. *(In Preparation)*.

As laid out in the previous chapter, Transient Grating (TG) is especially suited not only for studying thermal transport in polymer films, but also for probing microscopic properties of the underlying heat carriers. In this chapter, we apply the TG method to oriented polyethylene (PE) films. While there has been significant work towards improving thermal conductivity in PE, reviewed below, investigations into the interplay between the underlying heat carriers and the PE microstructure have been speculatory and indirect. In this chapter, we use TG specifically to probe the phonon MFP spectrum, a first for a polymer.

4.1 Background

As described in Chapter 1, PE was one of the first oriented polymers to be studied for its high thermal conductivity, with work on oriented PE going back over 40 years[4, 5, 7]. Follow up studies focused on improving sample quality by increasing polymer alignment and/or increasing crystallinity[8, 9, 11–13, 15, 20, 21]. The highest draw ratio, which refers to the ratio of the final to initial sample length after stretching it, achieved was 350 and resulted in a thermal conductivity $\kappa > 40$ Wm^{-1}K^{-1}[11]. The highest value reported is for a PE nanofiber, at $\kappa \sim 104$ Wm^{-1}K^{-1}[12], though achieving this sort of value in a macroscopic sample is far more challenging. The highest reported in a film is $\kappa \sim 65$ Wm^{-1}K^{-1}[13, 14].

In an effort to increase thermal conductivity in PE as much as possible, many studies have explored different aspects of sample fabrication. One of the most obvious and focused on factors is the draw ratio, DR, which is able to increase thermal conductivity through a few different mechanisms. Up to $DR \sim 10$, κ can be improved by a factor of at least 20[5, 7, 9, 13]. Beyond this, especially

at ultrahigh ratios exceeding ~40, growth in the crystalline domain size can lead to further increases in thermal conductivity[11, 13, 22]. Both of these structural improvements are possible due to PE's initial microstructure. Because PE begins as a semi-crystalline material, with a distribution of crystallites randomly oriented in an amorphous matrix, early drawing is able to largely align the polymer chains, including the crystal domains and the amorphous regions. Once there is near uniform chain alignment, further drawing forces existing crystalline domains to grow.

Another factor that can increase κ is the crystallite size, independent of the overall crystal fraction[21]. In PE, the natural crystallite size can vary widely, but is typically in the range of 10 nm to 75 nm[91–94]. Assuming, the grain boundaries of these domains is one of the dominant scattering mechanisms in PE, increasing their size, at a constant crystallinity, can increase κ.

Finally, separate from the crystalline portion of PE, the amorphous fraction can also play a role in increasing κ. While this portion is relatively less understood, numerous studies have shown that highly aligned amorphous polymers can also increase thermal conductivity considerably[12, 15, 20]. The extent to which these regions interact with the crystalline domains is unknown.

To put these experimental findings in perspective, a recent ab-initio calculation on a perfect PE crystal found $\kappa = 164$ Wm^{-1}K^{-1}, due in large part to phonon MFPs as high as 1 μm. However the perfect crystal assumed in these calculations ignores the imperfections and inhomogeneous composition in real PE films. While the greatly reduced thermal conductivity can be attributed to a lack of chain orientation or scattering off of a variety of microstructural features, the exactly relationship between these factors and the underlying heat carriers has been left to speculation.

In this chapter, we apply the TG technique to PE films, using its unique ability to probe a single in-plane direction at a tunable length scale to observe quasi-ballistic heat transport, an observation that has never been made in polymers. Then, we discuss how these measurements can directly yield the underlying phonon MFP spectrum. We then use these results in conjunction with structural characterization techniques to understand what key factors are most limiting to heat transport. We then comment how this relationship can inspire fabrication and processing changes to best maximize thermal conductivity.

4.2 Sample Information: Oriented Polyethylene Films

All PE results presented in this chapter refer to PE films made by our collaborators at Loughborough University in the UK, specifically Stavros Drakopoulos and Sara Ronca. Sample fabrication is discussed in previous works of theirs[13, 22]. Of the fabrication and processing, we are most interested in the drawing process. All samples are drawn by one or both of two processes. First, the samples may be rolled, which thins and spreads the films, though this technique is limited in the draw ratio that can be achieved (a maximum of 7.5 in this thesis). Second, samples may be stretched under tension. Combined, these methods have yielded samples up to a draw ratio $DR \sim 200$. The thickness of all films were not measured, however rough measurements on a few found that the thicknesses ranged from $\sim 20\,\mu m$ to $\sim 100\,\mu m$, with thicknesses being inversely proportional to the draw ratio.

Like the other polymers discussed already, PE is naturally transparent. Thus we must introduce trace amounts of dye or fillers to facilitate absorption of the pump laser in TG. We used and compared 3 different fillers: ZnO nanoparticles (NPs), Au NPs, and beta-carotene (BC). All were found to be stable, however the Au NPs, which had a diameter $< 10\,nm$ and strongly absorbed green light, were found to have a complex relaxation process which resulted in an unwanted background signal of significant magnitude. While Chapter 3, Section 3.8 provides an example of how a majority of this signal can be subtracted through heterodyne detection, a portion of the unwanted signal was present in the phase grating signal at very short timescales, which could not be reliably removed and thus distorts thermal signals, though only at low grating periods where the decay is on the order of $10\,ns$. Both the ZnO NPs (with diameters $< 100\,nm$) and BC did not have any significant non-thermal signal that inhibited thermal modelling.

In applying TG to these PE films, one particular challenge arose from intense light scattering caused by inhomogeneities resulting from the stretching process. Figure 4.1 shows examples of 4 samples, showing the difference in appearance as the draw ratio is increased, in addition to the coloration introduced by different fillers. Figure 4.1(c) and (d) show films with fiber-like striations distributed throughout the film. These features are present at the µm scale and thus are effective at scattering visible light. In cases of significant presence of this light scattering, application of TG is essentially impossible, though all samples shown do coherently transmit enough light for measurements to proceed. One way to amplify the signal in these cases is to remove the ND filter from the path of the reference probe beam. As
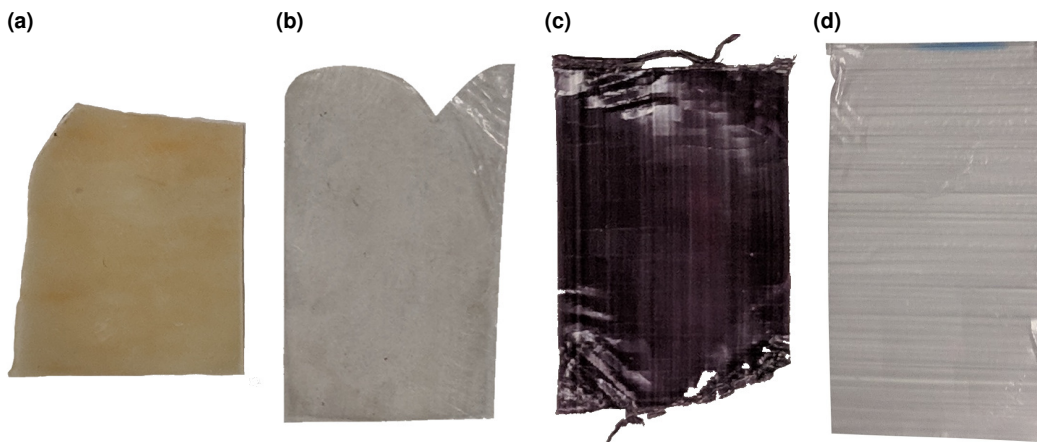
Figure 4.1: Images of 4 polyethylene films with different draw ratios and fillers. (a) (BC2.5) *DR* =2.5 from rolling only; filler: beta-carotene, with an orange color. (b) (ZnO7.5) *DR* =7.5 from rolling only; filler: ZnO NPs, which is mostly still transparent. (c) (Au72.5) *DR* =72.5 from rolling and stretching; filler: Au NPs, which has a strong purple-red color. Despite this high absorption, a strong signal is still given by this sample. (d) (Au196) *DR* =196 from rolling and stretching; filler: Au NPs, with a smaller concentration. This sample and (c) have clear striations along the draw direction, which leads to significant light scattering.

discussed in Chapter 3, this optic is specifically used to limit the total DC power into the detector. However the low coherent transmission makes this optic unnecessary for high draw ratio PE films.

4.3 Transient Grating on Oriented Polyethylene

Considering now the thermal conductivity of our PE films measured with TG, Figure 4.2(a) shows an example of raw data collected on a PE film with BC and *DR* = 2.5, referred to as BC2.5. To extract the thermal conductivity from the data, we implement the thermal model as described in Chapter 3, Section 3.6. This amounts to an exponential decay, which is what is shown in red as the fitting. Here we find an excellent fit. Note that the thermal model fits for thermal diffusivity. The thermal conductivity is calculated using an assumed heat capacity and density, based on previously published data[95]. Error in these values does not affect trends, except potentially for temperature-dependent measurements. However these variations are believed to be insignificant.

While the exponential fitting in Figure 4.2(a) shows excellent agreement, with different samples, and under different conditions, we at times have non-thermal signals that partially distort our desired exponential decay, as was discussed briefly
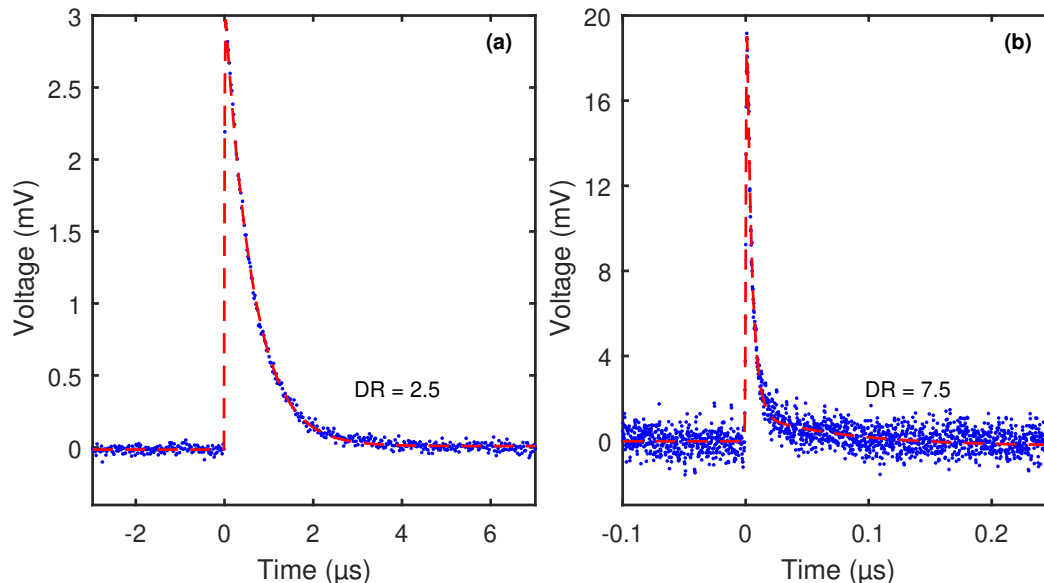
Figure 4.2: Raw TG signal for 2 PE films. (a) BC2.5 with an exponential fitting shown in red. (b) ZnO7.5 with a more complicated fitting model. An exponential fitting, representing the thermal signal, is dominant, while a very short and long exponential decay are added to fit the non-thermal signal components.

in Chapter 3. To account for these other signal sources, we need a more complex model.

Fitting Non-Thermal Signals

Figure 4.2(b) shows a signal for PE with ZnO NPs, with $DR = 7.5$, referred to as ZnO7.5. One can easily see that this signal exhibits a small non-thermal signal, specifically in the form of a low-magnitude, slow decay after $t = 0$. Though difficult to see without zooming in, there is also an extremely fast decay at $t = 0$ (with a negative magnitude). For this and similar signals, we use a model of the following form:

$$V(t) = b + st + u(t)\left(b_2 + m_1 e^{t/\tau_1} + m_2 e^{t/\tau_2} + m_3 e^{t/\tau_3}\right) \qquad (4.1)$$

where $u(t)$ is a unit step, b is the background constant, b_2 accounts for a different background after t_0, s is the background slope of the data, and m_i and τ_i are exponential fitting parameters.

While this model incorporates many parameters, all of them are seldom used simultaneously, and if they are, we use the following guidelines to ensure proper sensitivity to the thermal decay constant, which is the one parameter we are interested in. First, the background b as well as the first exponential term, with m_1 and

τ_1, are standard parameters for a simple exponential fitting. In Figure 4.2(b), the thermal decay is 3.9 ns.

As for the additional parameters, the second exponential decay is used to account for the excitation and thermalization of the filler and in this case has a fitted value of 120 ps[1]. This is a typical value, well below the thermal decay time, and generally has little to no impact on the overall fitting due to how short it is. However, we include it in an effort to account for all physical signal sources.

Next, we have a third exponential to account for long-term relaxation processes beyond the thermal signal. The source of this signal is not well understood, however we theorize it arises from the significant spatial variations across the drawn polymer samples. As can be seen in Figure 4.1, especially at high draw ratios, inhomogeneities at the μm scale affect the light transmission. As a result, small deviations in sample position may affect absolute signal magnitude[2]. While the heterodyne detection scheme would generally remove such signals, because the relative probe phase is changed via a rotating glass optic, the beam is translated up and down (only on the order of μms). However, we have observed this variation to be enough to alter the signal. If the pump excitation is sufficient to move the sample in any way, each signal in the heterodyne detection scheme may respond slightly differently. Importantly, because the total DC power entering the detector is generally at least 3 orders of magnitude larger than the magnitude of the signals being detected, any small fluctuations in the total power transmitted can be significant relative to the signal. Consequently, the third exponential, in addition to the second background term b_2, are meant to account for any deviations after $t = 0$. In the case of Figure 4.2(b), the fitted decay is 76 ns, which is more than an order of magnitude larger than the thermal signal, and thus does not significantly impact its sensitivity.

Finally, the slope term, s, is generally only used for very long signals, spanning many tens of μs. Occasionally, this term is necessary due to variations in the probe power, which may arise due to the sample, or other optics in the setup heating up. As the effect is exceptionally small, with changes in voltage several orders of magnitude smaller than the signal magnitude over ~10 μs, it can only be noticed over these long time scales. Again, because the DC signal is so much larger than the signal

---

[1]This fitted parameter actually has a large uncertainty in the regression, which is common. This indicates that the parameter is insensitive with regards to the fitting procedure, especially compared to the thermal decay.

[2]This is further supported by the fact that small translations of the sample randomly affect the magnitude of the intensity.

magnitude we look at, power variations below 0.1% would still be noticeable.

In summary, practical fitting of the ideal thermal model is frequently paired with accounting for other signals. While the above equation includes many fitting parameters, we fit most signals with a simple exponential decay, and only include extra parameters when there is a clear presence of another signal. However, even when they are included, their magnitude may be so small that they become negligible anyway. When this is the case, there is no cost to their inclusion. We also ensure other exponential decays that are incorporated are at least an order of magnitude different from the thermal decay to maintain sensitivity in the thermal fitting.

Uncertainty Analysis

To quantify the uncertainty of a given measurement, we first took the 95% confidence interval representing the standard error of the fitting procedure. For this we used a nonlinear regression, specifically least squares, as implemented in MATLAB's Statistics and Machine Learning Toolbox. This accounted roughly for the error inherent to a given signal. We frequently reduced this error by collecting more data, or increasing power such that the signal-to-noise ratio was increased. Additionally, we also considered other sources of error.

While the fitting procedure assumes a true value κ and assumes it is distorted by noise from the TG experiment, this κ may also come from a distribution caused by spatial variations across the sample, as previous discussed. To account for this, we compared fitted thermal conductivity values taken at different times on different spots on a sample to estimate the distribution. For this we used ZnO7.5, and we compared 8 independent measurements. We found the standard deviation of the measurement amounted to a relative difference of approximately 3.5%. As a result, all presented results incorporate the addition[3] of both the fitting error and the error from spatial variations. This fractional difference is extrapolated to other samples. Note that this is a conservative estimate of the error.

4.4 Angle-Dependence in Oriented Polyethylene

Considering now the thermal conductivity of our PE films measured with TG, we first performed angle-dependent measurements, which establish how the oriented chains both improve conductivity along the chain direction, and also if and how κ changes in the perpendicular direction. Figure 4.3(a) shows the angle-dependent

---

[3]Error additions were carried out by adding the variances and then converting back to 95% confidence bounds.
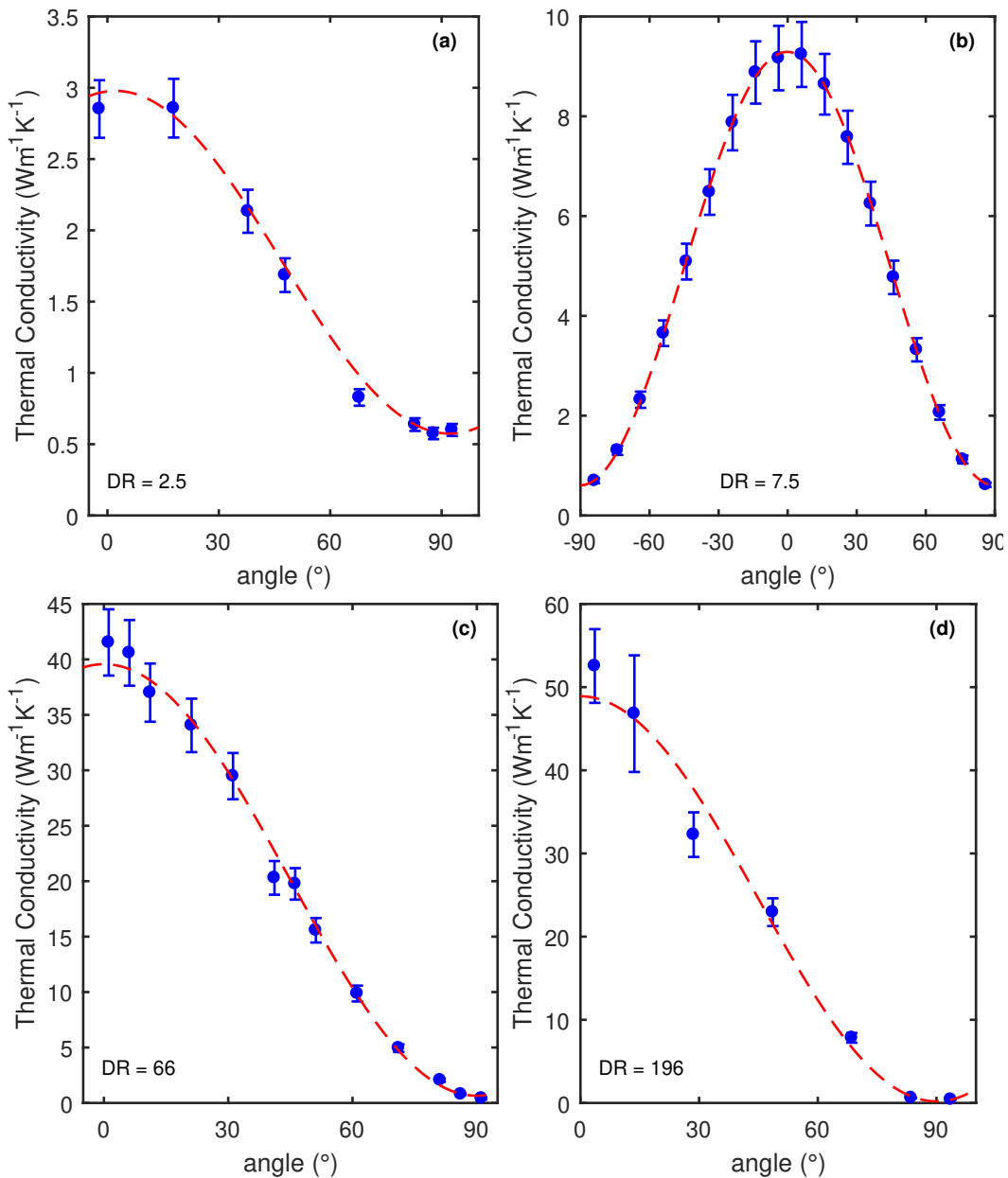
Figure 4.3: Angle-dependent thermal conductivity measured with TG on 4 samples by rotating the samples with respect to the optical setup. (a) BC2.5 with a peak κ of 2.98 ± 0.22 Wm^{-1}K^{-1}. (b) ZnO7.5 with a peak κ of 9.29 ± 0.05 Wm^{-1}K^{-1}. This plot shows the symmetry over $180°$. (c) Au66 with a peak κ of 39.6 ± 2.0 Wm^{-1}K^{-1}. (d) Au196 with a peak κ of 48.9 ± 8.4 Wm^{-1}K^{-1}. Note all reported errors here and in the plot refer to the 95% confidence intervals.

κ for a BC2.5. Note, even with a relatively small draw ratio of 2.5, the thermal transport anisotropy is already approximately 5.

Looking next to Figure 4.3(b), we consider the same measurement for ZnO7.5. Here we have measured over a full 180°, finding unsurprisingly that κ is symmetric. For this sample, we find a peak $\kappa = 9.29 \pm 0.05$ Wm^{-1}K^{-1}, with an anisotropy ratio of approximately 15. Finally, both Figure 4.3(c) and (d) show similar plots for PE with Au NPs, with $DR = 66$ (Au66) and $DR = 196$ (Au196), respectively. Here we see large anisotropy ratios on the order of 100.

For all plots in Figure 4.3, the results were fit to a simple geometric model based on Fourier's Law that considers κ to be composed of a separate $\kappa_\parallel$ and $\kappa_\perp$ component, with each contributing independently to heat transport in proportion to their alignment with the temperature gradient.

$$J_x = -\kappa_x \nabla_x T \tag{4.2}$$

$$J_x = J_\parallel \cos \theta + J_\perp \sin \theta \tag{4.3}$$

where we have expressed the heat flux, J in terms of our temperature gradient, which is in the x-direction. We then expressed J as the combination from transport in the two principle directions of the material system. Following this, we look to define $J_\parallel$ and $J_\perp$.

$$J_\parallel = -\kappa_\parallel \nabla_\parallel T \tag{4.4}$$

$$J_\parallel = -\kappa_\parallel (\nabla_x T) \cos \theta \tag{4.5}$$

where we have expressed $J_\parallel$ in terms of the component of the temperature gradient in the parallel (oriented) direction, as well as the component of κ in that direction. We can write the same expression for $J_\perp$

$$J_\perp = -\kappa_\perp (\nabla_x T) \sin \theta \tag{4.6}$$

Finally, we plug back into Eqn. 4.3

$$J_x = -\left(\kappa_\parallel \cos^2 \theta + \kappa_\perp \sin^2 \theta \right) \nabla_x T \tag{4.7}$$

where if we equate to Eqn. 4.2, we have an expression for κ in the direction of the grating. Note, $\theta = 0$ corresponds to the parallel direction. Considering again the plots in Figure 4.3, we find excellent agreement with the model. We also point out that not only is the peak κ increasing considerably with draw ratio, but that the κ minimum appears to be decreasing at high draw ratios, which is likely in response to transport being entirely over inter-chain interactions.

4.5 Grating dependent measurements

Having successfully used TG to measure the anisotropic thermal conductivity in PE, we next move on to conducting grating-dependent κ measurements. These measurements, utilizing one of TG's most critical capabilities, are the most important and novel measurements of this chapter. If κ is found to have any dependence on the length scale over which it is measured (corresponding to the grating period d), this trend must be due to quasi-ballistic heat transport as discussed in the next section[50–53]. Briefly, the origin of this trend is the overprediction of the heat flux by Fourier's law for a given temperature gradient. The result is that the apparent thermal conductivity is lower than the bulk value. As a general guideline for interpreting the data, an observed suppression of κ compared to the bulk value at a grating period d suggests the presence of phonons with MFPs on the order of $\lambda \sim \frac{d}{2\pi}$.

For context, ab-initio calculations on a perfect PE crystal have predicted significant contributions to thermal conductivity from phonons with MFPs in the range of $10\,\mathrm{nm}$ to $1\,\mathrm{\mu m}$[24]. This is of course for a perfect crystal. One of the critical purposes of this experimental work is to determine these microscopic thermal properties in real films. There are a few main reasons why we would not find such long MFPs in a real film. The first is that the relatively long MFPs predicted for a crystal are only along the chain direction, and measurements on partially oriented chains would have lower intrinsic MFPs. The second explanation is that the crystalline domains that are present are small relative to scattering expected in an infinitely large crystal. Then scattering at domain boundaries would lower MFPs. Third, there may be significant defects due to the disordered structure, which result in more scattering than in a perfect crystal. Overall, real PE samples have numerous potential sources of structural and defect scattering that have the (likely) potential to drastically limit the phonon MFPs.

We measured several PE films (in the oriented direction) at a range of grating periods, spanning $577\,\mathrm{nm}$ to $15.7\,\mathrm{\mu m}$. The especially low minimum grating period obtainable in our setup is what enables us to probe MFPs that would otherwise be impossible to detect. We limited our measurements to low to moderate draw ratios, because a majority of our high draw ratio PE films scattered too excessively to measure. Only Au NP-doped films provided enough signal for measurements; however, due to signal distortion at small time scales caused by the excitations of the Au NPs, low grating periods (corresponding to small decay times) were impossible

to accurately model.

Figure 4.4(a) shows the grating-dependent measurement for BC2.5. One can see that it has no statistically significant grating dependence. Given how partially oriented and relatively low κ still is, this is not unexpected. Next, Figure 4.4(b) shows the same plot for a $DR = 5$ sample (ZnO5). In this case, there is a notable decrease in κ below ~800 nm. This result is significant because it suggests that even at a relatively low draw ratio, with moderate improvements to κ over unoriented PE, relatively long MFPs may already be present. Figure 4.4(c) shows a $DR = 7.5$ PE film (BC7.5), which shows a clear grating dependence, especially below ~1 μm. Note, the maximum κ is already approximately 10 times larger than unoriented PE, largely due to the significant amount of chain orientation that has already occurred.

Finally, Figure 4.4(d) shows a different $DR = 7.5$ film, ZnO7.5. While the peak κ value differs between (c) and (d), that has to do with variations in the drawing process. The best indicator for the draw ratio is actually the peak κ value. As a result, one can take the effective draw ratio of (d) to be larger than (c). In this case, the peak κ is about 15 times larger than unoriented values, with polymer chains being largely aligned, though not completely. Here we observed significant grating dependence to κ below ~1.5 μm, with a reduction in κ of at least 1/3 from the peak value. This plot in particular provides strong evidence of long MFP phonons in these PE films.

In addition to measuring different samples, we considered grating-dependent κ at low temperature. Figure 4.5(a) shows ZnO7.5 measured at 100 K. While the overall κ is lower due to the lower heat capacity, a similar grating dependence is observed. On first glance, this suggests the MFP spectra in the two cases is similar.

Furthermore, we also verified the grating dependence perpendicular to the orientation direction. We used a highly drawn sample to select for only inter-chain transport. We used a Au NP-doped film with $DR = 73$, or Au73. Because we were measuring in the direction perpendicular, the decay times were sufficiently large to avoid signal distortion from the Au NPs. Figure 4.5(b) shows this data, showing as expected that there is no grating dependence when looking perpendicular to the oriented chains.

Having conclusively demonstrated the presence of relatively long MFP phonons in real PE films, we next consider how to interpret this data. We will show how the MFP spectra is related to the grating-dependent thermal conductivity and how
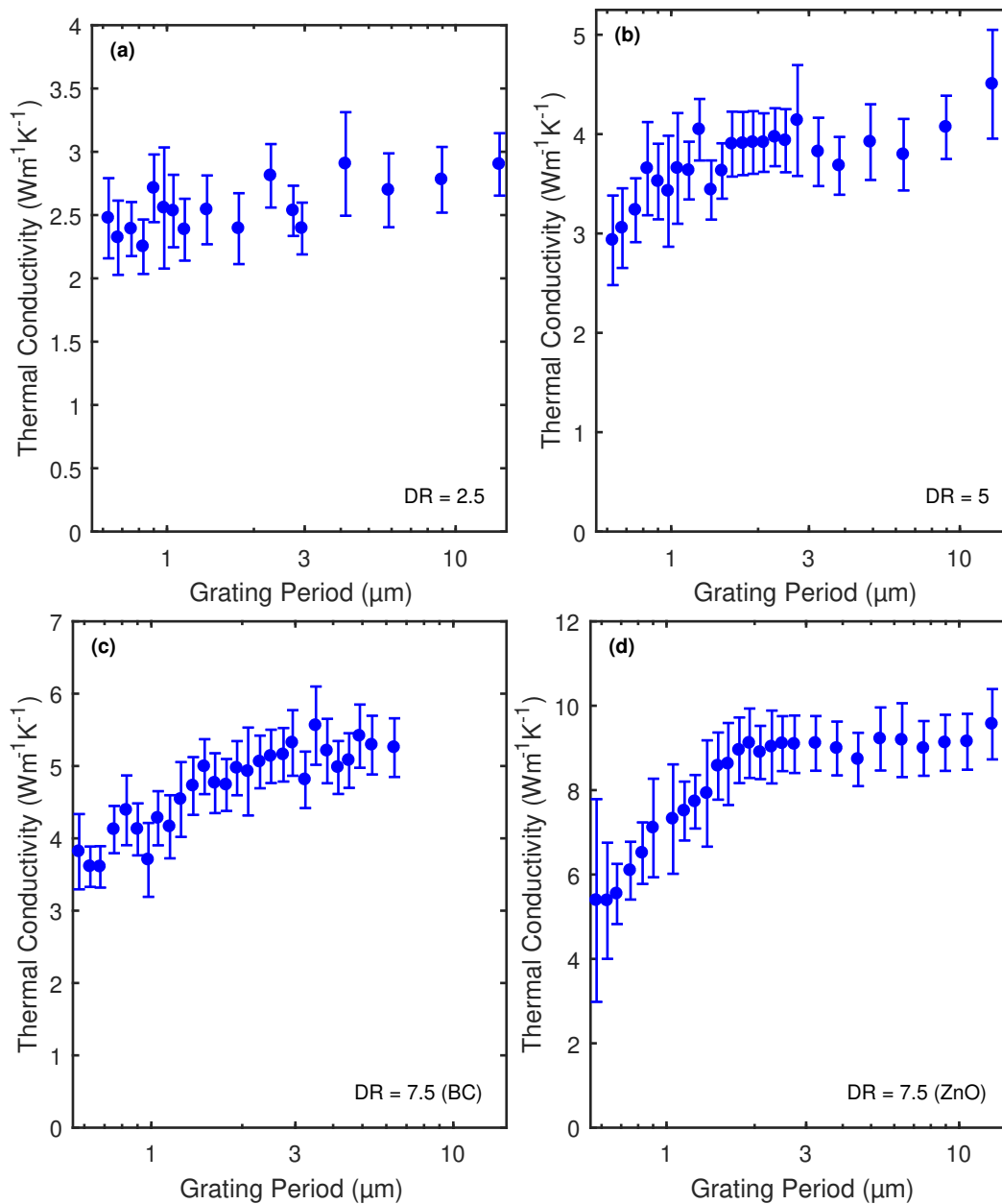
Figure 4.4: Grating-dependent thermal conductivity measured with TG on 4 samples by varying the grating period, covering as low as 577 nm up to 15.7 μm. (a) BC2.5, no meaningful variation with grating period. (b) ZnO5, there is a small decline in κ below 1 μm. (c) BC7.5, there is steady decline in κ, particularly by ~1 μm. (d) ZnO7.5, there is a significant decline in κ below 1.5 μm. Note, due to sample variations, (d) has a higher peak κ, which is a better indicator of how drawn it truly is. All error bars refer to the 95% confidence intervals.
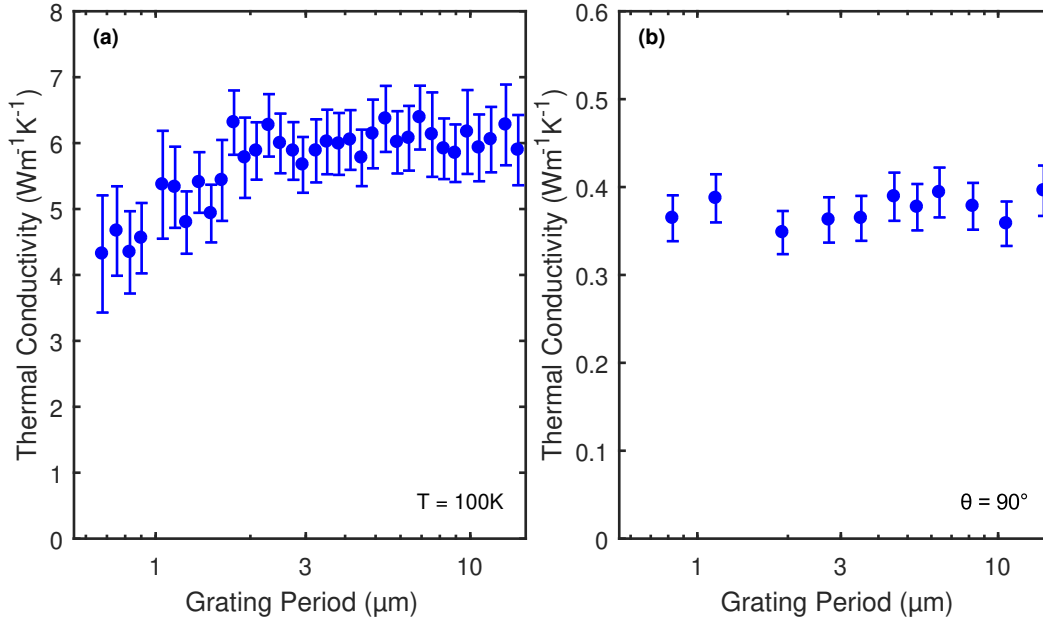
Figure 4.5: Grating-dependent thermal conductivity measured with TG for: (a) ZnO7.5 at 100 K, exhibiting a notable decrease in κ below 1.5 μm. (b) Au73, perpendicular to the orientation direction. There is no grating dependence, as is expected. All error bars refer to the 95% confidence intervals.

this relationship can be used to estimate the MFP spectrum for each PE film. This procedure is pivotal for providing novel insight into microscale heat transport properties in PE.

4.6   Quasi-Ballistic Heat Transport

A theoretical basis for quasi-ballistic heat transport as been established[50–53] that explains how thermal transport measurements at small length scales begin to deviate from Fourier's Law and reduce the apparent thermal conductivity. Further, many experiments with tunable thermal length scales have demonstrated the effect in recent years, both with TG[54] and with other methods[35, 51, 55–59]. Importantly, several works have used this understanding to estimate the underlying MFP spectrum from experimental data[51–53]. In this section, we outline the mathematical framework as laid out in these works. In subsequent sections, we will describe the numerical algorithms we use to carry out the MFP reconstruction and present results of this reconstruction for data on PE films from the previous section.

Aside: A Physical Picture

While a full mathematical derivation for quasi-ballistic heat transport in the TG experiment can be found in the previously cited publications, we take a moment here for a brief aside in an effort to provide an intuitive explanation of quasi-ballistic heat transport for those who are unfamiliar. Ballistic transport, and the intermediate quasi-ballistic regime, often elicit the idea of efficient transport due to a lack of scattering events. However, this effect leads to a *reduced* apparent thermal conductivity. While the details vary based on the experiment being discussed, we offer here a physical picture to help provide an intuitive understanding of the source of this reduced κ in the TG experiment.

Considering Fourier's Law, $J = -\kappa \nabla T$, we expect a heat flux to be driven by a temperature gradient in proportion to κ. One interpretation of quasi-ballistic heat transport can be rooted in the nuances of the temperature gradient. While it is trivial to write down a temperature profile as a continuous function of space, from a phonon's perspective, the effective temperature gradient is really just based on the difference between the local temperature where a phonon is generated and the local temperature where a phonon is scattered (destroyed). The reason for this is that a heat flux arises from the surplus of phonons originating from a hotter region compared to the counteracting phonons originating from the colder region.

Now, consider the sinusoidal thermal profile that is created in a TG experiment. Let us define the distance between the peak (hot) and low (cold) point of this profile as $L = \frac{d}{2}$. We can then define the difference in temperature between these two extremes as ΔT. The approximate temperature gradient between these points is thus $\frac{\Delta T}{L}$. If one considers a particular phonon mode with a MFP of $\Lambda = \frac{3}{2}L$, originating from a hot point of the profile, a large portion of these phonons will actually experience an effective temperature gradient closer to $\frac{\Delta T}{2} \frac{2}{3L} = \frac{\Delta T}{3L}$ because they will pass the cold point and be halfway to the next hot point by the time they scatter. In this scenario, the effective temperature gradient is reduced by a factor of 3. For a much longer grating period, this would not be the case. Going even further, for a MFP equal to $2L$, many phonons would experience no significant temperature gradient whatsoever. This scenario breaks with Fourier's Law because long MFP phonons now experience a relatively reduced temperature gradient compared to short MFP phonons. As a result, long MFP phonons' contributions to κ are suppressed not because their transport is somehow inhibited, but rather because the effective temperature gradient they experience is reduced, thus lowering their relative contribution to the heat flux.

We would like to stress that these descriptions are qualitative in nature and should only be used to help build an intuition. The full quantitative picture is more complex and requires the solution to the Boltzmann transport equation. The relevant mathematical descriptions and references are provided in the next section.

The Mean Free Path Spectrum and the Suppression Function

The quantity we are specifically interested in is the MFP spectrum of a given material, which can be described by the differential MFP distribution of thermal conductivity, $f(\Lambda)$. This function gives the relative contribution to κ per unit length at any given MFP, Λ. Similarly, we can define the cumulative MFP distribution of thermal conductivity, $F(\Lambda)$, as:

$$F(\Lambda) = \int_0^\Lambda f(\Lambda')d\Lambda' \qquad (4.8)$$

As the grating period is lowered and approaches the longer MFPs present in a material, these phonons will start to be suppressed, thus contributing less to the overall thermal conductivity, and leading to a reduction in $f(\Lambda)$.

We follow Minnich[52, 96] and describe the thermal conductivity suppression according to the quantity $x = q\Lambda$, which is proportional to the ratio between MFP Λ and grating period d:

$$\kappa(q) = \int_0^\infty qF(\Lambda)K(x)d\Lambda \qquad (4.9)$$

$$K(x) = -\frac{\partial S}{\partial x} \qquad (4.10)$$

$$S(x) = \frac{1}{1 + x^2} \qquad (4.11)$$

where $S(x)$ is the suppression function. To better understand the influence of $S(x)$, we can see that a phonon with a MFP where $\Lambda = \frac{1}{q}$ such that $x = 1$, which is equivalent to $\Lambda = \frac{d}{2\pi}$, will be suppressed by 50%. As a result, the effective thermal conductivity that is measured will be smaller relative to the value predicted by Fourier's Law.

Considering Eqn. 4.9, both q and $K(x)$ are known. If we already had $F(\Lambda)$, as is the case for many ab-initio calculations, computing κ for a particular grating period is simple and fast. However, our challenge comes from reversing the equation. Because Eqn. 4.9 essentially amounts to a convolution, going backwards amounts to a deconvolution, which is an ill-posed problem, lacking a unique solution.

4.7 Bayesian Inference: Solving for the MFP Spectrum

To find $F(\Lambda)$, we must find a spectrum that, when plugged back into Eqn. 4.9, closely matches the experimental data. However we must also impose some constraints to aid in the deconvolution to ensure a sensible solution. To effectively solve this problem, we add a constraint that our cumulative MFP distribution $F(\Lambda)$ must be relatively smooth, as has been done previously[52]. We find this a sensible choice because reported spectra from ab-initio calculations are typically smooth, as is also the case for PE in particular[24]. More precisely, we enforce this requirement by minimizing the second derivative in $F(\Lambda)$.

We have thus established two independent criteria in finding an appropriate distribution $F(\Lambda)$. First, we seek to minimize the error between the measured $\kappa(q)$ and those computed from Eqn. 4.9. Second, we seek to minimize the second derivative of $F(\Lambda)$, thus enforcing smoothness. At this point, we may simply optimize to find $F(\Lambda)$ such that the overall probability is highest. This has been done more commonly in the literature. However, in an effort to quantify the uncertainty in this process, we use Bayesian inference, which finds a distribution of possible $F(\Lambda)$ that are likely.

Bayesian inference relies on Bayes' Theorem, which is stated as:

$$P(A|B) = \frac{P(B|A)P(A)}{P(B)} \tag{4.12}$$

where B represents some measured data and A represents our hypothesis or the parameters we are searching for. $P(A|B)$ is the posterior distribution representing the likelihood of a given hypothesis A given the data B and is the quantity we are interested in quantifying. $P(B|A)$ is the probability of our data being represented by the proposed parameters and represents the likelihood function. $P(A)$ signifies our prior distribution and represents everything we know about our parameters before considering the data B. The final term, $P(B)$ is really just a normalization term and can be ignored, as we are only interested in the relative probability of the posterior.

Applying Bayes' theorem to our problem, A corresponds to $F(\Lambda)$, the unknown MFP distribution. B corresponds to the measured grating-dependent thermal conductivity values $\kappa(q)$. We re-write Bayes' theorem with these parameters for easy reference:

$$P_{post}(F|\kappa) \propto P_{like}(\kappa|F)P_{prior}(F) \tag{4.13}$$

We can first define $P(\kappa|F)$, or the likelihood, by utilizing the measured κ values along with their associated standard errors, given by standard deviations σ. The

significance of the measured κ and their errors is that they define a probability distribution for the true value of κ at the grating period of the measurement. Thus, for measurement i, at grating wavevector q_i, for measured thermal conductivity and error κ_i and σ_i, we may define the likelihood function as a normal distribution centered at the measured thermal conductivity:

$$P_i(\kappa_i|F) = \frac{1}{\sqrt{2\pi}\sigma_i} \exp\left(-\frac{\left(\kappa_i - \kappa(F, q_i)\right)^2}{2\sigma_i^2}\right) \tag{4.14}$$

where $\kappa(F, q_i)$ represents the thermal conductivity value that is computed for a given trial MFP distribution. To define the full likelihood function, we simply multiply all the probabilities together. However, this can be equivalently written as a sum over the arguments of the exponentials:

$$P(\kappa|F) \propto \exp\left(-\sum_i^N \frac{\left(\kappa_i - \kappa(F, q_i)\right)^2}{2\sigma_i^2}\right) \tag{4.15}$$

Next, we consider our prior distribution $P(F)$. So far, we have simply indicated that $F(\Lambda)$ should be smooth, but this constraint is not precise. Unfortunately, there is no rigorous procedure for defining this term a priori. However, we can define this in terms of a parameter that we may later tune. As previously stated, we wish to minimize the second derivative of $F(\Lambda)$. More specifically, we refer to the second derivative in terms of the log of Λ.[4] We shall use $\Omega = \log_{10}(\Lambda)$. To build our prior distribution, we define a probability distribution for the second derivative of a segment of $F(\Lambda)$. We use a normal distribution centered at 0 (which corresponds to perfect smoothness). To mathematically represent this normal distribution, we first consider the second derivative of $F(\Lambda)$ at some MFP Λ_j:

$$W_j = \left.\frac{\partial^2 F}{\partial \Omega^2}\right|_{\Lambda_j} \tag{4.16}$$

$$P_j(F) \propto \exp\left(-\frac{W_j^2 \Delta\Omega}{2\gamma^2}\right) \tag{4.17}$$

where we have defined γ to be a parameter representing how far from 0 the second derivatives are likely to deviate. Note we have also added the term $\Delta\Omega$ to quantify how much of the chain segment is being considered. This scales the penalty

---

[4]We mentioned earlier that the smoothness criteria is in part based on previous works, including that of PE. These works typically use a log scale in terms of MFP, suggesting that the function remains smooth only on that scale.

with the amount of the curve that has a high curvature. To build the total prior probability distribution, we must multiply all $P_j(F)$ terms together. Again, this can be represented as a sum over the arguments of the exponentials.

$$P(F) \propto \exp\left(-\frac{1}{2\gamma^2} \sum_j^M W_j^2 \Delta\Omega\right) \tag{4.18}$$

We note here that in the appropriate limit, the sum can be rewritten as an integral. This requires the discretization in the MFPs to be fine enough, and for W to go to 0 at the ends.

$$P(F) \propto \exp\left(-\frac{1}{2\gamma^2} \int_{-\infty}^{\infty} W_j^2 d\Omega\right) \tag{4.19}$$

As a result, as long as a chosen discretization of the MFPs correctly approximates this integral, the specific choice does not matter, and repeated use of this expression with different limits, quadrature, etc. will lead to the same results. It is important to design the condition this way for reproducing and comparing results.

4.8 Bayesian Inference: Algorithm and Implementation

We now consider the implementation of Bayesian inference, now that all the components of Bayes' theorem are defined. Our goal is to find a distribution of $F(\Lambda)$ with the highest likelihood. The first step we address involves the discretization and calculation details in evaluating $P(\kappa|F)$ and $P(F)$ from Eqns. 4.15 and 4.18, respectively.

Starting with $P(\kappa|F)$, we have a given set of N experimental data points defined by q_i, κ_i, and σ_i. We need only calculate $\kappa(F, q_i)$. To do this, we discretize the MFP spectrum into M parameters Λ_j. For all of our results, we use $M = 61$ and span the range from 1 nm to 1 μm. This range is found to be large enough to incorporate all contributing MFPs to the thermal conductivity. Further, the density of points is high enough to capture the finer details of the profiles. The points in between the bounds are distributed uniformly in log space. To compute $\kappa(F, q_i)$ from $F(\Lambda)$, we use Eqn. 4.9, though because we discretize in log space, corresponding to $\Omega = \log_{10}(\Lambda)$, we rewrite the integral:

$$\kappa(q) = \int_{-\infty}^{\infty} qF(\Lambda)K(x)\Lambda d\Omega \tag{4.20}$$

which differs only in the extra factor of Λ and the modified integration limits. Next, we are able to convert to a summation, which is made simple by our uniform

discretization.

$$\kappa(F, q_i) = \sum_{j}^{M} q F(\Lambda_j) K(x_{i,j}) \Lambda_j \Delta\Omega \qquad (4.21)$$

$$\kappa(F, q_i) = \sum_{j}^{M} A_{i,j} F(\Lambda_j) \qquad (4.22)$$

where we have written the RHS in terms of a matrix A and the unknown $F(\Lambda)$.

Next we consider evaluating $P(F)$, which requires the computation of second derivatives W according to Eqn. 4.16. We calculate the discrete second derivative at each point as follows:

$$W_j = \frac{1}{2}\big(2F(\Lambda_j) - F(\Lambda_{j+1}) - F(\Lambda_{j-1})\big) \qquad (4.23)$$

$$W = LF \qquad (4.24)$$

where we have defined a matrix L with dimensions $(M - 2)$ by M to represent the system of equations for each W_j. Following the computation of W, $P(F)$ may be calculated according to Eqn. 4.18.

Metropolis-Hastings Markov chain Monte Carlo Algorithm

To perform Bayesian inference, we must choose some algorithm to estimate the posterior distribution. In this work, we use the Metropolis-Hastings (MH) Markov chain Monte Carlo (MCMC) algorithm[97, 98]. The idea behind a generic MCMC is to move around parameter space, sampling various proposed parameters (F). The posterior probability distribution is then constructed as the algorithm explores parameter space.

The MH algorithm in particular implements a random walk around parameter space. Subsequent steps are chosen according to a proposal distribution, $K(F|F_{prev})$, which is a distribution of possible next steps (F) from the walker's current position (F_{prev}). Each step is then independently accepted or rejected according to the relative posterior probability at the new point. This allows the walker to spend more time in regions of high probability density, equating the time it spends in a region to the magnitude of the overall posterior density there. We lay out the specific steps of the algorithm as follows:

Algorithm 1 Metropolis-Hastings Markov chain Monte Carlo

1: Choose an initial F_0 ▷ vector length M
2: **for** $i = 1, ..., N$ **do**
3:      Choose new sample F_i from $K(F|F_{i-1})$ ▷ Sample proposal distribution
4:      Evaluate $\pi(F_i) = P_{like}(\kappa|F_i) \times P_{prior}(F_i)$ ▷ Evaluate posterior probability
5:      Compute the acceptance probability

$$\alpha(F_i, F_{i-1}) = \mathbf{min}\left[1, \frac{\pi(F_i)}{\pi(F_{i-1})} \right]$$

6:      Accept F_i with a probability equal to α. If rejected, set $F_i = F_{i-1}$
7: **end for**

Following all N steps, we will have N sets of F, where F consists of M parameters. Thus for each parameter, F_j, there is a distribution composed of N samples. The frequency of any value, or similarly the density of samples in a particular range of values, makes the posterior probability distribution for F_j. Also note, as a point of clarification, that when a point is rejected in the algorithm, the previous point, which is reused, then counts twice (or more if multiple points are rejected in a row). Thus if the set of parameters at one step corresponds to a high probability, and many of the neighboring points in parameter space are less likely, many steps after may be rejected. This results in an even larger weight being attributed to the current position, reflecting the point's high posterior probability.

Another important note is that depending on the initial set of parameters used, F_0, the random walker may not be starting in a relevant region of parameter space. The region of parameter space characterized by higher probability density, which ideally where the random walker would spend the most time, is known as the typical set. Because F_0 is likely not in the typical set, it is common to implement a "burn in" or warm-up period where the walker is allowed to run for a number of steps without saving its history. Because a single step is not computationally expensive in our case, we use a conservative 1×10^5 steps for warm-up. For the actual sampling step where every F_i is saved along the way, we use 1×10^8 steps for all results presented. This is found to be more than enough time to reach a converged posterior distribution.

While the MH-MCMC algorithm is relatively simple, the choice of a proposal distribution K is non-trivial. There are many options for K, however certain choices can result in dramatically more efficient simulations. For example, a uniformly distributed kernel that chooses random parameters on every iteration would be

inefficient, frequently spending time in regions of parameter space that are irrelevant. This problem is exacerbated as the dimensionality of parameter space increases. A straightforward choice for K is to randomly move from the current position according to a normal distribution. Thus any individual element of F may rise or fall independently, while tending to only change a small amount in any single step. The standard deviation of the distribution may be tuned to limit the walker's movement in any given step. Note that a large deviational parameter will approach the uniform distribution, which would explore the space inefficiently. On the other hand, a small deviational parameter would not be able to explore the space fully in a reasonable amount of steps because its movement is too restricted. The value must be tuned appropriately.

In our case, we have the added complication that there are numerous constraints on the elements of F that must be considered. The first constraint is that F must always be positive. The second, far more restrictive constraint, is that F must be monotonic. As it is a cumulative distribution function, it must never decrease. To more easily satisfy these restrictions, we reparametrize F and instead use f, the differential MFP distribution. This still leaves us with the constraint that each element f_j must be positive. Next, we consider instead $g_j = log(f_j)$. Now, g_j may be any real value, and f_j will be positive. Thus, we have no more constraints to consider.

As a brief aside, we must note that the exact parameterization used implicitly assigns a prior distribution to the possible parameter values we are seeking. The reason for this is that as we explore parameter space, we are effectively trying to integrate over the posterior probability distribution. This is affected in part by which regions have the highest magnitude probability. Just as important, however, is the density of the space being explored. For example, a large region of moderate probability may be as influential as a narrow region of high probability. By switching to log space, we are placing a higher density on lower magnitude parameter values compared to when in linear space. Values between 0.01 and 0.1 are just as likely as values between 1 and 10. We believe that this choice is actually preferable, as many parameters f_j at very low and very high MFPs are likely to be 0. It makes much more sense for them to vary around near-zero values rather than frequently foray into excessively high values that are unrealistic.

We now consider potential proposal distributions $K(g|g_{i-1})$. Due to our lack of constraints, we may now adopt a normally distributed proposal distribution as previously mentioned, which has a straightforward implementation. For each parameter,

we sample Δg from a normal distribution:

$$K(\Delta g_j) = \frac{1}{\sqrt{2\pi}\sigma} \exp\left(-\frac{\Delta g_j^2}{2\sigma^2}\right) \tag{4.25}$$

While this kernel is perfectly valid, we make one more modification to more effectively search the parameter space. Because we are imposing a prior probability distribution favoring smoothness in F, this translates to adjacent values of f having a small slope, or being close to the value of their neighboring points. Because our current kernel changes each point fully independently, it is likely that a random step would experience a great penalty due to the prior. To avoid this, we make the individual Δg_j steps dependent on their neighbors. We accomplish this by first drawing $\Delta g_j'$ according to Eqn. 4.25. Following this, each sampled deviational term is spread out and added to neighboring points as follows:

$$\Delta g_j = \sum_{j'}^{M} \Delta g_{j'}' \exp\left(-\frac{((j - j')\Delta\Omega)^2}{2\sigma_s^2}\right) \tag{4.26}$$

where as a reminder, $\Delta\Omega$ is the difference between adjacent discretized MFP points in log space. Here, we effectively draw random deviational terms for each j point. Then we spread these terms out according to a normal distribution to nearby points. This ensures that any step by the walker will maintain some amount of local smoothness. Note, this is effectively equivalent to building a non-diagonal covariance matrix and applying it in Eqn. 4.25 when drawing Δg_j. Regardless, these choices for the proposal distribution ensure that the random walker in our algorithm is able to both effectively explore the parameter space while preferentially choosing new steps that are more likely to be accepted.[5]

Finally, we point out that our proposal distribution satisfies a critical condition of the MH-MCMC algorithm. To accurately build the posterior distribution, the proposal distribution must have an equal probability of stepping from point A to B as from stepping from B to A. Thus, it must be symmetric. The acceptance/rejection step will account for the posterior distribution. Any bias in the chosen distribution will bias the final results and lead to an inaccurate posterior. We note that our choice of proposal distribution does satisfy this because the drawn Δ_g values are symmetric about 0, and that their magnitude does not depend on the value of g.

---

[5]If this is still unclear, it is equivalent to biasing a random walker trying to cross a bridge to preferentially move forward and backwards rather than a random direction. It is still capable of exploring the entire bridge, however it will be much faster if it covers more ground forward and backwards.

With the algorithm fully established, we note that we have several parameters that must be chosen. With regards to the proposal distribution, we have σ, which acts similar to a temperature. The larger it is, the further the random walker can jump from step to step. We also have σ_s, which acts as a spreading factor that helps ensure smoothness in each step. When this is near 0, it does nothing. When it is large, it causes a degeneracy that removes any independence in the changing parameters. Then it is impossible to explore the parameter space. However, for most choices of these values, the algorithm should converge accurately, just with varying amounts of computational efficiency. For results presented in this thesis, we choose $\sigma = 0.005$ and $\sigma_s = 0.2$. Overall, we aimed for an acceptance ratio in the algorithm of approximately 40% in an effort to balance exploring the full space while not jumping too far in any single step.

The only other parameter we must choose is γ in the prior distribution of Eqn. 4.18. For $\gamma = 0$, this would impose a δ-function prior probability that $F(\Lambda)$ is a line (perfectly smooth). Alternatively, As $\gamma \rightarrow \infty$, the distribution becomes uniformly dense, imposing no smoothness criteria at all. In practice, choosing a value for γ is nontrivial. In this work, we have no a priori method for assigning it a value. As a result, we will consider a range of γ values, spanning from close to 0, where a straight line is favored, to large values, where the prior only weakly influences $F(\Lambda)$. While this significantly expands the uncertainty in the final results, we are still able to draw conclusions. Specifically in this work, we vary γ between 0.1 and 10, spaced evenly in log space. This range was found empirically to cover a majority of reasonable and distinct γ values.

4.9 MFP Reconstruction of PE Films

We apply the MH-MCMC algorithm as laid out in the previous sections to the grating-dependent thermal conductivity data presented in Section 4.5. Beginning with Figure 4.6(a), we show the reconstructed MFP spectra for 3 different PE films of varying draw ratios, corresponding to data presented in Figure 4.6. This plot shows the posterior probability distribution calculated from Bayesian inference. For any given MFP Λ, the darker regions have a higher probability density. The solid lines show the mean distribution for a given $F(\Lambda)$, while the 2 corresponding dotted lines encapsulate the 95% credible interval[6]. This interval encloses the highest likelihood solution for $F(\Lambda)$.

---

[6]Specifically, we include the central 95% of the distribution.
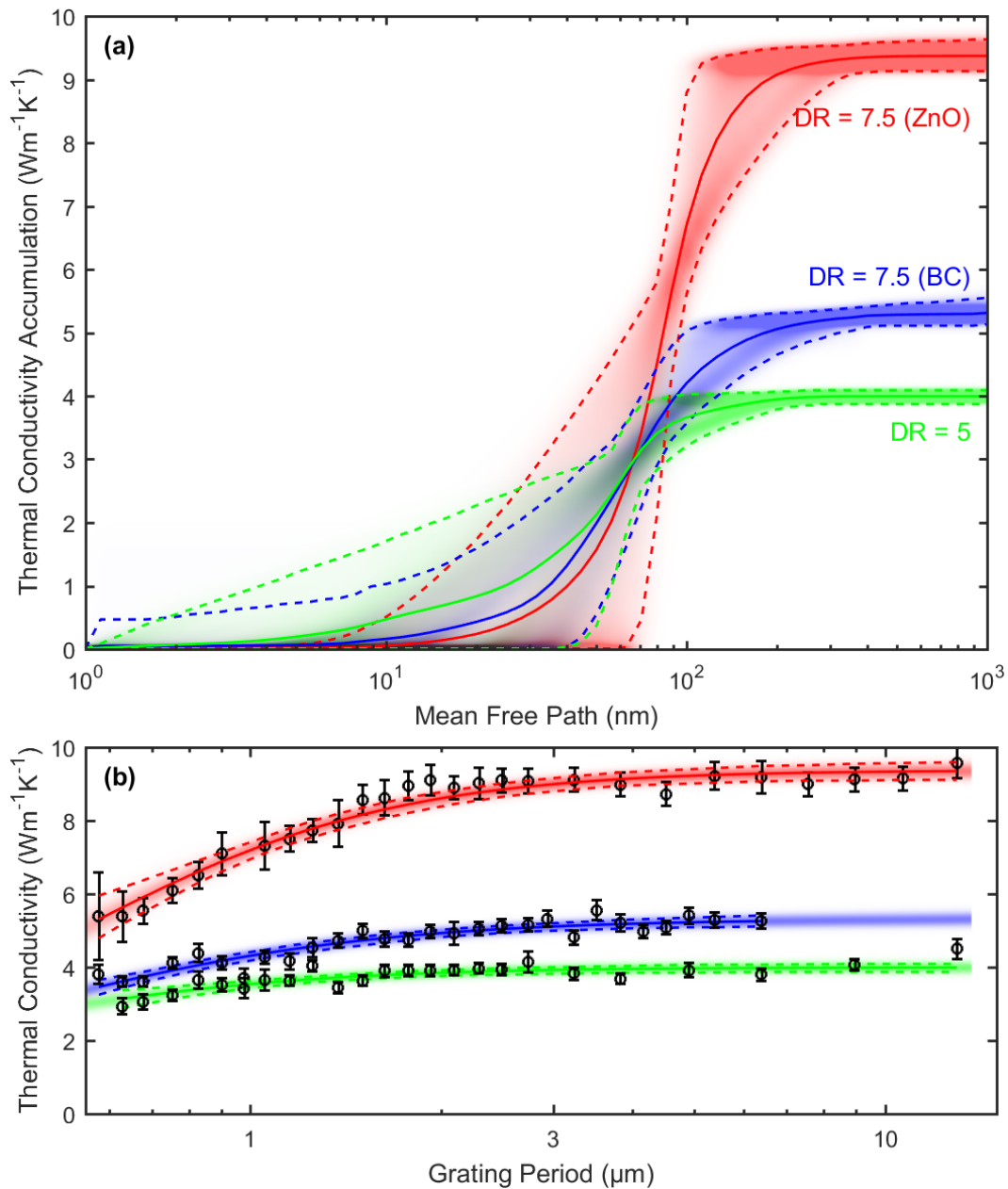
Figure 4.6: (a) Posterior probability density for reconstructed MFP spectra for (green) ZnO5, (blue) BC7.5, and (red) ZnO7.5. The solid lines correspond to the mean spectrum and the dotted lines enclose the 95% credible interval. (b) The corresponding grating-dependent thermal conductivities overlaid with the calculated thermal conductivities from the spectra in (a). The error bars refer to the 68% confidence intervals.

This plot shows data for ZnO5, BC7.5, and ZnO7.5, in green, blue, and red, respectively. We remind the reader that the nominal draw ratio is subject to variability and that each sample is best evaluated based on the maximum thermal conductivity value. As a result, the 3 samples shown in this plot represent a series of increasing draw ratio and how the MFP spectrum evolves with draw ratio.

For reference, Figure 4.6(b) shows the grating-dependent thermal conductivity data as previously shown, and overlays them with the calculated thermal conductivities corresponding to the posterior distributions for $F(\Lambda)$ from Figure 4.6(a). The solid and dotted lines have the same meanings as well. We can see from this plot that the calculated κ values from the reconstruction are in good agreement with the data, giving us confidence in our reconstruction.

Looking closer at the reconstructed MFP spectra in Figure 4.6, we first draw attention to ZnO5 shown in green. First, regardless of the uncertainty, there is a clear and significant contribution to thermal conductivity from MFPs in the range of 10 nm to 100 nm. Considering the mean distribution for $F(\Lambda)$, approximately 30% of the thermal conductivity contribution appears to come from phonons with MFP above 60 nm. The uncertainty may vary this proportion, though we will use the mean distribution as a standard way to compare different samples.

Looking to the spectrum at lower MFPs, we see that the uncertainty grows substantially. The reason for this corresponds to the lowest grating period used in the measurements. As previously discussed, the lowest grating period being used in any measurement is 577 nm. Recalling the suppression function from Eqn. 4.11, we can calculate that a phonon with a MFP of 50 nm would experience a suppression of approximately 23%. At 30 nm, the suppression is only 10%. Roughly speaking, the sensitivity to MFP suppression in this range starts to become too small to obtain much certainty about the spectrum. Furthermore, only a small portion of the measured data showed a significant suppression in κ. While our data for this sample is enough to confidently establish an approximate upper bound to the contributing phonon MFPs, it is unable to quantitatively yield much below that. However, despite this, we are still able to find strong evidence that phonons with MFPs of at least 80 nm are present in this sample.

We next move to BC7.5, which shows a similar range of contributing MFPs compared to ZnO5. Here, ~30% of the thermal conductivity contribution appears to come from phonons with MFP above 85 nm. Furthermore, there is clear evidence for significant contributions up to 100 nm, regardless of the uncertainty in the reconstruction.

Finally, we compare to ZnO7.5, the most conductive film we consider. For this sample, ~30% of the thermal conductivity contribution likely comes from phonons with MFP above 95 nm. Phonons with MFPs well above 100 nm seem to be contributing significantly to κ.

Overall, with increasing draw ratio, we see a clear increase in contributions from higher MFP phonons. While there is a significant amount of uncertainty in the reconstruction, we are still able to obtain a relatively narrow distribution in $F(\Lambda)$ at higher MFP values in each spectrum. The reason for this is that the onset of the suppression in κ has a strong influence on where the upper cutoff in MFP can occur in $F(\Lambda)$. It is this region that has the highest sensitivity to the data. Thus, we can confidently say that as draw ratio is increased, relatively long phonon MFPs above 100 nm, become significant in these PE films.

We next show identical MFP reconstruction calculations at a lower temperature. Figure 4.7 shows the reconstructed spectrum for ZnO7.5 at 100 K. The spectrum at room temperature is shown again (identical to Figure 4.6) for easy comparison. This measurement reveals the temperature dependence of the MFP spectrum.

Overall, the spectra are very similar. The maximum κ is smaller at 100 K due to the lower heat capacity, however there still appear to be significant contributions to κ well above 100 nm. At this temperature, ~30% of the thermal conductivity comes from MFPs above 90 nm. In general, one might expect MFPs to get longer at a reduced temperature, due to decreased phonon-phonon scattering, however that does not appear to be the case at all here. This is direct evidence for structural scattering being the dominant scattering mechanism in the film, because it would not be temperature-dependent.

In summary, we have established the MFP spectra for numerous PE films with varying draw ratios and found that they all have phonon MFPs on the order of 100 nm. The effect was repeatedly demonstrated on different films, at different temperatures, and with different fillers used in the films. To better understand and interpret these results, we first consider other measurements that may help understand the microstructure of the films as well as how it relates to thermal transport.

4.10   Temperature-Dependent Thermal Conductivity

Having shown grating-dependent thermal conductivity for PE films at low temperatures already, we now consider the full temperature dependence for a variety of PE
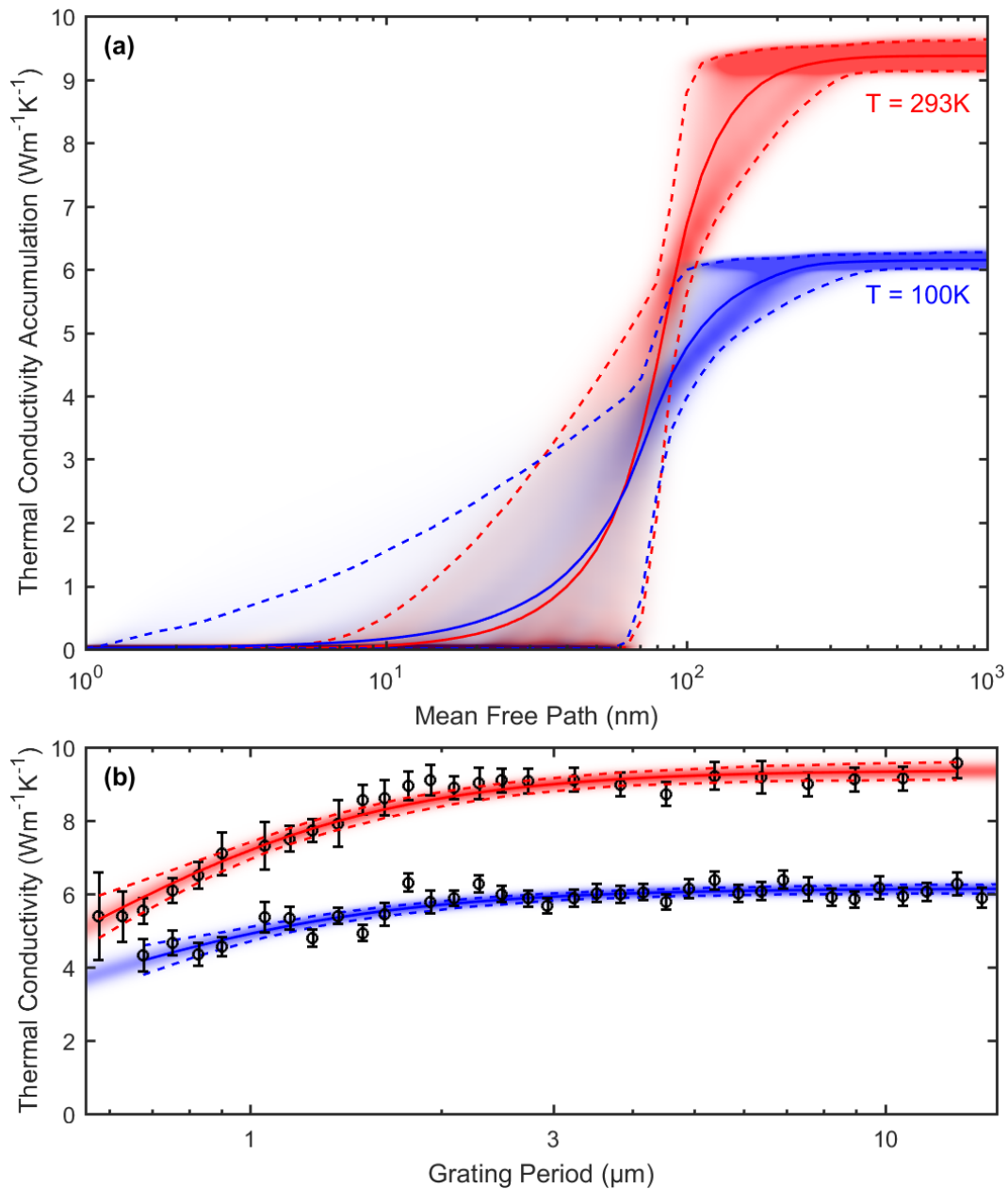
Figure 4.7: (a) Posterior probability density for reconstructed MFP spectra for ZnO7.5 at (red) room temperature and (blue) 100 K. The solid lines correspond to the mean spectrum and the dotted lines enclose the 95% credible interval. (b) The corresponding grating-dependent thermal conductivities overlaid with the calculated thermal conductivities from the spectra in (a). The error bars refer to the 68% confidence intervals.

films to further investigate the scattering mechanisms dominating thermal transport.

Figure 4.8 shows temperature-dependent κ for 4 films, ranging in draw ratio from 2.5 to 196. Considering the lower draw ratios, ranging from 2.5 to 7.5, we see two defining features of the temperature dependence. First, κ is steadily increasing as a function of temperature. For high quality crystals, one would expect a decreasing trend, indicative of phonon-phonon scattering. At higher temperatures, the increased phonon population leads to excess scattering that lowers MFPs. However, in these samples that is not the case, and κ is able to rise due to the increase heat capacity. This is direct evidence for the prevalence of structural scattering, which is not surprising in these films.

The second observation we can make is concerned with the hump near 200 K, where κ drops relative to surrounding temperatures. While this feature is not fully understood, it overlaps with the glass transition temperature for PE[99, 100] and likely has to do with the transition occurring in the amorphous regions of the film. Regardless, it does not affect the overall trend of the data.

At the highest draw ratio of 196, we see that we have an increased κ with temperature up to a point, but that it appears to reverse at high enough temperatures, where presumably, phonon-phonon scattering begins to dominate. By comparing this to the lower thermal conductivity, lower draw ratio samples, we can clearly see how the relative importance of different scattering mechanisms changes at different draw ratios.

Overall, while we may already expect that structural scattering dominates in partially drawn, highly imperfect films, the temperature-dependent measurements provide further evidence. Having explored the direct relationship between κ and T, we next move on to direct characterization methods of the microstructure in these PE films.

4.11   Structural results

While we were able to directly study the length scales of heat carriers in PE films using MFP spectroscopy, if we pair that with independent characterization of the films' microstructure, we can relate how structural properties directly affect and limit thermal transport.

Scanning Electron Microscopy

First, we show Scanning Electron Microscope (SEM) images of two PE films in Figure 4.9. While we do not extract any quantitative information from this plot, it
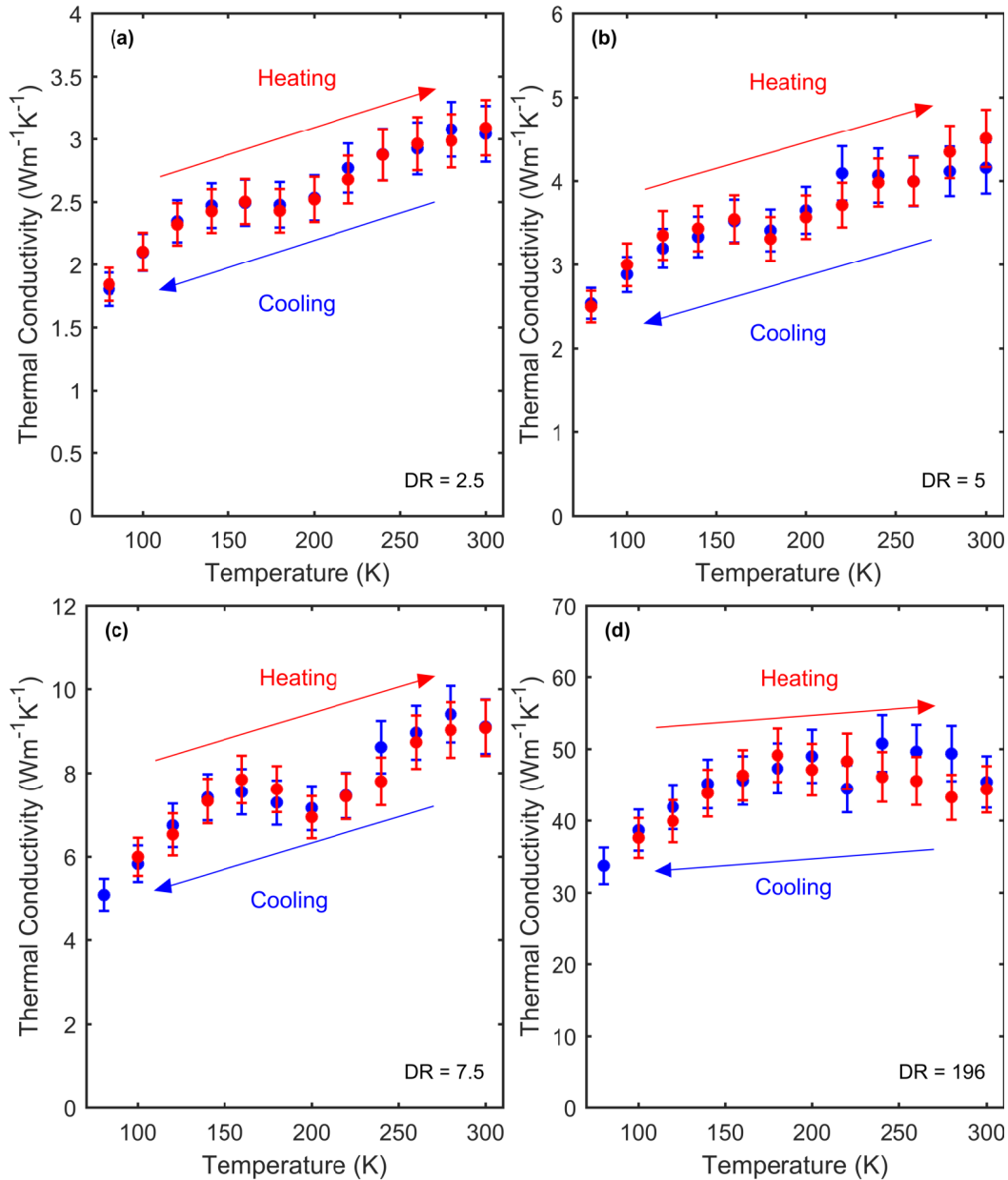
Figure 4.8: Temperature-dependent thermal conductivity for (a) BC2.5, (b) ZnO5, (c) ZnO7.5 film, and (d) Au196 film. At lower draw ratios, κ increased with temperature, indicating that phonon-phonon scattering is not dominant. This suggests structural scattering must dominate. At the highest draw ratio, this trend does appear to level out and potentially start decreasing, suggesting phonon-phonon scattering becomes more important. The bump visible near 200 K in multiple profiles is likely caused by the glass-transition in PE.
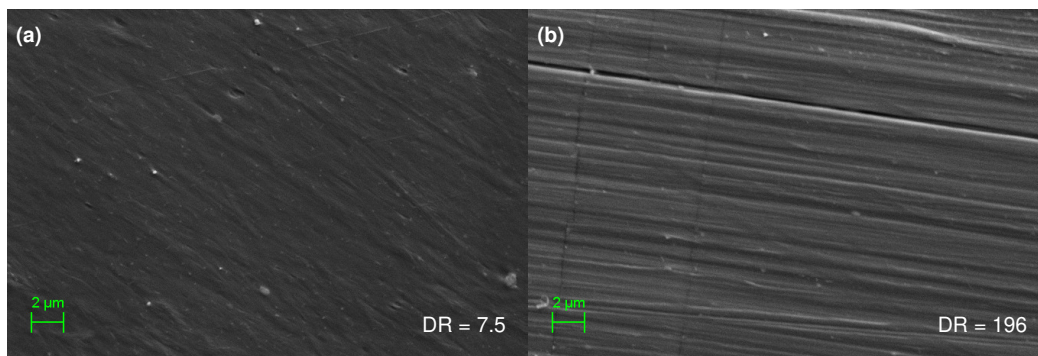
Figure 4.9: Scanning Electron Microscope image of (a) ZnO7.5 and (b) Au196. While the orientation in (a) is visible, its chains are not fully oriented. (b) shows clear fibers on the surface of the film that are fully oriented over long length scales of 10's of μm's.

provides a physical picture for the structure of the PE films that may be useful for the reader. While SEM images only provide information on the topological features on the films, we assume it is representative of the internal microstructure. In Figure 4.9(a), for ZnO7.5, one can see that the film has a preferential orientation, however it is clearly only partially oriented. In contrast, Figure 4.9(b) shows that for an ultra-drawn PE film, there are clear fibers with near perfect orientation. Further, the fibers appear to extend on the order of 10's of μm's.

Small-Angle X-ray Scattering

Moving on to a quantitative evaluation of the microstructure, we use Small-Angle X-ray Scattering (SAXS) measurements on several films. All experiments and analysis were performed by our collaborators at Loughborough University who fabricated the films. Also note that different films were used in the SAXS measurements compared to all other results presented in this work. However the PE and fillers used were all from the same batch, and thus can be expected to have similar internal structures.

Figure 4.10(a) shows raw SAXS results for a ZnO NP-doped PE film with a draw ratio of 7.5. There are clearly visible peaks on either side of the central beam that correspond to the lamellar spacing along the oriented direction. Figure 4.10(b) shows the Lorentz-corrected intensity for 3 SAXS measurements for films ranging in draw ratio from 2.5 to 7.5. The peaks clearly show the presence of regular lamellar spacing. All 3 films show spacing in the range of 40 nm to 50 nm, steadily increasing with draw ratio.
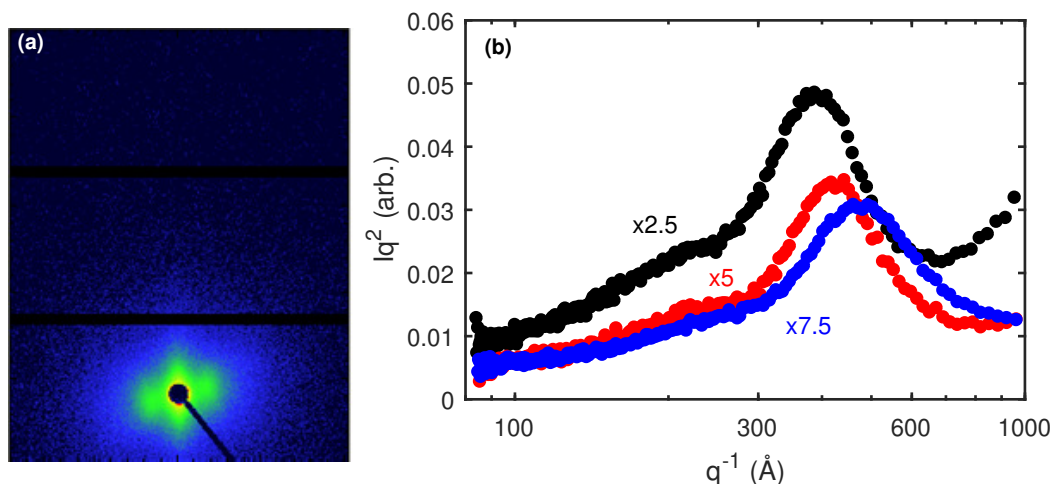
Figure 4.10: Small-Angle X-ray Scattering of ZnO NP-doped PE films at draw ratios from 2.5 to 7.5. (a) shows raw data for the $DR = 7.5$ PE film, with peaks outside the central peak visible. (b) shows the Lorentz-corrected intensity plotted on a log scale. The peaks correspond to the lamellar spacing along the oriented direction in the PE films. The sizes range from 40 nm to 50 nm. This will roughly correspond to the crystalline domain sizes.

We are most interested in estimating the crystalline domain size in the film. Wide-Angle X-ray Scattering (WAXS) measurements were also conducted which estimated the crystallinity for these films to be in the range of 70-80%. As a result, regardless of the exact arrangement of crystalline and amorphous regions within the film, the crystalline domain sizes are likely in the range of 30 nm to 50 nm.

Furthermore, there is clearly a distribution of lamellar sizes based on the variable peak widths. There are numerous factors that can modulate the peak width, so we are unable to quantitatively establish a size distribution. However, to establish a very approximate estimate, we are able to fit the distribution of the $DR = 7.5$ film very well with a log-normal profile with a standard deviation of ~10 nm. The other draw ratio samples' distributions are a bit narrower. As a result, it is feasible that the films have crystalline domain sizes as high as ~60 nm.

4.12 Discussion

Having presented measurements of both physical and thermal length scales, we can now construct a more complete picture of thermal transport in these oriented PE films, especially as it relates to scattering and the microstructure.

Considering ZnO7.5, the chains are mostly oriented, though not fully, with crys-

tal domain sizes along the oriented direction on the order of 50 nm. From the temperature-dependent measurements, the dominant scattering mechanism is clearly structural scattering. The reconstructed MFP spectrum for this film however places a significant portion of the phonon MFPs above 95 nm, notably higher than even the largest estimate of crystal domain size. It is important to note that longer MFP phonons will be over-represented in the thermal conductivity accumulation function because they intrinsically carry more heat and thus are weighted higher. However, it is clear that a large portion of the phonons in the material have MFPs at or exceeding the average crystal size.

Our first conclusion we may draw from these findings is that the crystal size is the primary limiting factor with regards to scattering in these PE films. While it was already clear that intrinsic phonon-phonon scattering was not dominant, this observation also rules out defect scattering as a dominant mechanism. Thus, the PE crystalline domains that are present are able to transmit phonons without significant scattering caused by defects or other means, and it is the domain boundaries related to the semi-crystalline microstructure that are most limiting.

Our second conclusion is that while a large portion of phonons are scattered at domain boundaries, a significant portion do appear to transmit and extend over ~2 domain lengths. This suggests that the amorphous regions in between these domains are able to transmit phonons. The amorphous regions in oriented polymers have long been poorly understood with regards to thermal transport. Like the crystalline domains, amorphous regions are similarly oriented from the drawing process, so heat transport can still travel primarily over the chain backbones. As a result, it is feasible that some phonon modes that do not exist in an unoriented amorphous structure might be supported in the drawn amorphous structure. As mentioned in Chapter 1, there is evidence that these regions do experience a dramatic increase in thermal conductivity, albeit smaller than the crystalline domain, so this picture has some support. While our data and characterization does not separate out contributions from crystalline vs amorphous regions, the relative phonon MFPs compared to the crystal domain size offer strong support that the structure of amorphous regions play a key role in the thermal transport, intimately tied to that in the crystalline domains.

Not only are these results enlightening with regards to thermal transport at the microscale, but they may be extremely useful in fabricating PE films with even higher thermal conductivity. Because the crystal domain size appears to be the dominating factor limiting the phonon MFP, enlarging it during fabrication of PE

should have one of the largest benefits to κ. While the overall crystallinity has always been known to strongly influence κ, these results suggest that for a constant crystallinity, larger grains should significantly benefit heat transport. Crystal domain sizes higher than those studied here have already been reported in different studies, as previously mentioned. Thus by tuning the fabrication, it is possible to improve the grain size. Our results point to the fact that this property should receive far more attention in future studies.

A secondary conclusion with narrower applicability has to do with potential applications of PE and potentially other polymer thermal conductors. Due to the high thermal conductivity relying so heavily on large MFPs, any application utilizing nano or microscale polymers (in the chain direction) should expect the effective thermal conductivity to decrease. For example, the polymer brush structure discussed in Chapter 2, which can produce highly ordered polymer chains, would likely suffer from this quasi-ballistic effect for highly conducting polymers, unless the brush is sufficiently long. While we are unaware of any such applications with these polymers now, these materials have long been proposed as heat spreaders in micro-electronics and other nanoscale devices. Our results should be considered when evaluating the true benefit of polymers in such applications.

In conclusion, we have used TG as a MFP spectroscopy tool to estimate the phonon MFP spectrum in a series of oriented PE films. Furthermore, we have characterized the anisotropic transport in these films, their temperature dependence, and the length-scale of the crystalline domains within the semi-crystalline structure. These results provide a novel view into thermal transport at the microscale and may prove to be valuable feedback for the fabrication of even more conductive PE films in the future.

C h a p t e r 5

SUMMARY AND OUTLOOK

In this thesis, we have explored the limits of thermal conductivity through simulations and experiments for semi-crystalline and crystalline polymers. We have built on decades of research that established the potential for high thermal conductivity in various polymers through computational and experimental studies. Our work has provided a new experimental perspective of the microscopic transport processes in oriented polymers and identified strategies to realize molecular solids with exceptional thermal transport properties.

In Chapter 2, we explained how Molecular Dynamics (MD) simulations are used to study thermal transport in materials. Then, polynorbornene (PNb) was introduced as a potential thermal conductor, based on the conclusions and guidelines laid out by previous literature. Through the use of MD and a variety of data analysis tools, we showed that not only does crystalline PNb have a low thermal conductivity, but it conducts heat as a phonon glass, in a fundamentally different way compared to all other polymer crystals that have been studied. This result highlights the lack of a detailed understanding of the molecular factors that lead to high thermal conductivity. However the finding extends and makes known an alternative heat conduction scheme that may occur in numerous other polymer crystals.

In Chapter 3, we introduced the Transient Grating (TG) technique and described the unique advantages the method has when it comes to measuring heat transport in polymer films. We laid out the specific challenges faced when measuring polymers, including oriented films, as was the focus of Chapter 4. Our setup required numerous modifications and developments not only to enable the measurement of these films, but also to maximize the accuracy and efficiency of the process. Numerous measurements and results were presented to verify the functionality of TG. Finally, we presented the thermal models necessary for data analysis, including the solution for the thin film geometry, which is necessary for polymer thin films that rely on a substrate for fabrication.

Finally in Chapter 4, we presented measurements of quasi-ballistic heat transport measurements in polyethylene (PE), the first of any polymer. First, TG was successfully applied to PE, measuring the full anisotropic in-plane thermal conductivity.

Next, TG was applied with sub-µm grating periods to obtain grating-dependent thermal conductivity in a variety of samples. To reconstruct the phonon mean free path (MFP) spectra of these films, a Bayesian inference algorithm was presented and applied to establish a probability distribution for the spectrum of any material. Through this analysis, we found that even in partially oriented, semi-crystalline PE, MFPs on the order of 100 nm contributed significantly to thermal conductivity. Through the use of Small-Angle X-ray Scattering (SAXS) measurements, we were able to establish that the average crystal domain size was even smaller, demonstrating that domain boundary scattering is the limiting factor in achieving high thermal conductivity in PE films.

Overall, we have challenged the fundamental lower limits of thermal transport in polymer crystals, extended the experimental capability to measure phonon length scales in real polymers, and provided direct evidence for the intimate relationship between phonon MFPs and the microstructure in PE. Next, we consider how these results may affect and inspire future areas of study.

5.1 Future Work

For the field of thermal transport in polymers, there remain a number of open questions that call for continued computational and experimental work. In general, many of these questions center on the bridging of computational studies, which typically focus on ideal structures, to the real materials that are feasible to study with experiments.

One of the key takeaways from our MD work with PNb dealt with the failure of conventional criteria for high thermal conductivity previously established in the literature. Specifically, this discrepancy arose from a low thermal conductivity arising in PNb despite the presence of light atoms, strong bonds, and an ordered structure. A potential direction for immediate future study would further probe the Ioffe-Regel crossover, where this phonon glass behavior begins. What molecular features truly cause this effect, and are there a set of materials that exhibit the phenomenon to a lesser extent? It is possible that the cutoff frequency is higher in other materials, or that a more gradual transition is observed in frequency space between diffusons and propagons. Then, further understanding here may build on and complete the guidelines previously presented in the literature.

On the experimental size, TG can always be improved. In the interest of probing smaller and smaller length scales, TG systems that work at shorter wavelengths

would enable this. For example, the use of a UV laser would allow grating periods as low as half that of those used in this thesis, which would greatly extend experimental capabilities. While PE is intrinsically capable of MFPs long enough to be measured by our current experiment, many other polymers that may be studied would not have this benefit. Developing a system capable of pushing the lower limits even further would open up the field to study a much wider set of materials.

With regards to PE specifically, our work provides strong evidence for the dominant scattering mechanisms. These results may prove valuable inspiration for the best ways to improve thermal conductivity moving forward. Previous work has already established the ability to make PE with larger crystal domain sizes. Our work suggests this be a priority in sample fabrication and processing, potentially enabling dramatically improved transport for the same level of sample drawing and post-processing.

Because TG is able to probe the MFP spectra, especially in PE, future studies that systematically study a wide variety of fabrication or other processing steps in conjunction with TG spectroscopy would be especially valuable. Numerous other characterization tools are routinely used as a feedback mechanism as fabrication processes are developed. While TG is more complex than the typical thermal characterization methods, its use as an additional characterization tool would provide a more direct window to the interplay between thermal properties and microstructure, for PE and other materials.

Additionally, PE and other polymers may also be studied under a wider set of experimental conditions. Specifically, while we only went down to temperatures of 80 K, PE and other polymers can be studied down to liquid Helium temperatures ($\sim$4 K). In cases where phonon-phonon scattering plays a more critical role, the MFP spectrum may vary at these lower temperatures. Conversely, while we did not exceed room temperature in our measurements, PE and other polymers can be investigated at higher temperatures where phonon-phonon scattering would become increasingly more dominant. While high temperatures would be limited by sample stability, the MFP spectrum at elevated temperatures would not only directly measure temperature stability of thermal transport, it would show the varying temperature dependence of different MFP phonons.

The MFP spectroscopy in this thesis was also limited to draw ratios of 7.5 and lower due to poor sample quality. While this thesis did not focus on sample fabrication, further work into improving the optical properties of highly drawn polymer samples

would enable TG MFP spectroscopy to be applied to highly oriented PE films with bulk thermal conductivities exceeding 40 $\text{Wm}^{-1}\text{K}^{-1}$. These samples would likely have MFPs even longer than samples investigated in this thesis, though without these improvements in fabrication, we can only speculate.

Finally, one general area of focus for the future that we have previously eluded to relies on bridging computational work to experiments. For example, simulation studies on amorphous or semi-crystalline structures would be extremely interesting and valuable. Results from experiments and simulations on polymers can seldom be compared directly, but simulations of realistic structures could change that. Furthermore, simulations of structures like the PE samples presented in this thesis could help verify and better explain our experimental observations. In particular, while we presented evidence that some phonons are able to traverse beyond the crystal domains for an even longer MFP, the role of the oriented amorphous region in this process is left to speculation. Computational studies that replicate our experimental findings would provide a window into the finer details we are still unable to see experimentally.

In summary, we have described a sampling of potential future directions inspired by our work. Better fundamental understanding of heat transport in polymers may eventually enable the engineering of polymers in heat spreading applications, effectively creating a brand new class of functional materials. We hope this thesis has been a useful resource for computational and experimental studies of heat transport in semi-crystalline and crystalline polymers, as well as experimental methods related to TG for MFP spectroscopy.

BIBLIOGRAPHY

1. Mark, J. E. *Physical Properties of Polymers Handbook* 1050 pp. ISBN: 978-0-387-69002-5 (Springer Science & Business Media, Mar. 21, 2007).

2. Culebras, M., Gómez, C. M. & Cantarero, A. Review on Polymers for Thermoelectric Applications. *Materials* **7,** 6701–6732 (Sept. 18, 2014).

3. Washo, B. D. & Hansen, D. Heat Conduction in Linear Amorphous High Polymers: Orientation Anisotropy. *Journal of Applied Physics* **40,** 2423–2427. ISSN: 0021-8979 (May 1, 1969).

4. Burgess, S. & Greig, D. The low-temperature thermal conductivity of polyethylene. *Journal of Physics C: Solid State Physics* **8,** 1637. ISSN: 0022-3719 (1975).

5. Kilian, H. G. & Pietralla, M. Anisotropy of thermal diffusivity of uniaxial stretched polyethylenes. *Polymer. Polymer Physics Group Conference* **19,** 664–672. ISSN: 0032-3861 (June 1, 1978).

6. Choy, C. L., Chen, F. C. & Luk, W. H. Thermal conductivity of oriented crystalline polymers. *Journal of Polymer Science: Polymer Physics Edition* **18,** 1187–1207. ISSN: 1542-9385 (June 1, 1980).

7. Choy, C. L., Luk, W. H. & Chen, F. C. Thermal conductivity of highly oriented polyethylene. *Polymer* **19,** 155–162. ISSN: 0032-3861 (Feb. 1, 1978).

8. Poulaert, B., Chielens, J. C., Vandenhende, C., Issi, J. P. & Legras, R. Thermal Conductivity of Highly Oriented Polyethylene Fibers. *Polymer Communications* **31** (Apr. 1990).

9. Mergenthaler, D. B., Pietralla, M., Roy, S. & Kilian, H. G. Thermal conductivity in ultraoriented polyethylene. *Macromolecules* **25,** 3500–3502. ISSN: 0024-9297 (June 1, 1992).

10. Choy, C. L., Yang, G. W. & Wong, Y. W. Thermal diffusivity of polymer films by pulsed photothermal radiometry. *Journal of Polymer Science Part B: Polymer Physics* **35,** 1621–1631. ISSN: 1099-0488 (July 30, 1997).

11. Choy, C. L., Wong, Y. W., Yang, G. W. & Kanamoto, T. Elastic modulus and thermal conductivity of ultradrawn polyethylene. *Journal of Polymer Science Part B: Polymer Physics* **37,** 3359–3367. ISSN: 1099-0488 (Dec. 1, 1999).

12. Shen, S., Henry, A., Tong, J., Zheng, R. & Chen, G. Polyethylene nanofibres with very high thermal conductivities. *Nature Nanotechnology* **5,** 251–255. ISSN: 1748-3387 (Apr. 2010).

13. Ronca, S., Igarashi, T., Forte, G. & Rastogi, S. Metallic-like thermal conductivity in a lightweight insulator: Solid-state processed Ultra High Molecular Weight Polyethylene tapes and films. *Polymer* **123,** 203–210. ISSN: 0032-3861 (Aug. 11, 2017).

14. Xu, Y. *et al.* Nanostructured Polymer Films with Metal-like Thermal Conductivity. *arXiv:1708.06416 [cond-mat].* arXiv: `1708.06416`. `<http://arxiv.org/abs/1708.06416>` (Aug. 21, 2017).

15. Choy, C. L. Thermal conductivity of polymers. *Polymer* **18,** 984–1004. ISSN: 0032-3861 (Oct. 1, 1977).

16. Piraux, L., Kinany-Alaoui, M., Issi, J. .-.-P., Begin, D. & Billaud, D. Thermal conductivity of an oriented polyacetylene film. *Solid State Communications* **70,** 427–429. ISSN: 0038-1098 (Mar. 1989).

17. Wang, X., Ho, V., Segalman, R. A. & Cahill, D. G. Thermal Conductivity of High-Modulus Polymer Fibers. *Macromolecules* **46,** 4937–4943. ISSN: 0024-9297, 1520-5835 (June 25, 2013).

18. Gupta, S., Schieber, J. D. & Venerus, D. C. Anisotropic thermal conduction in polymer melts in uniaxial elongation flows. *Journal of Rheology* **57,** 427–439. ISSN: 0148-6055 (Jan. 16, 2013).

19. Singh, V. *et al.* High thermal conductivity of chain-oriented amorphous polythiophene. *Nature Nanotechnology* **9,** 384–390. ISSN: 1748-3387 (May 2014).

20. Mugishima, T., Kogure, Y., Hiki, Y., Kawasaki, K. & Nakamura, H. Phonon Conduction in Polyethylene. *Journal of the Physical Society of Japan* **57,** 2069–2079. ISSN: 0031-9015 (June 15, 1988).

21. Finlayson, D. M. & Mason, P. J. Structure scattering and the thermal conductivity of a semicrystalline polymer. *Journal of Physics C: Solid State Physics* **18,** 1791. ISSN: 0022-3719 (1985).

22. Rastogi, S., Yao, Y., Ronca, S., Bos, J. & van der Eem, J. Unprecedented High-Modulus High-Strength Tapes and Films of Ultrahigh Molecular Weight Polyethylene via Solvent-Free Route. *Macromolecules* **44,** 5558–5568. ISSN: 0024-9297 (July 26, 2011).

23. Wang, X., Kaviany, M. & Huang, B. Phonon coupling and transport in individual polyethylene chains: a comparison study with the bulk crystal. *Nanoscale* **9,** 18022–18031. ISSN: 2040-3372 (Nov. 23, 2017).

24. Shulumba, N., Hellman, O. & Minnich, A. J. Lattice Thermal Conductivity of Polyethylene Molecular Crystals from First-Principles Including Nuclear Quantum Effects. *Physical Review Letters* **119,** 185901 (Oct. 31, 2017).

25. Zhang, T., Wu, X. & Luo, T. Polymer Nanofibers with Outstanding Thermal Conductivity and Thermal Stability: Fundamental Linkage between Molecular Characteristics and Macroscopic Thermal Properties. *The Journal of Physical Chemistry C.* ISSN: 1932-7447. doi:`10.1021/jp5051639`. <`http://dx.doi.org/10.1021/jp5051639`> (visited on 09/05/2014) (Aug. 19, 2014).

26. Liu, J. & Yang, R. Length-dependent thermal conductivity of single extended polymer chains. *Physical Review B* **86,** 104307 (Sept. 24, 2012).

27. Zhang, T. & Luo, T. Morphology-influenced thermal conductivity of polyethylene single chains and crystalline fibers. *Journal of Applied Physics* **112,** 094304. ISSN: 0021-8979, 1089-7550 (Nov. 1, 2012).

28. Henry, A. & Chen, G. High Thermal Conductivity of Single Polyethylene Chains Using Molecular Dynamics Simulations. *Physical Review Letters* **101.** ISSN: 0031-9007, 1079-7114. doi:`10.1103/PhysRevLett.101.235502`. <`http://link.aps.org/doi/10.1103/PhysRevLett.101.235502`> (visited on 04/26/2014) (Dec. 2008).

29. Freeman, J. J., Morgan, G. J. & Cullen, C. A. Thermal conductivity of a single polymer chain. *Physical Review B* **35,** 7627–7635 (May 15, 1987).

30. Parker, W. J., Jenkins, R. J., Butler, C. P. & Abbott, G. L. Flash Method of Determining Thermal Diffusivity, Heat Capacity, and Thermal Conductivity. *Journal of Applied Physics* **32,** 1679–1684. ISSN: 0021-8979 (Sept. 1, 1961).

31. Nunes dos Santos, W., Mummery, P. & Wallwork, A. Thermal diffusivity of polymers by the laser flash technique. *Polymer Testing* **24,** 628–634. ISSN: 0142-9418 (Aug. 1, 2005).

32. Shrestha, R. *et al.* Crystalline polymer nanofibers with ultra-high strength and thermal conductivity. *Nature Communications* **9,** 1664. ISSN: 2041-1723 (Apr. 25, 2018).

33. Li, D. *et al.* Thermal conductivity of individual silicon nanowires. *Applied Physics Letters* **83,** 2934–2936. ISSN: 0003-6951 (Sept. 30, 2003).

34. Hippalgaonkar, K. *et al.* Fabrication of Microdevices with Integrated Nanowires for Investigating Low-Dimensional Phonon Transport. *Nano Letters* **10,** 4341–4348. ISSN: 1530-6984 (Nov. 10, 2010).

35. Kwon, S., Zheng, J., Wingert, M. C., Cui, S. & Chen, R. Unusually High and Anisotropic Thermal Conductivity in Amorphous Silicon Nanostructures. *ACS Nano* **11,** 2470–2476. ISSN: 1936-0851 (Mar. 28, 2017).

36. Losego, M. D., Moh, L., Arpin, K. A., Cahill, D. G. & Braun, P. V. Interfacial thermal conductance in spun-cast polymer films and polymer brushes. *Applied Physics Letters* **97,** 011908. ISSN: 00036951 (2010).

37. Fayer, M. D. Dynamics of Molecules in Condensed Phases: Picosecond Holographic Grating Experiments. *Annual Review of Physical Chemistry* **33,** 63–87 (1982).

38. Fourkas, J. T. & Fayer, M. D. The transient grating: a holographic window to dynamic processes. *Accounts of Chemical Research* **25,** 227–233. ISSN: 0001-4842 (May 1, 1992).

39. Rose, T. S., Righini, R. & Fayer, M. D. Picosecond transient grating measurements of singlet exciton transport in anthracene single crystals. *Chemical Physics Letters* **106,** 13–19. ISSN: 0009-2614 (Apr. 13, 1984).

40. Rose, T. S., Wilson, W. L., Wäckerle, G. & Fayer, M. D. Gas phase dynamics and spectroscopy probed with picosecond transient grating experiments. *The Journal of Chemical Physics* **86,** 5370–5391. ISSN: 0021-9606 (May 15, 1987).

41. Hyde, P. D., Evert, T. E. & Ediger, M. D. Nanosecond and microsecond study of probe reorientation in orthoterphenyl. *The Journal of Chemical Physics* **93,** 2274–2279. ISSN: 0021-9606 (Aug. 15, 1990).

42. Tokmakoff, A., Banholzer, W. F. & Fayer, M. D. Thermal diffusivity measurements of natural and isotopically enriched diamond by picosecond infrared transient grating experiments. *Applied Physics A* **56,** 87–90. ISSN: 0947-8396, 1432-0630 (1993).

43. Marshall, C. D. *et al.* Thermal boundary resistance and diffusivity measurements on thin YBa2Cu3O7-x films with MgO and SrTiO3 substrates using the transient grating method. *Journal of Applied Physics* **73,** 850–857. ISSN: 0021-8979, 1089-7550 (Jan. 15, 1993).

44. Cho, M., Scherer, N. F., Fleming, G. R. & Mukamel, S. Photon echoes and related four-wave-mixing spectroscopies using phase-locked pulses. *The Journal of Chemical Physics* **96,** 5618–5629. ISSN: 0021-9606 (Apr. 15, 1992).

45. Maznev, A. A., Nelson, K. A. & Rogers, J. A. Optical heterodyne detection of laser-induced gratings. *Optics Letters* **23,** 1319–1321. ISSN: 1539-4794 (Aug. 15, 1998).

46. Vega-Flick, A. *et al.* Laser-induced transient grating setup with continuously tunable period. *Review of Scientific Instruments* **86,** 123101. ISSN: 0034-6748, 1089-7623 (Dec. 1, 2015).

47. Rogers, J. A. & Nelson, K. A. Study of Lamb acoustic waveguide modes in unsupported polyimide thin films using real-time impulsive stimulated thermal scattering. *Journal of Applied Physics* **75,** 1534–1556. ISSN: 0021-8979, 1089-7550 (Feb. 1, 1994).

48. Rogers, J. A., Yang, Y. & Nelson, K. A. Elastic modulus and in-plane thermal diffusivity measurements in thin polyimide films using symmetry-selective real-time impulsive stimulated thermal scattering. *Applied Physics A* **58,** 523–534. ISSN: 0947-8396, 1432-0630 (May 1, 1994).

49. Okuda, M. & Nagashima, A. Optical measurement of the anisotropic behavior of the thermal diffusivity of oriented poly(methyl methacrylate). *High Temperatures - High Pressures* **21,** 205–210 (1989).

50. Maznev, A. A., Johnson, J. A. & Nelson, K. A. Onset of nondiffusive phonon transport in transient thermal grating decay. *Physical Review B* **84,** 195206 (Nov. 28, 2011).

51. Minnich, A. J. *et al.* Thermal Conductivity Spectroscopy Technique to Measure Phonon Mean Free Paths. *Physical Review Letters* **107,** 095901 (Aug. 25, 2011).

52. Minnich, A. J. Determining Phonon Mean Free Paths from Observations of Quasiballistic Thermal Transport. *Physical Review Letters* **109,** 205901 (Nov. 13, 2012).

53. Minnich, A. J. Multidimensional quasiballistic thermal transport in transient grating spectroscopy. *Physical Review B* **92,** 085203 (Aug. 13, 2015).

54. Johnson, J. A. *et al.* Direct Measurement of Room-Temperature Nondiffusive Thermal Transport Over Micron Distances in a Silicon Membrane. *Physical Review Letters* **110,** 025901 (Jan. 8, 2013).

55. Siemens, M. E. *et al.* Quasi-ballistic thermal transport from nanoscale interfaces observed using ultrafast coherent soft X-ray beams. *Nature Materials* **9,** 26–30. ISSN: 1476-4660 (Jan. 2010).

56. Zeng, L. *et al.* Measuring Phonon Mean Free Path Distributions by Probing Quasiballistic Phonon Transport in Grating Nanostructures. *Scientific Reports* **5,** 17131. ISSN: 2045-2322 (Nov. 27, 2015).

57. Hu, Y., Zeng, L., Minnich, A. J., Dresselhaus, M. S. & Chen, G. Spectral mapping of thermal conductivity through nanoscale ballistic transport. *Nature Nanotechnology* **10,** 701–706. ISSN: 1748-3395 (Aug. 2015).

58. Chen, X., Hua, C., Zhang, H., Ravichandran, N. K. & Minnich, A. J. Quasiballistic Thermal Transport from Nanoscale Heaters and the Role of the Spatial Frequency. *Physical Review Applied* **10,** 054068 (Nov. 29, 2018).

59. Ramu, A. T., Halaszynski, N. I., Peters, J. D., Meinhart, C. D. & Bowers, J. E. An electrical probe of the phonon mean-free path spectrum. *Scientific Reports* **6,** 33571. ISSN: 2045-2322 (Sept. 28, 2016).

60. Robbins, A. B. & Minnich, A. J. Crystalline polymers with exceptionally low thermal conductivity studied using molecular dynamics. *Applied Physics Letters* **107,** 201908 (Nov. 16, 2015).

61. Luo, T., Esfarjani, K., Shiomi, J., Henry, A. & Chen, G. Molecular dynamics simulation of thermal energy transport in polydimethylsiloxane. *Journal of Applied Physics* **109,** 074321. ISSN: 00218979 (2011).

62. Edmondson, S., Osborne, V. L. & Huck, W. T. S. Polymer brushes via surface-initiated polymerizations. *Chemical Society Reviews* **33,** 14. ISSN: 0306-0012, 1460-4744 (2004).

63. Plimpton, S. Fast Parallel Algorithms for Short-Range Molecular Dynamics. *Journal of Computational Physics* **117,** 1–19. ISSN: 0021-9991 (Mar. 1, 1995).

64. Sakurai, K., Kashiwagi, T. & Takahashi, T. Crystal structure of polynor-bornene. *Journal of Applied Polymer Science* **47,** 937–940. ISSN: 1097-4628 (Feb. 5, 1993).

65. Sun, H. Ab initio calculations and force field development for computer simulation of polysilanes. *Macromolecules* **28,** 701–712. ISSN: 0024-9297 (Jan. 1, 1995).

66. Thomas, J. A., Turney, J. E., Iutzi, R. M., Amon, C. H. & McGaughey, A. J. H. Predicting phonon dispersion relations and lifetimes from the spectral energy density. *Physical Review B* **81,** 081411 (Feb. 26, 2010).

67. Feng, T., Qiu, B. & Ruan, X. Anharmonicity and necessity of phonon eigen-vectors in the phonon normal mode analysis. *Journal of Applied Physics* **117,** 195102. ISSN: 0021-8979, 1089-7550 (May 21, 2015).

68. Thomas, J. A., Turney, J. E., Iutzi, R. M., Amon, C. H. & McGaughey, A. J. H. Erratum: Predicting phonon dispersion relations and lifetimes from the spectral energy density. *Physical Review B* **91,** 239905 (June 30, 2015).

69. Braden, D. A., Parker, S. F., Tomkinson, J. & Hudson, B. S. Inelastic neutron scattering spectra of the longitudinal acoustic modes of the normal alkanes from pentane to pentacosane. *The Journal of Chemical Physics* **111,** 429–437. ISSN: 0021-9606, 1089-7690 (July 1, 1999).

70. Tomkinson, J., Parker, S. F., Braden, D. A. & Hudson, B. S. Inelastic neutron scattering spectra of the transverse acoustic modes of the normal alkanes. *Physical Chemistry Chemical Physics* **4,** 716–721. ISSN: 1463-9084 (Feb. 20, 2002).

71. Barrera, G. D., Parker, S. F., Ramirez-Cuesta, A. J. & Mitchell, P. C. H. The Vibrational Spectrum and Ultimate Modulus of Polyethylene. *Macro-molecules* **39,** 2683–2690. ISSN: 0024-9297 (Apr. 1, 2006).

72. Ioffe, A. & Regel, A. Non-crystalline, amorphous, and liquid electronic semi-conductors. *Progress in Semiconductors* **4,** 237–291 (1960).

73. Allen, P. B., Feldman, J. L., Fabian, J. & Wooten, F. Diffusons, locons and propagons: Character of atomie yibrations in amorphous Si. *Philosophical Magazine Part B* **79,** 1715–1731. ISSN: 1364-2812 (Nov. 1, 1999).

74. Chen, X. *et al.* Twisting phonons in complex crystals with quasi-one-dimensional substructures. *Nature Communications* **6.** doi:`10.1038/ncomms7723`. `<http://www.nature.com/ncomms/2015/150415/ncomms7723/full/ncomms7723.html>` (visited on 04/16/2015) (Apr. 15, 2015).

75. Cahill, D. G., Fischer, H. E., Watson, S. K., Pohl, R. O. & Slack, G. A. Thermal properties of boron and borides. *Physical Review B* **40,** 3254–3260 (Aug. 15, 1989).

76. Cahill, D. G. Thermal conductivity measurement from 30 to 750 K: the 3-omega method. *Review of Scientific Instruments* **61,** 802–808. ISSN: 0034-6748, 1089-7623 (Feb. 1, 1990).

77. Cahill, D. G. *et al.* Nanoscale thermal transport. II. 2003–2012. *Applied Physics Reviews* **1,** 011305. ISSN: 1931-9401 (Mar. 1, 2014).

78. Koh, Y. K. & Cahill, D. G. Frequency dependence of the thermal conductivity of semiconductor alloys. *Phys. Rev. B* **76,** 075207 (Aug. 2007).

79. Highland, M. *et al.* Ballistic-phonon heat conduction at the nanoscale as revealed by time-resolved x-ray diffraction and time-domain thermoreflectance. *Phys. Rev. B* **76,** 075337 (Aug. 2007).

80. Wilson, R. B. & Cahill, D. G. Anisotropic failure of Fourier theory in time-domain thermoreflectance experiments. *Nature Communications* **5.** doi:`10.1038/ncomms6075`. `<http://www.nature.com.clsproxy.library.caltech.edu/ncomms/2014/141001/ncomms6075/full/ncomms6075.html>` (visited on 01/02/2015) (Oct. 1, 2014).

81. Zhang, H., Chen, X., Jho, Y.-D. & Minnich, A. J. Temperature-Dependent Mean Free Path Spectra of Thermal Phonons Along the c-Axis of Graphite. *Nano Letters* **16,** 1643–1649. ISSN: 1530-6984 (Mar. 9, 2016).

82. Jiang, P., Qian, X. & Yang, R. Time-domain thermoreflectance (TDTR) measurements of anisotropic thermal conductivity using a variable spot size approach. *Review of Scientific Instruments* **88,** 074901. ISSN: 0034-6748 (July 1, 2017).

83. Rodin, D. & Yee, S. K. Simultaneous measurement of in-plane and through-plane thermal conductivity using beam-offset frequency domain thermoreflectance. *Review of Scientific Instruments* **88,** 014902. ISSN: 0034-6748 (Jan. 1, 2017).

84. Chang, Y. J., Cong, P. & Simon, J. D. Optical heterodyne detection of impulsive stimulated Raman scattering in liquids. *The Journal of Physical Chemistry* **99,** 7857–7859. ISSN: 0022-3654 (May 1, 1995).

85. Maznev, A. A., Crimmins, T. F. & Nelson, K. A. How to make femtosecond pulses overlap. *Optics Letters* **23,** 1378–1380. ISSN: 1539-4794 (Sept. 1, 1998).

86. Rao, D. N., Burzynski, R., Mi, X. & Prasad, P. N. Picosecond transient grating studies of polymeric thin films. *Applied Physics Letters* **48,** 387–389. ISSN: 0003-6951, 1077-3118 (Feb. 10, 1986).

87. Kurabayashi, K., Asheghi, M., Touzelbaev, M. & Goodson, K. E. Measurement of the thermal conductivity anisotropy in polyimide films. *Journal of Microelectromechanical Systems* **8,** 180–191. ISSN: 1057-7157 (June 1999).

88. Zhang, Z., Zhao, P., Lin, P. & Sun, F. Thermo-optic coefficients of polymers for optical waveguide applications. *Polymer* **47,** 4893–4896. ISSN: 0032-3861 (June 28, 2006).

89. Ravichandran, N. K. *Theoretical and Experimental Investigation of Phonon Boundary Scattering in Thin Silicon Membranes* PhD thesis (California Institute of Technology, 2017). <http://resolver.caltech.edu/CaltechTHESIS:01172017-145551495> (visited on 09/25/2018).

90. Robbins, A. B., Drakopoulos, S. X., Ronca, S. & Minnich, A. J. Thermal Phonons with Micron-Scale Mean Free Paths in Semi-Crystalline Polyethylene. *(In Preparation).*

91. Lu, L., Alamo, R. G. & Mandelkern, L. Lamellar Thickness Distribution in Linear Polyethylene and Ethylene Copolymers. *Macromolecules* **27,** 6571–6576. ISSN: 0024-9297 (Oct. 1, 1994).

92. Marega, C., Marigo, A., Cingano, G., Zannetti, R. & Paganetto, G. Small-angle X-ray scattering from high-density polyethylene: lamellar thickness distributions. *Polymer* **37,** 5549–5557. ISSN: 0032-3861 (Jan. 1, 1996).

93. Zhou, H. & Wilkes, G. L. Comparison of lamellar thickness and its distribution determined from d.s.c., SAXS, TEM and AFM for high-density polyethylene films having a stacked lamellar morphology. *Polymer* **38,** 5735–5747. ISSN: 0032-3861 (Nov. 1, 1997).

94. Hansen, D. & Bernier, G. A. Thermal conductivity of polyethylene: The effects of crystal size, density and orientation on the thermal conductivity. *Polymer Engineering & Science* **12,** 204–208. ISSN: 1548-2634 (May 1, 1972).

95. Chang, S. S. & Bastul, A. B. Heat capacities of polyethylene from 2 to 360 K. I. Standard samples of linear and branched polyethylene whole polymer. *Journal of Research of the National Institute of Standards and Technology* **77A,** 395–405 (Mar. 14, 1973).

96. Minnich, A. J. Phonon heat conduction in layered anisotropic crystals. *Physical Review B* **91,** 085206 (Feb. 17, 2015).

97. Hastings, W. K. Monte Carlo Sampling Methods Using Markov Chains and Their Applications. *Biometrika* **57,** 97–109. ISSN: 0006-3444 (1970).

98. Ravichandran, N. K., Zhang, H. & Minnich, A. J. Spectrally Resolved Specular Reflections of Thermal Phonons from Atomically Rough Surfaces. *Physical Review X* **8,** 041004 (Oct. 5, 2018).

99. Davis, G. T. & Eby, R. K. Glass transition of polyethylene: Volume relaxation. *Journal of Applied Physics* **44,** 4274–4281. ISSN: 0021-8979 (Oct. 1, 1973).

100. Beatty, C. L. & Karasz, F. E. The Glass Transition of Linear Polyethylene. *Journal of Macromolecular Science, Part C* **17,** 37–60. ISSN: 1532-1797 (Jan. 1, 1979).